Advanced Methods of Joining for Indian Reduced Activation Ferritic/Martensitic Steel

A thesis

Submitted by

Manugula Vijayalakshmi

in partial fulfilment of the requirements for the award of the degree of

Doctor of Philosophy

in

Materials Engineering

School of Engineering Sciences and Technology

University of Hyderabad, India

June, 2017

Advanced Methods of Joining for Indian Reduced Activation Ferritic/Martensitic Steel

A thesis

Submitted by

Manugula Vijayalakshmi

in partial fulfilment of the requirements for the award of the degree of

Doctor of Philosophy

in

Materials Engineering

Under the supervision of

Dr. Koteswararao V Rajulapati

and

Dr. G Madhusudhan Reddy

School of Engineering Sciences and Technology

University of Hyderabad, India

June, 2017

DECLARATION

I, **M. Vijayalakshmi** hereby declare that this thesis work entitled ***"Advanced Methods of Joining for Indian Reduced Activation Ferritic/Martensitic Steel"*** submitted in partial fulfilment of the requirements for the award of **Doctor of Philosophy** (in **Materials Engineering**) in the School of Engineering Sciences and Technology (SEST), University of Hyderabad is a bonafide record of the work which was carried out by me under the supervision of **Dr. Koteswararao V. Rajulapati** and **Dr. G. Madhusudhan Reddy.** I also declare that the content of this thesis has not been submitted earlier, as a whole or in part, to this University or any other University/ Institution for the award of any degree or equivalent.

(M.Vijayalakshmi)
Reg. No.: 11ETPM02
School of Engineering Sciences and Technology
University of Hyderabad

CERTIFICATE

This is to certify that the thesis work entitled ***"Advanced Methods of Joining for Indian Reduced Activation Ferritic/Martensitic Steel"***, submitted by **M. Vijayalakshmi** bearing Reg. No. **11ETPM02** in partial fulfilment of the requirements for the award of the degree of **Doctor of Philosophy** in **Materials Engineering** is a bonafide record of research work that has been carried out by her under our guidance and supervision. The content of this thesis has not been submitted earlier, as a whole or in part, to this or any other University/Institution for the award of any degree or equivalent.

Thesis Supervisor

Dr. Koteswararao V. Rajulapati
Associate Professor
School of Engineering Sciences and Technology
University of Hyderabad

Thesis Co-Supervisor

Dr. G. Madhusudhan Reddy
Outstanding Scientist, MJG
DMRL
Hyderabad

Approved by

Prof. M. Ghanashyam Krishna
Dean
School of Engineering Sciences and Technology
University of Hyderabad

CERTIFICATE

This is to certify that the thesis entitled "***Advanced methods of joining for Indian reduced activation ferritic/martensitic steel***" submitted by **M. Vijayalakshmi** bearing registration number **11ETPM02** in partial fulfilment of the requirements for award of **Doctor of Philosophy** (in **Materials Engineering**) in the School of Engineering Sciences and Technology (SEST) is a bonafide work carried out by her under my supervision and guidance.

This thesis is free from plagiarism and has not been submitted previously in part or in full to this or any other University or Institution for award of any degree or diploma.

Parts of this thesis have been published in the following publications:

1. ***Materials and Design, 92(2016)200-212***
2. ***Metallurgical and Materials Transactions A, 48 (2017) 3702-3720.***
3. ***Material Science and Engineering A, 698 (2017)36-45.***

Further, the student has passed the following courses towards fulfilment of coursework requirement for Ph.D.

Course Code	Course Title	Credits	Pass /Fail
MT704	Thermodynamics and Phase Equilibria	4	Pass
MT710	Concepts of Materials Science	4	Pass
MT712	Metal Forming: Science and Technology	4	Pass
MT715	Characterization of Materials	4	Pass
MT724	Seminar	2	Pass
MT730	Design & Selection of Engineering Materials	4	Pass
MT731	Advanced Engineering Mathematics	2	Pass
MT735	Materials Processing and Characterization Laboratory	4	Pass
PD601	Research Methodology	4	Pass

Supervisor **Dean of School**

ACKNOWLEDGEMENTS

Firstly, I would like to express my sincere gratitude to my supervisors Dr.Koteswararao V Rajulapati and Dr.G.Madhusudhan Reddy for their guidance, support and motivation throughout my Ph.D study and related research work. I consider it as a great opportunity to do my research work under their guidance and to learn from their research expertise.

This thesis would not have been materialized without the support of Prof. K.Bhanu Sankara Rao Ministry of Steel, Chair Professor MGIT. His guidance helped me in all the time of research and writing of this thesis. Without his precious support it would not be possible to conduct this research work. My heartfelt thanks are due to Dr. Mythili Scientist 'G' IGCAR Kalpakkam for dedicating her time and efforts in TEM investigations.

Special thanks to Sri P. Mastaniah, Scientist DRDL, for conducting EBW experiments. I express my deep sense of gratitude to Mr. Nagaraj Kaumudi, Scientist, DMRL in conducting thermography. I am thankful to Prof. Indradev Samajdar, Mr. A. Durgaprasad of National Facility of Texture and OIM at IIT, Bombay for EBSD experiments. I thank Mr.M. Durgaprasad, School of Chemistry, UoH for assisting in FE-SEM experiments.

I would like to thank the doctoral research committee members Dr.-Ing.V.V.S.S. Srikanth and Dr. Swathi Ghosh Acharya for their insightful comments during the review meetings. Special thanks to Dr.-Ing.V.V.S.S.Srikanth for his assistance in Corel draw software.

I am grateful to Prof. Ghanashyam Krishna Dean, SEST and former Deans, Prof. M.Sundaraman and Prof. Rajender Singh and all the faculty members for their support during the course of my work. My sincere thanks to Dr. Samir Kamath, Director, DMRL and former Directors Dr.G. Malakondaiah and Dr. Amol A Gokhale, for permitting me to carry out this research work at DMRL, Hyderabad.

I wish to acknowledge all the scientists, technical officers and staff of metal joining group for their cooperation and help during my research work at DMRL. Special thanks are due to Mr.G.R. Vijay kumar and Mr. Ajay (Friction stir welding), Mr. T. Ramachandram (Hardness measurements) Mr. K. Sunil of MEG for preparation of tensile and impact samples, Ms. Vijayalakshmi, Mr. Sai Madhav and Mr. Venugopal of SFAG for Optical microscopy. I thank Dr.V.V. Satyanarayana, Group Head, MBG and Mr. Vikram for tensile and impact testing. I thank Dr. Pardha Goshal, Group Head, EMG and Mr. Deepak for TEM sample preparation.

I will forever be grateful to Dr.J. Viplava kumar former Dean R&D, MGIT who has motivated me to pursue Ph.D, and all the support rendered for my professional growth. I would like to express my gratefulness to the management of MGIT, Hyderabad for permitting me to register for Ph.D and carry out research work. I place my special thanks to Dr. G. Chandramohan Reddy, Principal and Sri P.K Subramanian, former head of department, Dept. MMT, for their wholehearted encouragement and cooperation during my research work. I express my sincere thanks to HoD, and all the faculty members and non-teaching staff of the Department of Metallurgical and Materials Engineering, MGIT for the moral support and readiness in sharing the work, which helped me to concentrate on my research work. I am grateful to my student friends, U. Savitha, K. Sivaji, Y Pardhu, Rahul, M.Kamal, Johny and Koushikumar for their support during my research work.

Last but not the least; I would like to thank my parents, brother, sisters and my mother-in-law for supporting me spiritually throughout writing this thesis. I owe a lot to my mother M. Kusuma, who encouraged and helped me at every stage of my personal and academic life, and longed to see this achievement come true. I am very much indebted to my family, my husband Mr. N. Nagaraju, sons Venkata Aditya and Maruthi Jaideep, who supported me in every possible way to see the completion of this work.

Finally, I would like to dedicate this thesis to my husband and my children.

M.Vijayalakshmi

List of publications based on the research work

1. ***Vijaya L.Manugula****, Koteswararao V.Rajulapati, G.Madhusudhan Reddy, R Mythili and K.Bhanu Sankara Rao,* "A Critical Assessment of the Microstructure and Mechanical Properties of Friction Stir Welded Reduced Activation Ferritic-Martensitic Steel", ***Materials and Design****, **92(2016)200-212**.*

2. ***Vijaya L.Manugula****, Koteswararao V.Rajulapati, G.Madhusudhan Reddy, R. Mythili and K. Bhanu Sankara Rao,* "Influence of Tool Rotational Speed and Post-weld Heat Treatments on Friction Stir Welded Reduced Activation Ferritic-Martensitic Steel", ***Metallurgical and Materials Transactions A, 48 (2017) 3702-3720.***

3. ***Vijaya L.Manugula****, Koteswararao V.Rajulapati, G.Madhusudhan Reddy, and K. Bhanu Sankara Rao, "R*ole of Evolving Microstructure on the Mechanical Properties of Electron Beam Welded Ferritic-Martensitic Steel in the As-Welded and Post weld Heat-Treated States", ***Material Science and Engineering A ,698 (2017)36-45****.*

4. ***Vijaya L.Manugula****, Koteswararao V.Rajulapati, G.Madhusudhan Reddy, R. Mythili and K. Bhanu Sankara Rao, "*Adaption of a Green Technology (Friction Stir Welding) to Join Fusion Energy Materials*", **Energy Materials**, Proceedings of CAETS 2015 Convocation on Pathways to Sustainability,* ***Chapter, Springer ISBN 978-981-10-3101-4, 173-177.***

Conferences/Workshops attended

1. Oral presentation, "Insights into friction stir welding of reduced activation ferritic-martensitic steel", NMD-ATM 2015,Coimbatore, 13th Nov-16th Nov, 2015

2. Oral presentation, "Friction stir welding of Indian reduced activation ferritic-martensitic steel" National Welding Seminar 2015, CIDCO Convention Centre Vashi, Mumbai, 9th Dec-11th Dec, 2015

3. Oral presentation, "Influence of post-weld heat treatments on microstructure and mechanical properties of reduced activation ferritic martensitic steel electron beam welds", International Institute of Welding 6th Welding Research and Collaboration Colloquium", MAK Club Banyan Tree Retreat, Hyderabad,7th -9th April, 2016

4. Poster presentation, **"**Adaption of a Green Technology (Friction Stir Welding) to Join Fusion Energy Materials", International Council of Academies of Engineering and Technological Sciences, Inc. (CAETS) Convocation -2015, Hotel Ashok, New Delhi, October 13th-15th, 2015**.**

5. Oral presentation "Role of section thickness in friction stir welding of reduced activation ferritic/martensitic steel", National Welding Seminar, Science city, Kolkata, Dec 9th-11th, 2016

6. Oral presentation, "Integrated approach in metallurgical understanding of friction stir welded reduced activation ferritic/martensitic steel", one day workshop, Challenges in Joining of Advanced Materials", Gurukul, NFC, Hyderabad, 26th, May 2017

CONTENTS

List of Figures

List of Tables

List of Symbols and Abbreviations

AS	Advancing Side
ASTM	American Society for Testing and Materials
BM	Base Metal
CCT	Continuous Cooling Transformation
DBTT	Ductile-to-Brittle Transition Temperature
DSC	Differential Scanning Calorimetry
EBSD	Electron Backscatter Diffraction
EBW	Electron Beam Welding
EDS	Energy Dispersive Spectra
FE-SEM	Field-Emission -Scanning Electron Microscopy
FSW	Friction Stir Welding
FZ	Fusion Zone
HAGBs	High Angle Grain Boundaries
HAZ	Heat Affected Zone
HV	Vickers Hardness
ITER	International Thermonuclear Experimental Reactor
ODS	Oxide Dispersion Strengthened
LAGBs	Low Angle Grain Boundaries
PAGBs	Prior Austenite Grain Boundaries
PcBN	Polycrystalline Cubic Boron Nitride
PWDT	Post Weld Direct Tempering
PWHT	Post Weld Heat Treatment
PWNT	Post Weld Normalized and Tempered
RAFM	Reduced Activation Ferritic / Martensitic Steel
RS	Retreating Side
SAED	Selected Area Electron Diffraction
SMA	Shielded Metal Arc
SZ	Stir Zone
TBM	Test Blanket Module
TEM	Transmission Electron Microscopy
TIG	Tungsten Inert Gas
TMAZ	Thermo-Mechanically Affected Zone
TTT	Time Temperature Transformation
A_{c1}	Austenite Start Temperature
A_{c3}	Austenite Finish Temperature
KAB	Cliff-Lorimer Constant
M_f	Martensite Finish Temperature
Ms	Martensite Start Temperature
UTS	Ultimate Tensile Strength
WM	Weld Metal
YS	Yield Strength
α	Low Temperature Ferrite
α'	Martensite
γ	Austenite
δ	High Temperature Ferrite

Abstract

Reduced activation ferritic–martensitic (RAFMs) steels are potential candidate structural materials for first wall and test blanket modules (TBMs) of International Thermonuclear Experimental Reactor (ITER) which is under construction in France. The development of these steels has been pursued by European Union, United States of America, Japan, China and India. The main objectives behind the development of these steels is to arrive at a chemical composition that could give an optimum combination of physical, mechanical and thermal properties and also capable of achieving rapid decay of the radioactivity induced by various elements under neutron irradiation in the prevailing fusion reactor environment.

The RAFM steels were designed by altering the chemical composition of the conventional Mod.9Cr -1Mo ferritic-martensitic steel, with substitution of W and Ta for Mo and Nb respectively, in order to promote rapid decay of radioactivity after irradiation. India's participation in ITER programme necessitated the development of India-specific RAFM steel for TBM. Several heats of RAFM steels were processed by varying W (1- 2wt. %) and Ta (0.06-0.18wt. %) contents. These steels have been produced by vacuum induction melting followed by vacuum arc refining which enabled to obtain clean, homogeneous and 'segregation-free' ingots. The controlled chemical composition was achieved by proper selection of raw materials and completely avoiding the usage of scrap during melting. These precautions were found indispensible with respect to obtaining control over radiologically undesirable elements as well as trace and tramp elements. Based on extensive studies on phase transformations, heat treatments, initial microstructure, physical and mechanical properties, the composition of India- specific RAFM steel has been identified. The

INRAFM steel chosen for fabrication of TBM of ITER contains 1.4 wt. % tungsten and 0.06 wt. % tantalum and recommended for its use in the normalized plus tempered condition.

The manufacturing processes that are being considered for fabrication of TBM channels include welding, hot isostatic pressing and micromachining. In general, high heat input fusion welding processes such as shielded metal arc (SMA) and tungsten inert gas (TIG) welding processes develop a wider heat affected zone (HAZ) in ferritic-martensitic steels and generate an inhomogeneous microstructure in the HAZ, resulting in a marked variation in mechanical properties across the weld joint. Premature failures have been reported quite often in the ferritic-martensitic steel weld joints, due to the pronounced localization of creep deformation and cracking at the parent metal/HAZ interface; these are classified as Type IV cracking failures. In the light of these observations, electron beam welding (EBW) and friction stir welding (FSW) processes have been explored since both these joining processes will not produce extensive HAZ due to the low heat input employed. Furthermore, fusion welding processes under certain conditions may introduce δ- ferrite in the fusion zone (FZ) which is considered to be detrimental for mechanical properties at elevated temperatures. This issue also calls for establishing the welding methods and post-weld-heat-treatments that could eliminate δ-ferrite in the fusion zone.

In this study detailed investigations are conducted on FSW of India specific RAFM steel with the aim of demonstrating the feasibility of FSW of 6mm and 12 mm thick plates and to understand the effects of rotational speed and section thickness on the development of the microstructure and hardness in various zones. An attempt has been made to demonstrate the usage of in-line thermography to monitor the temperature changes resulting from the variation in rotational speed of

tool, and to establish appropriate post weld heat treatments (PWHTs) that would develop homogeneous microstructure and impart reasonable hardness and impact toughness in the weld joints.

Bead-on-Plate FSW was conducted on 6 mm thick plate of RAFM steel employing polycrystalline cubic boron nitride tool with varying rotational speeds at a constant traverse speed of 30 mm/min. The weld joint of FSW is composed of stir zone, thermo-mechanically affected zone, heat affected zone and base metal. The selection of rotational speeds of 200 rpm, 300 and 500rpm and 700rpm were chosen such that the peak temperature attained in the stir zone (SZ) during FSW was below A_{c1}, between A_{c1} and $A_{c3,}$ and above A_{c3} respectively. In the base metal (BM), the prior austenite grain and martensite lath boundaries were decorated with chromium and tungsten rich $M_{23}C_6$ precipitates while intra-lath regions revealed Ta and V rich MX type carbides. Rotational speeds greater than 300 rpm led to martensite formation and simultaneous recovery, recrystallization and grain growth in SZs with wide distribution in grain size. The SZ of 200 rpm and BM possessed similar grain size distribution. The grain boundary $M_{23}C_6$ dissolved and very fine needles of Fe_3C precipitated in all SZs. The hardness in SZ obtained at various rotational speeds was unacceptably higher compared to the BM. The 200 rpm weld exhibited higher impact toughness in the absence of martensite in SZ.

Since the absence of grain boundary strengthening precipitates in SZ would promote premature creep failures, investigations have been conducted to restore them by appropriate PWHTs. The low and high rotational speed FSW welds at 200 and 700 rpm were subjected to two types of PWHTs, namely post weld direct tempering (PWDT) and post weld normalizing and tempering (PWNT). PWHTs caused the dissolution of Fe_3C and re-appearance of $M_{23}C_6$ on grain boundaries in SZ. The

PWNT treatment promoted nearly uniform hardness across 200 rpm weld joint and significantly improved the impact toughness at both the rotational speeds.

Higher section-thickness strongly influenced the width of various zones and microstructures developed due to thermal gradients and associated slow cooling rates across the weld joint resulting from high heat input. The SZ hardness of 12 mm thick plate was less than that obtained in SZ of 6 mm plate. The microstructures developed in TMAZ and HAZ of 12 mm thick plate were different from those obtained in 6mm plate. PWHTs were found beneficial in decreasing the hardness of SZ and enabling the desirable precipitation of grain boundary carbides. The excessive softening of HAZ was prominent after PWDT. However, the softening of HAZ could be eliminated after PWNT treatment.

The present work is also aimed at establishing suitable PWHTs for restoring the mechanical properties of EBW joints to the level of BM, and developing a comprehensive understanding of evolving microstructure during the EBW and PWHTs across various zones of the weld joint. In the as-welded state, the FZ contained martensite in coarse grains and small amount of δ-ferrite with no evidence for precipitation of $M_{23}C_6$ and MX either in intra- or inter-granular regions. The as-welded joints exhibited high hardness in the FZ and HAZ and the impact toughness was inferior compared to that of the BM. PWNT treatment minimized the variation in hardness across the transverse section of weld joint and the impact toughness surpassed than that achieved in BM. The tensile properties of BM, welded joints in as-welded and in PWHT conditions were determined at room temperature and correlated with the prevailing microstructures. Delta-ferrite in FZ of EBW joint was eliminated after PWNT treatment. As a result the impact toughness of weld joint is drastically improved.

Chapter 1- Introduction

Reduced activation ferritic-martensitic (RAFM) steels are currently being considered as main structural materials for Test Blanket Module (TBM) and first wall of the International Thermonuclear Experimental Reactor (ITER) due to the low levels of induced radioactivity in fusion reactor environment [1, 2]. These steels were designed by altering the chemical composition of the conventional Mod.9Cr-1Mo ferritic-martensitic steel, with substitution of W and Ta for Mo and Nb respectively, in order to promote rapid decay of radioactivity after irradiation [3-5]. India is one of the countries associated with the development and testing of TBMs in ITER. In view of this, India has taken up an ambitious programme of developing its own RAFM steel. Several experimental heats have been produced by varying W and Ta and extensive characterization of microstructure and mechanical properties was undertaken. These studies have indicated that RAFM steel having 1.4 wt. % tungsten with 0.06 wt. % tantalum was found to possess better combination of tensile strength, creep strength, and low cycle fatigue resistance at elevated temperatures and very low ductile-to-brittle-transition temperature (DBTT) [6-8]. The steel with its above composition for W and Ta has been designated as Indian RAFM steel.

In general welding of ferritic-martensitic steels by conventional fusion welding processes have distinctive features in heat affected zone (HAZ) as a result of phase transformations that occur during weld thermal cycle [4].The high heat input shielded metal arc (SMA) and tungsten inert gas (TIG) welding processes, during the weld thermal cycle, promote a wider HAZ and generate an inhomogeneous microstructure in the HAZ of ferritic-martensitic steels, resulting in a marked variation in mechanical properties across the weld joint.

Therefore, the full performance of 9-12% Cr ferritic-martensitic steels has often not been realized in service due to the premature failures at the parent metal/HAZ interface of weld joints. These failures are commonly referred to as Type-IV cracking and have been reported to occur due to the pronounced localization of creep deformation coupled with preferential creep cavitation in the soft intercritical region of HAZ [9, 10]. The weld joints of RAFM steels fabricated by SMA and TIG welding processes would also be expected to undergo Type-IV cracking failures when the weld joints are made by employing SMA/TIG welding methods.

On the other hand, advanced methods of joining such as electron beam welding (EBW) and friction stir welding (FSW) processes appear to be beneficial in that these do not produce extensive HAZ due to the low heat input employed, and therefore expected to reduce the HAZ and its associated deleterious effects [11]. The important issue in fusion welding of RAFM steel that needs to be addressed is the occurrence of δ-ferrite that nucleates during the solidification of liquid metal produced during fusion welding processes [11]. The presence of δ-ferrite in tempered martensitic matrix raises the DBTT, and also deteriorates impact toughness and creep rupture strength [13]. In this aspect, the solid state FSW is beneficial since it does not produce liquid metal and subsequent solidification does not prevail. Therefore no δ-ferrite could be expected in the weld zone [14]. However, the wide usage of FSW in the fabrication of steels was hindered by non-availability of a suitable tool material. With the emergence of Poly Crystalline Cubic Boron Nitride (PcBN) tools, FSW of steels is now receiving considerable attention. There is limited data available on FSW of RAFM steel and the influence of various FSW parameters on microstructure and mechanical properties is far from fully understood. In order to address this, the current study has been undertaken.

1.1. Objectives and scope of the thesis

This thesis is aimed at establishing suitable welding parameters for the production of very clean RAFM steel weld joints by employing FSW and EBW processes and understanding the role of evolving microstructure on mechanical properties. Special attention has been paid to develop suitable post weld heat treatments (PWHTs) and understanding their role in promoting the suitable microstructure for deriving the optimum mechanical properties in INRAFM (India-specific) steel weld joints. The thesis addresses the following aspects:

- Evaluation of the feasibility of FSW and EBW processes for joining India specific RAFM steel
- Demonstration of the usage of in-line thermography to monitor the temperature changes resulting from the variation in rotational speed of tool for the first time in FSW process
- Detailed investigations on the effects of rotational speed on the evolving microstructure in stir zones of FSW weld joints with special reference to phase transition temperatures
- Studies on the effects of microstructure on hardness and impact toughness in FSW joints
- Assessment on the effects of post weld heat treatments on microstructure and mechanical properties of FSW joints
- Exploring the section thickness effects on microstructure and mechanical properties of FSW joints
- Evaluation of microstructure and its influence on mechanical properties of EBW joints
- Deduction of post-weld heat treatment effects in EBW joints

1.2. Overview of the thesis

Chapter 2, "**Literature review**," briefly presents a review of the existing literature on the RAFM steel, with emphasis on origin of alloy development, transformation temperatures, mechanical properties and welding aspects of the steel. This chapter also highlights the specific issues related to fusion welding aspects of ferritic/martensitic steels that need to be addressed, the current status of research in this field and the necessity for further investigations. This chapter also covers an overview of welding processes (friction stir welding and electron beam welding) employed in this study.

Chapter 3 deals with the **"Experimental methodology"** adopted in this study. Details of material, FSW and EBW machines, welding parameters, temperature measurement using infra-red thermography, post weld heat treatments and dimensions of FSW tools are given. Details of different characterization techniques, mechanical testing methods, operating conditions and analysis procedures employed in this study are described.

Chapter 4 presents the **"Results and discussion"** of the current thesis work. Section 4.1 deals with the "Effects of tool rotational speed on microstructure and mechanical properties of friction stir welded RAFM steel". This chapter also discusses the usage of thermography to measure the interface temperatures on varying rotational speed. The stir zone (SZ) microstructures have been characterised using field-emission scanning electron microscopy (FE-SEM), electron backscatter diffraction (EBSD) and transmission electron microscopy (TEM) techniques. This chapter is based on the journal article, *Vijaya L. Manugula, Koteswararao V.Rajulapati, G.Madhusudhan Reddy, R. Mythili and K. Bhanu Sankara Rao, Materials and Design, 92 (2016) 200-212.*

Section 4.2 provides a detailed description on the "Influence of rotational speed and post weld heat treatments on microstructure and mechanical properties of friction stir welded INRAFM steel**"** .This chapter is based on the journal article, *Vijaya L. Manugula, Koteswararao V.Rajulapati, G.Madhusudhan Reddy, R. Mythili and K. Bhanu Sankara Rao, Metallurgical and Materials Transactions A, 48(2017) 3702-3720.*

Section 4.3 discusses the "Role of section thickness in FSW of INRAFM steel on microstructure and mechanical properties". This study suggests that tool geometry has to be properly designed for different thicknesses and FSW parameters for each thickness are to be separately established.

Section 4.4 describes the "Role of evolving microstructure during EBW on the mechanical properties in the as-welded and post weld heat-treated states". This chapter is based on the journal article, *Vijaya L. Manugula, Koteswararao V.Rajulapati, G.Madhusudhan Reddy, and K. Bhanu Sankara Rao, Material Science and Engineering A,698 (2017)36-45.*

Chapter 5 presents the "**Summary"** of important conclusions of this study and also identifies the **future directions** for further studies.

References

1. T.Noda, F.Abe, H.Araki, M.Okada, Development of low activation ferritic steels, Journal of Nuclear Materials,141-143(1986)1102-1106.

2. S.Jitsukawa M. Tamura, B.Van der Schaaf, R.L. Klueh, A. Alamo, C. Petersen, M. Schirra, P. Spaetig, G.R. Odette, A.A. Tavassoli, K. Shiba, A. Kohyama, A. Kimura, Development of an extensive database of mechanical and physical properties for reduced-activation martensitic steel F82H, Journal of Nuclear Materials,307–311(2002)179–186

3. R.L.Klueh, E.E.Bloom, The development of ferritic steels for fast induced radioactive decay for fusion reactor applications, Nuclear Engineering and Design, 2(1985)383-389.

4. R.L Kleuh, D.R.Harries, High chromium (7-12%Cr) ferritic and martensitic steels for nuclear applications, ASTM monograph, ASTM International (2001)3

5. A.F.Tavassoli, Present limits and improvements of structural materials for fusion reactors –A review, Journal of Nuclear Materials, 302(2002)73-88.

6. B.Raj, K.Bhanu Sankara Rao, A.K.Bhadhuri, Progress in the development of reduced activation ferritic-martensitic steels and fabrication technologies in India, Fusion Engineering and Design, 85(2010)1460-1468.

7. K.Laha, A Saroja, A Moitra, R.Sandhya, M.D.Mathew, T.Jayakumar, E.Rajendra kumar, Development of India-specific RAFM steel through optimisation of tungsten and tantalum contents for better combination of impact, tensile, low cycle fatigue and creep properties, Journal of Nuclear Materials, 439(2013)41-50.

8. Ravikirana, Study of Transformation Characteristics and Microstructural Evolution in 9Cr Reduced Activation Ferritic/Martensitic Steel Using Electron Microscopy, Calorimetry and Computational Methods, Ph.D. Thesis, Homi Bhabha National Institute, August 2014.

9. J.A.Francis, W.Mazur, H.K.D.H.Bhadeshia, Type IV cracking in ferritic power plant steels, Material Science and Technology, 22(2006)1387-1395.

10. K.Laha, K.S.Chandravathi, P.Parameswaran, and K. Bhanu Sankara Rao, Type IV cracking susceptibility in weld joints of different grades of Cr-Mo steel, Metallurgical and Materials Transactions, 40A (2009)386-397.

11. S.K.Albert, M.Matsui, T.Watanabe, H.Hongo, K.Kubo, M.Tabuchi, Variation in the Type IV cracking behaviour of a high Cr steel weld with post weld heat treatment, International Journal of Pressure Vessel and pipes, 80 (2003) 405–413.

12. S.Sam, C.R Das, V.Ramasubbu, S.K.Albert, A.K.Bhaduri, T.Jayakumar, E.Rajendra kumar, Delta-ferrite in the weld metal of reduced activation ferritic martensitic steel, Journal of Nuclear Materials, 455 (2014) 343-348.

13. K.Anderko, L. Schafer, E. Materna-Morris, Effect of the δ-ferrite phase on the impact properties of martensitic chromium steels, Journal of Nuclear Materials, 179-181 (1991) 492-495.

14. R.S.Mishra, Z.Y.Ma, Friction stir welding and processing, Material Science and Engineering, R50 (2005) 1-78.

Chapter 2- Literature review

2.1. Development of ferritic-martensitic steels for nuclear applications

The increasing global demand for energy and the absolute necessity to reduce emissions of global warming gasses by more than half in less than 50 years are providing an opportunity to depart from more abundantly used environmentally harmful fossil-fuel combustion for generation of electricity. Many countries are exploiting alternate sources of energy in order to bring down green-house gas emissions that are causing concern with respect to global warming. Although renewable energy sources like solar, wind etc. offer a possibility of clean energy, there exist various concerns on economic efficiency and reliability when used for base load power generation. Nuclear power is being considered as one of the options. Many of the nuclear power stations operating today rely on fission reaction associated with splitting of the nucleus of heavy elements that are either uranium or plutonium. Another important approach for usable energy production is by nuclear fusion reaction which gives rise to release of energy when two very light nuclei (isotopes of hydrogen, tritium and deuterium) are brought together to synthesise a heavy and more stable element. Fusion reaction between tritium and deuterium generates a helium nucleus and a single neutron, as well as 17.6 MeV energy. The released energy is taken up by the two new particles, helium and neutron, in inverse proportion to their masses. The fast neutrons are emitted in all directions and are the primary means by which energy leaves the fusion reactor. The high energy neutron irradiation in fusion reactor would lead to changes in nuclide composition of materials being used, and some of the new nuclides generated may be radioactive, activating the materials. The irradiation levels and decay rates of these activated materials are dependent upon the elements used in structural materials.

Therefore, the elements used in structural materials of fusion reactor should meet the criteria of low or reduced activation. These criteria require all materials used in a fusion reactor to be suitable for recycling or disposal in non-active landfills approximately 100 years after removal from the reactor. International collaboration is under progress to build a fusion reactor, the first of its kind, called International Thermonuclear Experimental Reactor (ITER) to demonstrate the scientific and technical feasibility of generating fusion energy [1, 2].

The development of structural materials for the first wall and breeding blanket components of the fusion reactor offers a greater challenge since a very much high energy neutron flux is produced by fusion. The first wall and blanket modules will be exposed to plasma particles and electromagnetic radiation, consequently will suffer from radiation by 14 MeV neutrons [3-5]. Therefore materials for first wall and blanket systems are assessed in terms of strength, efficiency and irradiation embrittlement. A wide range of structural materials have been investigated for manufacturing the first wall and blanket modules to be tested in ITER. The materials considered include austenitic stainless steels, Ni-base superalloys, Ti alloys, copper alloys and chromium alloys [4]. The austenitic stainless steels which were used as the primary material for fast reactor structures have a limitation with respect to void swelling, helium embrittlement, poor thermal conductivity and high co-efficient of thermal expansion. Thorough investigations have constricted the choice of structural materials to ferritic/martensitic steels, Vanadium alloys, and SiC-SiC ceramic composites [6, 7]. Ferritic-martensitic steels were not considered initially for fusion applications because of expected complications that could result from the interaction of ferromagnetic material with the high magnetic fields in a fusion system. However investigations

revealed that possible problems can be handled in reactor design [8]. SiC-SiC ceramic composites and vanadium alloys could become competing candidates because of high temperature properties; however the joining techniques for these materials are still at developmental stage. Furthermore the structural materials used for fabrication of a fusion power plant would have to receive the appropriate code approval for the country in which the plant is being constructed. Out of these three candidate materials, ferritic-martensitic steels have received considerable attention since these alloys possess extensive engineering database on mechanical properties, reasonable understanding on various metallurgical aspects and proven ability to fabricate the components by conventional welding processes such as tungsten inert gas welding and electron beam welding.

The alloy that received most attention in nuclear industry was Modified 9Cr-1Mo-Nb-V-C steel widely known as Grade-91(P-91, F-91, T-91) [7, 9]. Though it was originally developed for steam generator applications in Fast Breeder Reactors, it has been extensively used in fossil-fuel based conventional power plants due to its excellent creep strength and oxidation resistance at reasonably high temperatures, thermal fatigue resistance, adequate fracture toughness under typical service conditions prevailing and good weldability [10-12].

Modified 9Cr-1Mo steel was recommended for use in the normalised and tempered condition. This heat treatment comprises of a solutionising treatment that produces austenite and dissolves the carbides, followed by cooling in air to room temperature. In this state the steel contains martensite, which is brittle. In commercial practice, the normalized steels are tempered by heating between 650°C to 780^{o}C which results in the "tempered martensite" microstructure comprising of a ferrite matrix with carbide precipitates. The majority of carbides are $M_{23}C_6$ rich in Cr and fine MC carbides rich in

V or Nb [11-13]. The Mod.9Cr-1Mo steel has been approved for design by code bodies in USA, Europe and Japan for fission applications [1, 2].

2.2. Development of low/reduced activation ferritic-martensitic steels

As discussed in the previous section, Mod.9Cr-1Mo steels have good swelling resistance, excellent thermal properties, exceptional mechanical properties and good weldability [11, 12]. In spite of its excellent mechanical properties, Mod.9Cr-1Mo was deficient as a structural material for construction of first wall and test blanket modules of the fusion reactors due to the incompetence of satisfying the 'low activation' criterion. The idea of 'low activation' materials was introduced into the international fusion program to facilitate hands-on-maintenance and minimise waste disposal. 'Low activation' materials are the materials that would either not activate when irradiated by neutrons or, if activated, develop low-level radiation that would decay quickly [1, 14]. Low activation materials also calls for environmental effects that will be produced from the disposal of fusion reactor components when they are replaced during operation or following the decommissioning of the plant. The radioactive waste has to be disposed in a safe manner harmless to the environment [14, 15]. The presence of Mo and Nb in the Mod.9Cr-1Mo steel transmutes on neutron irradiation to produce long-lived isotopes and does not satisfy the low activation criterion. The alloy also reveals pronounced shift in the ductile-to-brittle transition temperature after irradiation [16-18].

At present "low-activation" structural material as defined above does not exist. "Reduced-activation" steels, where the radioactivity decays to hand-control level in a relatively short time after its disposal thus minimise the environmental problems, were considered possible and their development was pursued. Reduced activation could be achieved by selection of appropriate alloying elements that has low residual

radioactivity when induced by high energy neutrons and also by control of impurities and tramp elements [1,14,15]. In the development of reduced activation ferritic steels, evaluation of induced activity of several alloying elements is made and found that alloying elements Al, Ni, Cu, Nb, Mo, and Sn which produce long-lived radioactive nuclides are not desirable and needed to be eliminated or minimised [1,18].

Reduced activation ferritic-martensitic steels have been developed by altering the chemical composition of modified 9Cr-1Mo steel. The high induced radioactive elements Mo and Nb are replaced by W and Ta to lower the induced radioactivity. Special efforts were focussed on elimination of Nb because of very low concentration of that element will be required to meet the criteria for shallow land burial or recycle [1, 19]. Further, strict control has also been exercised on the radioactive tramp elements (Mo, Nb, B, Cu, Ni, Al, Co, Ti) and on the elements that promote embrittlement (S, P, As, Sb, Sn, Zr, O). These elements have been restricted to ppm levels to achieve reduced activation [15] .In addition to satisfying the criteria of reduced activation, these steels also meet the criteria required of conventional Cr-Mo steels for structural applications [18].Investigations reveals RAFM steels have excellent resistance to void swelling [7] and He embrittlement [20-22].In addition these steels also possess good thermo-physical, mechanical properties and good weldability [23-28] .The useful temperature window of RAFM steel is 350^{o}C- 550^{o} C; lower value being limited by the radiation induced embrittlement and upper value is limited by reduction in elevated temperature strength [23]. The operating temperatures could be further enhanced to 650^{o}C with the development of oxide dispersion strengthened (ODS) steel [17, 21, 29]. RAFM steel developed by various countries as a part of international fusion program is given in Table 2.1.The composition of RAFM steel developed by various countries varied slightly with respect to Cr, W and Ta concentrations.

Table 2.1 Nominal composition of reduced -activation ferritic-martensitic steels (wt. %)

Program	Steel	C	Si	N	Cr	W	Ta	V	Mn	Fe	Ref
Europe	Eurofer	0.1	0.05	0.03	8.5	1.0	0.08	0.25	0.5	Bal	[22,30, 31]
Japan	F82H	0.093	0.09	0.002	7.65	2.0	0.04	0.2	0.49	Bal	[19,32]
	JLF-1	0.1	0.2	0.05	9.0	2.0	0.07	0.23	0.54	Bal	[21,33, 34]
USA	9Cr2WV Ta	0.11	0.03	0.022	8.84	1.97	0.06 5	0.18	0.39	Bal	[1,16, 17]
China	CLAM	0.092	0.01	0.02	8.87	1.48	0.12	0.2	0.47	Bal	[35]

India is one of the countries associated with the development and testing of test blanket modules (TBMs) in ITER. India's participation in ITER programme necessitated the development of India-specific RAFM steel for TBM, which is discussed in subsequent section. Based on optimisation experiments, these steels are recommended to be used in normalised and tempered condition and the microstructure reveals fully tempered martensitic structure. The physical metallurgy aspects involving the phase transformations in RAFM steel are briefly discussed in the following section.

2.3. Physical metallurgy of RAFM steel

The γ-Fe loop in the Fe-Cr equilibrium diagram containing 0.1%C shown in Figure 2.1 [2] is closed if the Cr content exceeds about 12%. However the ferrite-forming elements (Cr, V, W, Si) contract the γ- phase field while the austenite stabilizers extend it. The 9-12% Cr steels are fully austenitic or have a duplex (austenite + ferrite) structure at temperatures in the range 850-1200^{o}C [36-38]. Therefore for 9%Cr steels, normalizing heat treatment is carried out below 1200^{o}C to confine to single γ-phase field. The tempering of the martensite is performed below A_{c1} to avoid re-austenization and to achieve good combination of strength and toughness. However the actual phase

diagram is sensitive to alloying elements that may rise or lower the transformation temperatures. The A_{c1} temperature is increased by 30-50^{o}C by eliminating Ni, which reduces the alpha-gamma transformation [30].The increase in tempering temperature is beneficial as it lowers DBTT and minimises stress corrosion cracking. Addition of high chromium or high silicon causes the formation of δ-ferrite during austenitizing around 1100^{o}C. Therefore addition of austenite stabilising elements is required to prevent the formation of δ-ferrite in steels containing chromium concentrations greater than 9%.

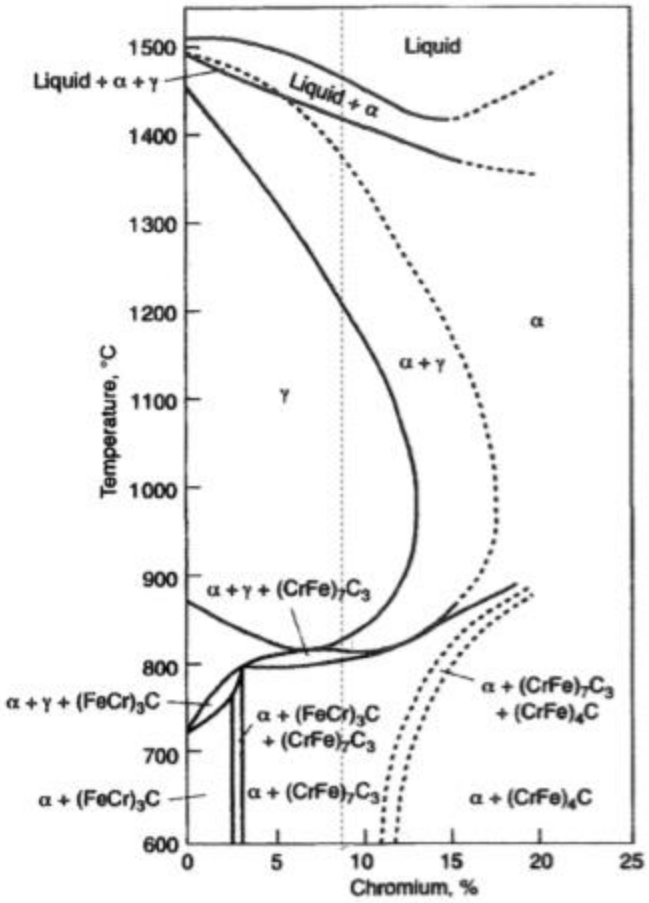

Figure 2.1 Fe-Cr equilibrium diagram containing 0.1%C [2]

Even when there is no δ-ferrite present in the base metal, some amount of δ-ferrite is retained in the weld metal at ambient temperatures depending on the cooling rate and chemical composition. The retention of δ-ferrite in the weld metal and its influence on

mechanical properties were discussed in the subsequent section. The constitution of the steels at room temperatures on cooling from austenite phase field can be predicted using Schalfer-Scheinder diagram .The amount of δ-ferrite that is retained in the weld metal can be calculated from formulas describing difference between Cr and Ni equivalents respectively. Several methods were developed to predict the weld metal microstructures are Schalfer, Scheinder, Kalthauser and Newhouse etc.[36]. J. Onoro investigations revealed that, to obtain completely martensitic microstructure in weld metal, it is necessary to consider Schneider Cr equivalent value lesser than 13.5, and also the difference between the Cr and Ni equivalents to be lesser than 8[36].The Cr equivalent for these steels is given below;

Cr eq = (%Cr) +6%Si+4%Mo+11%V+5%Nb+1.5%W+8%Ti+12%Al.

Ni eq=2Mn+Cu+40C+30N+2Co+4Ni

Some investigations carried out on the occurrence of phase transformations during heating and cooling using dilatometry techniques, revealed that transformation temperatures rise with increase in W and Ta which are ferrite stabilisers [37, 38]. Time-temperature-transformation (TTT) diagrams produced for various grades of RAFM steel reveal that high martensite start (M_s) temperatures for low C containing steel and low M_s for high C/N steels [37].The continuous cooling transformation (CCT) diagrams generated for RAFM steel demonstrates that these steels are air–hardenable and the critical cooling rate for complete transformation to martensite is 50-60 $Kmin^{-1}$ [26].

2.4. Microstructural features of 9%Cr tempered martensitic steels

The high temperature creep strength of structural materials is dictated by its microstructure stability during creep and its effect on creep behaviour. As already discussed in section [2.1], 9Cr ferritic-martensitic steels derive their high temperature

strength from the fully tempered martensitic structure consisting of laths, which contains a high density of dislocations and fine precipitates. The $M_{23}C_6$ carbides are distributed along the prior austenite grain boundaries (PAGBs) and lath boundaries .The MX carbides are distributed at laths, blocks, packet boundaries and PAGBs as well as in the matrix within laths as illustrated in Figure 2.2 [10]. In creep resistant steels containing V and Ta, the MX carbides are rich in V and Ta [32-34]. The $M_{23}C_6$ carbides are rich in Cr and depending on the alloying elements there may be considerable solubility of other elements [39]. The size of $M_{23}C_6$ carbides is usually much larger in the vicnity of PAGBs, about 100–300nm, than that inside grains, 50–70 nm. The size of MX carbonitrides 5–20nm, is much smaller than that of $M_{23}C_6$ carbides.

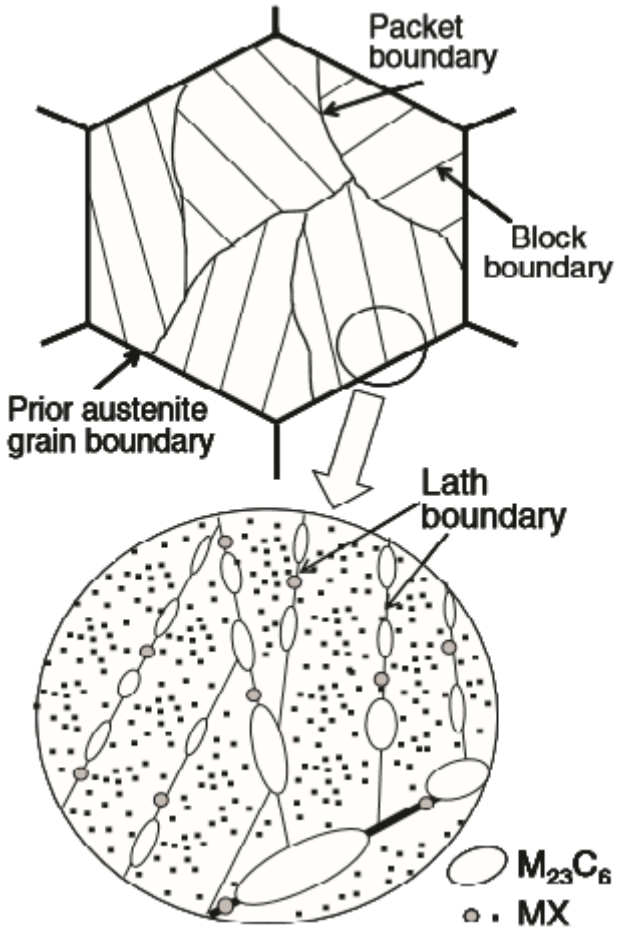

Figure 2.2.Schematic illustration of tempered martensitic structure of 9%Cr steel [10]

2.5. Effect of alloying elements W and Ta on microstructure and mechanical properties:

The alloying elements play a vital role in transformation kinetics and temperature at which transformation takes place. Therefore in the development of RAFM steel the effects of alloying elements W and Ta on the microstructure and mechanical properties of Cr-W base steels have been investigated by Abe and co-workers [6,9,10,34, 40-44]. Figure 2.3 illustrates the effect of W concentration on creep strength and DBTT. The creep rupture strength increases linearly with increasing W concentration up to 2% W, where the steels consisted of single phase martensite.

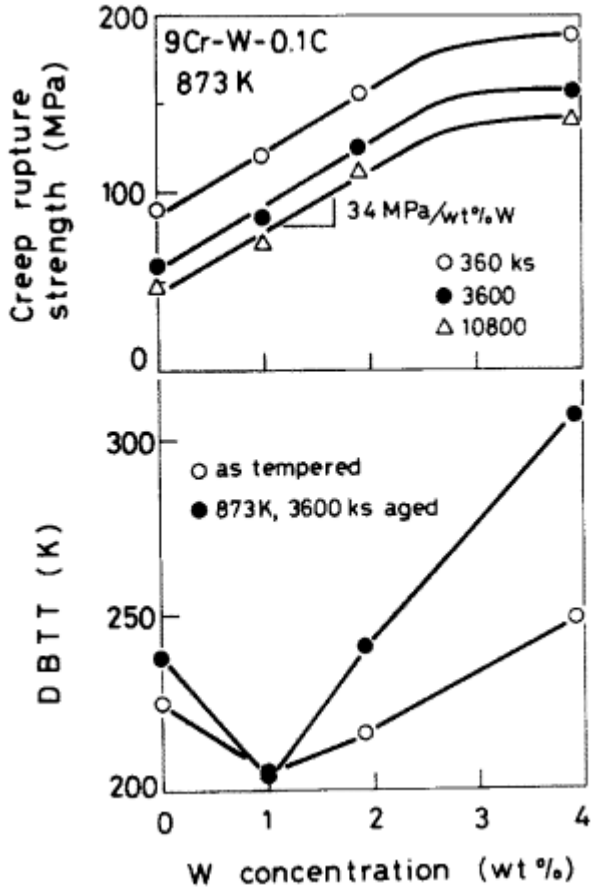

Figure 2.3Variation of creep rupture strength and DBTT as a function of W content[34]

The creep strength hardly increases above 3%, corresponding to two-phase region of martensite and δ-ferrite [43, 44].The δ-ferrite does not contribute to strength.

The strength of steels could be correlated with martensite lath sub-grains. The coarsening of laths indicates a decrease in creep strength because lath boundaries are responsible for strength. Coarsening of laths occurs as a result of migration and annihilation of boundaries. Therefore fine carbides pinning at the grain boundaries and low self-diffusion rates are necessary for decrease in coarsening of lath boundaries and hence improves the creep strength. Tungsten additions are effective in decreasing the self-diffusion rates and therefore decrease the coarsening of lath boundaries as shown in Figure 2.4. The higher DBTT of 9Cr-4W resulted mainly from the presence of δ-ferrite and the precipitation of Fe_2W in δ-ferrite (Figure 2.3). A similar trend was observed with respect to aging temperatures. Figure 2.5 shows the effect of $M_{23}C_6$ and laves phase on DBTT [6]. It is observed that coarsening of $M_{23}C_6$ and laves phase increase the DBTT. Studies on microstructure evolution in RAFM steel reveal that the thermal embrittlement increases with increase in W [42]. As mentioned earlier the prevention of annihilation and migration of martensite lath boundaries during creep is required for better creep strength. The MC type fine carbides are effective in pinning the lath boundaries and therefore contribute to better creep strength. V and Ta are preferred for low activation in RAFM steel to substitute niobium in MC. The coarsening of laths is much lower in steels containing Ta than plain 9Cr steels. It was reported that minor additions of Ta is beneficial to reduce the grain size [23] and also did not cause any degradation in toughness .DBTT of modified steel remained as low as in case of plain steels [33, 40, 45, 46].However increase in Ta up to 0.16% is reported to increase the DBTT and hot cracking susceptibility as shown in Figure 2.6.

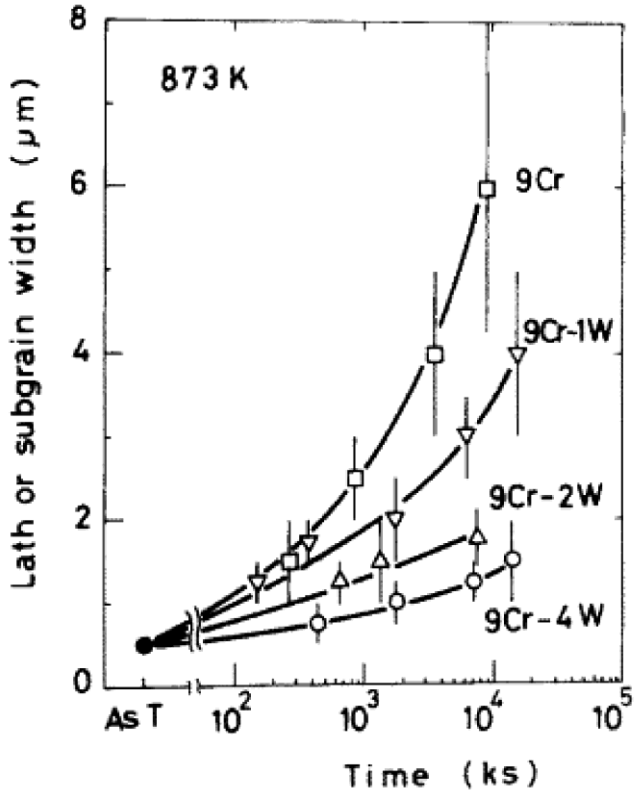

Figure 2.4 Effect of W content on martensite lath width [34].

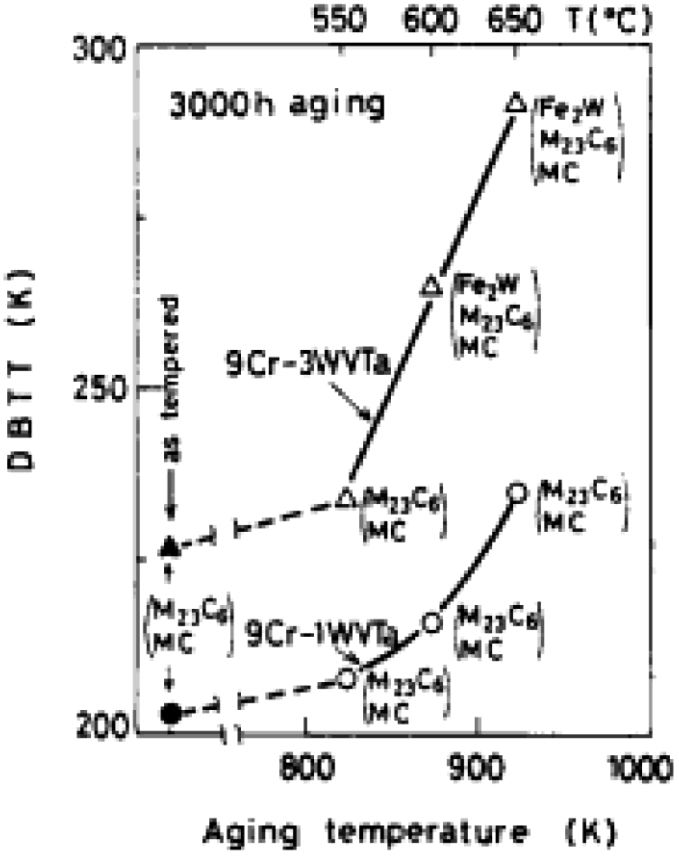

Figure 2.5 Variation of DBTT as a function of W content with aging temperature showing drastic increase in the presence of Laves phase [5]

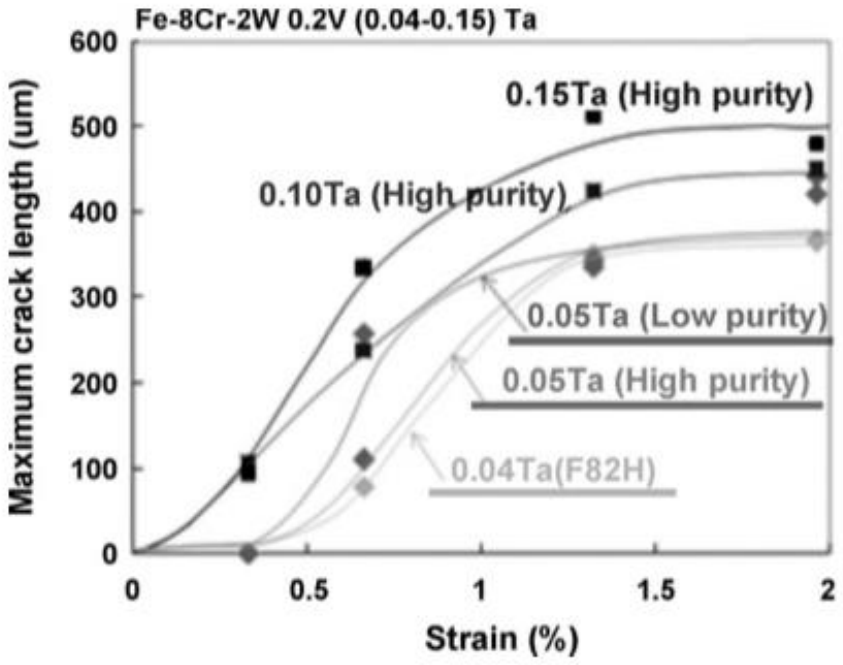

Figure 2.6 Effect of Ta content on hot cracking susceptibility [45]

2.6. Development of India specific RAFM steel

In India, extensive efforts have been made on the development of RAFM steel for Indian TBM to be tested in ITER .The fusion grade steel conforming to Eurofer has been achieved by employing vacuum induction melting followed by vacuum arc refining. This melt route ensured a clean, homogeneous, and segregation free ingots. The specified composition of the different heats was obtained by proper selection of very pure raw materials and completely eliminating the use of any scrap material. Further, strict control was exercised on the radioactive elements Mo, Nb [18,19]. The chemical composition was optimised based on extensive studies on structure-property correlations [47-60]. Four variations of RAFM steel having 1 wt% tungsten with 0.06Ta, 1.4 wt% tungsten with 0.06 Ta, 2 wt% tungsten with 0.06 wt% Ta and 1 wt% tungsten with 0.14 wt% Ta have been produced by Mishra Dhatu Nigam (MIDHANI) Hyderabad, India, in an effort to optimise the chemical composition with the aim of achieving very low DBTT, fine grain size, good impact toughness, low cycle fatigue

and creep properties. The RAFM steel having1.4 wt% tungsten with 0.06 wt% Ta was found to possess better combination of strength and toughness needed for TBM and is designated as India-specific RAFM (INRAFM) steel. The optimum normalising and tempering heat treatment conditions were arrived at based on optimum prior austenite grain size and hardness with austenitizing temperatures and with the duration of tempering temperature. The optimised heat treatment conditions were found to be normalizing at 1253K for 30 min and tempering at 983 K at 60 min [47].

2.6.1. Phase transformation temperatures in INRAFM steel

The phase transformation temperatures in INRAFM steel was determined by using Setaram Sestys 1600 heat flux Differential Scanning Calorimetry (DSC) employing plate type transducer[50]. DSC measures the difference in heat flow between the sample and a reference material (usually empty alumina crucible), when both are heated or cooled at a pre-set heating or cooling rate [58]. The absorption or evolution of heat due to the phase change in the material induces a change in the differential heat flow between the sample and reference, which appears as an uncompensated temperature differential ΔT. The martensite start M_s and martensite finish M_f temperatures for 1.4W INRAFM steel is 645 ± 5 K and 583 ± 5 K respectively. The typical DSC thermogram for RAFM steel showing $\alpha \rightarrow \gamma$ transformation is shown in Figure 2.7.The phase transformation sequence reported for this steel on heating at a rate of 1K/min include:α-ferrite (ferromagnetic) + $M_{23}C_6$ + MX→ α-ferrite (paramagnetic) + $M_{23}C_6$ + MX → γ-austenite + $M_{23}C_6$ + MX → γ-austenite + MX → δ + γ + MX → δ + γ → δ + γ + L → δ + liquid → Liquid [49,51,58]. The transformation temperatures determined are given in Table 2.2

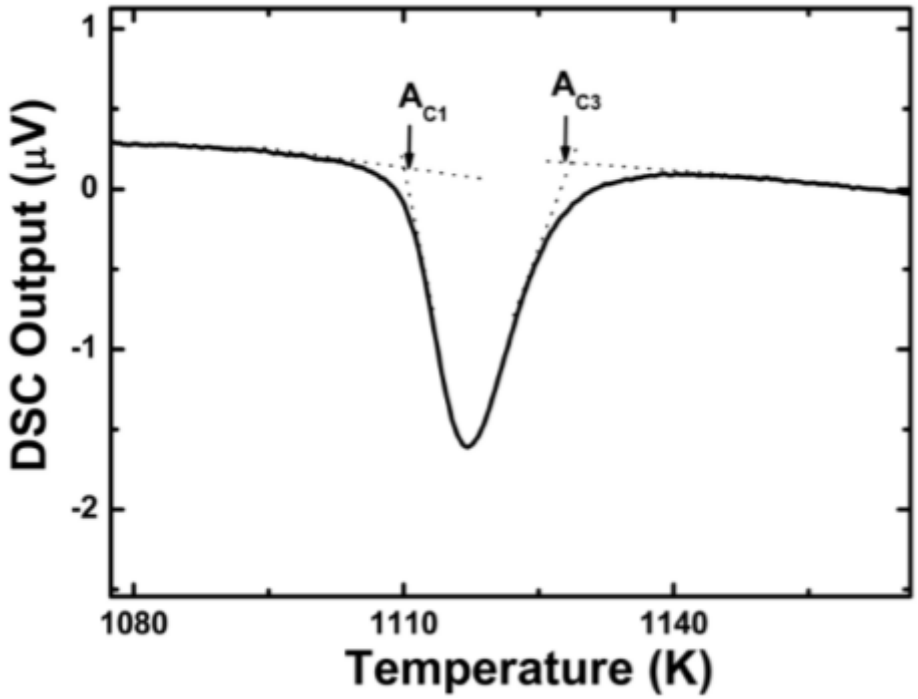

Figure 2.7 Typical DSC thermogram for RAFM steel showing α→γ transformation [58]

Table2.2 Transformation temperatures (K) [50]

Description of phase change	Transformation Temperature (K)
ά (martensite) →α(ferrite)+ $M_{23}C_6$	918±5
T_c, Curie temperature	1027±5
α+ MX+ $M_{23}C_6$→α+γ +MX+ $M_{23}C_6$ (A_{c1})	1091±5
α+γ+ MX+ $M_{23}C_6$→ γ+ MX+ $M_{23}C_6$ (A_{c3})	1130±5
γ + MX+ $M_{23}C_6$→ γ + MX	1342±10
γ + MX→ δ + γ + MX	1494±10
δ + γ + MX→ δ + γ	1563±15
δ + γ → L+ δ + γ	1762±15
L+ δ+ γ →L + δ	1767±15
L+ δ→ L	1791±15

2.7. Development of fabrication technologies for TBM:

In the development of RAFM steel for first wall and breeding blanket system emphasis was laid on high temperature strength, physical properties and weldability [2, 21, 24, 26]. The first wall of blanket is exposed to the fusion plasma, and it is subjected to 0.5 MW/m of heat from plasma and high neutron load. The blanket system design requires demonstrating, the capability to extract heat deposited by fusion neutrons and to reproduce Tritium. Therefore the first wall, with built-in cooling channels has been adopted in the blanket design [61-63]. As a result the blanket design develops into complex structure with a variety of tubes, plates, pipes required for its fabrication.

The usage of newly developed alloy; RAFM steel and the innovative design of the blanket system call for utilization of various fabrication technologies. The parts will be joined by either welding and or hot isostatic pressing (HIP) methods [63-68]. It was demonstrated that the HIP technology is mature enough to make a full scale first wall and cooling channels. Welding technology has gained maturity and various welding processes developed for conventional ferritic-martensitic steels are basically applicable for RAFM steels. The welding processes that are considered for RAFM steels include tungsten inert gas (TIG), electron beam welding (EBW), LASER etc. [68-76]. Some data has also been generated on post irradiation effects on welded joints [77].

2.7.1. Welding metallurgy of high chromium ferritic-martensitic steels

In general the fusion weld joint of ferritic/martensitic steel have distinctive features i.e., fusion zone (FZ), heat affected zone (HAZ) consisting of a range of microstructures [2, 71]. This complex HAZ occurs because of the phase transformations that occur upon heating /cooling during the weld thermal cycle as shown in Figure 2.8.The occurrence of various zones illustrated in the Figure 2.8 are discussed as follows.

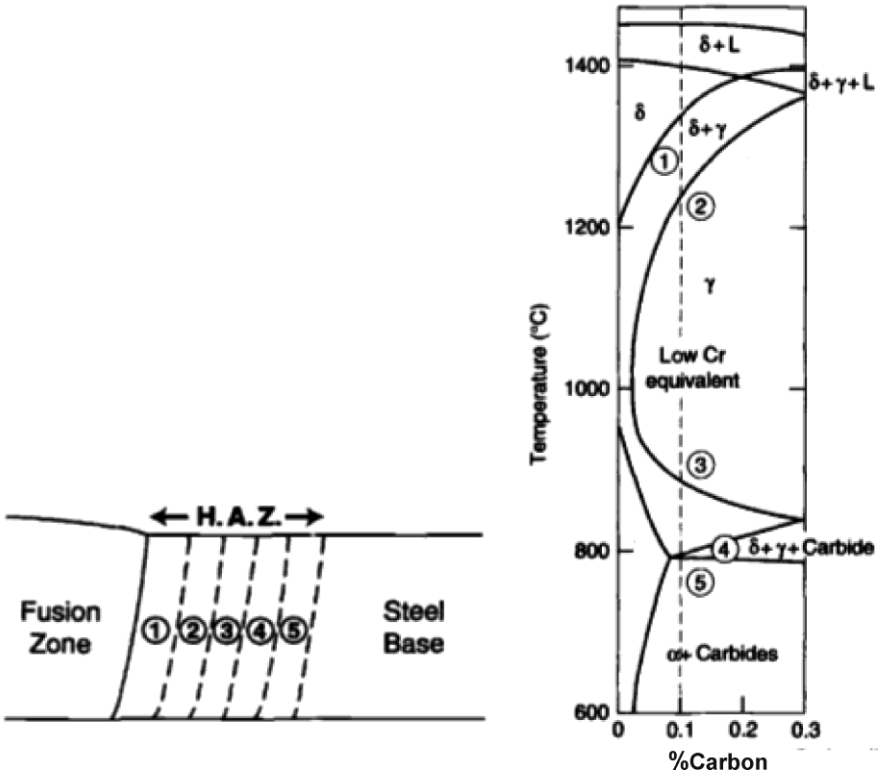

Figure 2.8 Schematic diagram illustrating various zones in a high Chromium ferritic–martensitic steel fusion welded joint and the relationship with the HAZ regions observed [2]

Where T = temperature achieved during welding

T_m = melting point of steel

$T_{\gamma\delta}$ = temperature at which γ→δ transformation is complete on heating

T_T = original tempering temperature of steel

A_{c1} = temperature at which α→γ transformation starts on heating

A_{c3} = temperature at which α→γ transformation is complete on heating

Fusion Zone –The peak temperature experienced in this zone is above the melting temperature (T>Tm), and δ-ferrite is the first phase to form during solidification of the molten weld metal. The δ-ferrite to austenite transformation occurs on further cooling and the austenite transforms to martensite on cooling below the M_s temperature. Some δ-ferrite is retained in the fusion zone at ambient temperature, even when there is no δ-ferrite present in the base and filler wire materials, as complete transformation to

austenite does not occur during cooling ,at the fast cooling rates associated with the welding process.

HAZ--Region 1- The peak temperatures experienced in this region are in (T_m>T> $T_{\gamma\delta}$).This region consists of martensite and δ-ferrite. The δ-ferrite is formed along the prior austenite grain boundaries as this region is heated into the two-phase (γ+δ) field during welding; some of the δ-ferrite is again retained at ambient temperature adjacent to the fusion line as a result of the rapid cooling after welding. The width of this region increase with increasing welding heat input.

HAZ--Region 2 – This region is heated into the higher temperature part of the γ-phase field during welding, and experience temperatures ($T_{\gamma\delta}$>T>A_{c3}).Therefore the prior existing carbides dissolve, resulting in coarse prior austenite grains and subsequent cooling results in fully martensitic microstructure .

HAZ--Region 3 --This region, which is heated into the lower temperature part of the γ-phase field ($T_{\gamma\delta}$>T>A_{c3}), is again martensitic, but it is finer grained than Region 2. The temperature is not high enough to dissolve all the prior existing carbides; therefore the undissolved carbides prevent grain growth.

HAZ-Region 4-The temperatures experienced in this region is (A_{c3}>T>A_{c1}) which is in the intercritical zone. The partial transformation to austenite and additional tempering of the original tempered martensite structure of the base steel occur during heating in this region, with the austenite again transforming to martensite on cooling. Therefore the microstructure consists of un-tempered and over-tempered martensite.

HAZ-Region 5–The temperature experienced in this region is (A_{c1}>T>T_T). Therefore original tempered martensite in this narrow zone is further tempered during welding. Fusion welding in particular requires post weld heat treatment (PWHT) to temper the

brittle martensite; therefore both welding and PWHT determine the strength of the weld joint.

2.7.2. Post weld heat treatments

Post weld heat treatments are employed to reduce the residual stress levels, temper the martensite in FZ and HAZ and improve the toughness .The Holloman Jaffe parameter P, which involves both temperature T and time t, is used to compare the response of steel to tempering treatment. The value of P 21 and above, indicates satisfactory tempering of the weld metal.

$$P=T\,(\log t+c)\times 10^{-3}$$

T is exposure temperature in Kelvin

t is the exposure time in hours

c is a constant that depends on the composition of the steel

From the plots of hardness Vs Holloman Jaffe parameter the post weld tempering temperature and time are optimised [13, 25].

2.7.3 Effect of δ-ferrite on mechanical properties of ferritic-martensitic steels:

As discussed in the previous section the FZ contains some δ-ferrite that could not transform to austenite during cooling from the liquid phase because of faster cooling rates associated with the welding process. Delta-ferrite contains no carbides, no sub grains and low density of dislocations .These factors promote poor toughness for ferrite matrix of δ-ferrite compared to tempered martensite which consists of laths, blocks, packets and substructures [6, 9].Delta-ferrite in tempered martensite deteriorates the

impact toughness of the steel [78-80] raises DBTT and also results in degradation of creep rupture strength [36].

2.7.4 Type IV cracking in ferritic–martensitic steels

Ferritic-martensitic steel welded joints, under some conditions may result in a locally soft zone that could affect the mechanical properties. Hardness distributions revealed that this locally soft zone was found to occur at the outer edge of the HAZ close to BM. The welded joints have shown degradation in mechanical properties and led to premature failures during high temperature creep. This type of failure is commonly known as Type-IV cracking [81-91].The cracking of the welded joints is usually classified according to the position of the crack as shown in Figure 2.9. Type-I and Type-II modes refer to, the occurrence of crack within the weld metal, the former confined to the weld metal whereas the latter may grow out of the weld into the HAZ. Type-III cracking occurs in the coarse grained region of the HAZ and Type-IV cracking occurs in the fine grained, soft intercritical HAZ [81,83].

As discussed in section [2.7.1] the weld joint obtained in fusion welding processes containing the fusion zone, HAZ and base metal have distinct microstructures as a result of phase transformations that occur during the weld thermal cycle, leading to significant variation in mechanical properties. As the distance from the fusion line towards the base metal increases, the peak temperature decreases.

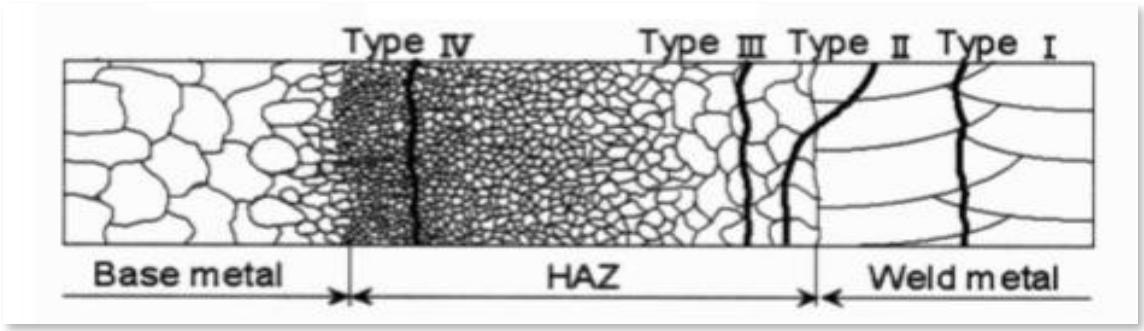

Figure 2.9 Schematic showing the types of cracking of welded joints.

The outer portion of the HAZ adjoining the base metal experience temperatures between A_{c3} and A_{c1} i.e., in the intercritical region .The ferrite that had been re-austenitized on intercritical heating transformed into martensite on cooling and the untransformed ferrite merely undergo extensive tempering. The temperatures in the intercritical range are not expected to dissolve the pre-existing carbides significantly, therefore could be coarsened by Ostwald-ripening mechanism; the relatively coarser particles increase in size at the expense of the relatively fine particles. Therefore, the austenite formed on the intercritical heating had lower carbon content in solution than that expected from the normal austenitizing where the majority of the prior-existing carbides dissolve. The low-carbon austenite transforms into martensite on subsequent cooling. During post weld tempering treatment which is carried out at temperatures below A_{c1}, no further secondary precipitation is expected in the heavily tempered ferrite and much less secondary re-precipitation is expected in the martensite derived from the low-carbon austenite. Therefore the above described microstructural features led to an enhanced recovery in the intercritical structure compared to the other regions of the HAZ. Therefore the strength reduction in the intercritical HAZ was associated with the combined effects of coarsening of precipitates and dislocation substructure.

2.8. Welding procedures for RAFM steel

The RAFM steels developed by various countries have been focussed, to develop the welding procedures with the primary objectives to minimise the volume of weld metal and HAZ, reduce distortion and maintain high joint efficiency. The irradiation induced embrittlement in fusion reactor is more severe for welded joints than that of BM, therefore it is beneficial to minimise the volume of weld metal and HAZ. Both fusion and solid state welding processes are considered for joining RAFM steel. The welding methods being explored include tungsten inert gas (TIG), narrow gap tungsten inert gas (NG-TIG), electron beam welding (EBW), friction stir welding (FSW) and laser beam welding (LBW) etc. [68-76,92,93].

As discussed in previous section the fusion weld joints of ferritic-martensitic steels are susceptible to Type-IV cracking, and its occurrence is due to preferential accumulation of creep deformation and cavitation in the soft zone of HAZ /intercritical region. Some investigations have explored the influence of welding processes on the propensity for Type-IV cracking in P91 weld joints. These investigations revealed that decreasing the width of HAZ results in improvement of creep rupture life. Therefore the welding processes employed in the fabrication of structural components of TBMs plays an important role in the width of HAZ formed and thus influence Type-IV fracture [88].

2.8.1. Research on fusion welding of RAFM steel

Some investigations carried out on TIG welding of RAFM's revealed the formation of soft zone in the intercritical HAZ as confirmed by hardness measurements [71, 94]. Thomas Paul et al. investigated the microstructure evolution in various regions of INRAFM steel weldments upon thermal exposure fabricated by TIG welding process [94]. It was observed that the fine-grained HAZ in the weldment was identified as a region prone to failure during long-term service. Some investigations revealed that the

heat input and cooling rates during welding strongly influenced the microstructure evolution and mechanical properties [95, 96]. A variant of TIG welding process called Activated (A)-TIG welding process has been demonstrated to enhance the penetration capability of conventional autogenous TIG welding for plate thickness up to 12mm. Activated flux for RAFM steels was developed to achieve full penetration in 6 mm thick plates in single pass and the microstructure and mechanical properties were assessed [97].Welding consumables have been developed for NG-TIG and TIG welding process [98]. Advancements in various welding processes such as EBW, LASER and LASER-hybrid welding process are in progress including optimisation of PWHTs [92]. It appears that the low heat input welding processes such as EBW and solid state welding processes that produce a very little or no HAZ hold promise for fabrication of TBM.

2.8.1.1. Electron beam welding process

Electron beam welding process utilizes an electron beam, which is emitted from a heated filament of tungsten or tantalum and is directed at a location on the weld joint. The kinetic energy of the electrons is converted into heat as they strike the work piece and melts it. The work piece can be stationary and the beam energy deflected or the work-piece can be traversed along a desired axis of motion. This process is often carried out in vacuum to prevent dispersion of the electron beam. The beam energy melts the material under temperatures near 2700 K, and then a rapid vaporization occurs followed by the resultant coalescence [99]. EBW can be done in two different modes, conductance and keyhole mode.

Conductance mode is mainly applicable to thin materials, in which heating of the weld joint to melting temperature is generated at or below the materials surface followed by thermal conductance throughout the joint for complete or partial penetration. The weld

produced by this method is very narrow. In cases where deep penetration is required the keyhole mode is employed. The concentrated energy and velocity of electrons of the focused beam are capable of subsurface penetration and causes the rapid vaporisation of the material, causing a hole to be drilled through the material. In the keyhole cavity the rapid vaporization and sputtering causes a pressure to develop thereby suspending the liquidus material against the cavity walls. As the hole is advanced along the weld joint by motion of the work-piece, the molten layer flows around the beam energy to fill the hole and coalesce to produce a fusion weld. The hole and trailing solidifying metal resemble the shape of a traditional keyhole. Both the modes have similar aspects such as narrow welds and minimal HAZ. The keyhole weld is considered as a full penetration weld.

2.8.2. Solid state friction stir welding

The peak temperatures attained in solid state welding process are much lower than the melting temperatures of the materials being welded, hence no melting and solidification in the weld joint is involved. This avoids the problems associated with fusion welding such as solidification and liquation cracking, porosity and loss of volatile alloying elements. Since no fusion is involved, much of the thermal contraction associated with solidification and cooling that promotes distortion could be significantly reduced. Friction stir welding (FSW), a solid state welding process is invented at the welding institute (TWI) Cambridge U.K. in 1991. In FSW process a rotating tool containing the shoulder and pin is plunged into the joint between the two flat plates which generate heat due to friction and plastic deformation. The work piece is softened around the tool and the material is transported from advancing side to retreating side [99,100-102].A schematic of the principle of FSW process is shown in Figure 2.10.

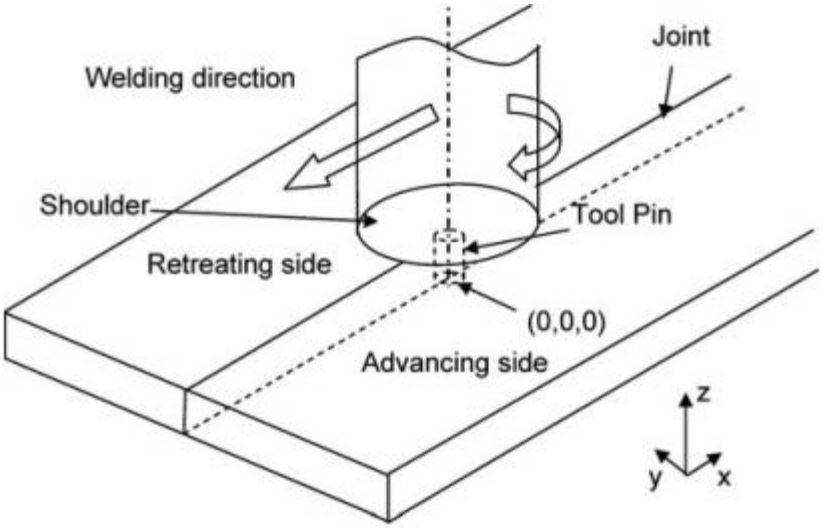

Figure 2.10 Schematic of FSW process[103]

A typical cross-section of the FSW joint consists of a four zones as shown in Figure 2.11. The heat–affected zone (HAZ) is similar to that in conventional welds although the maximum peak temperature is significantly less than the solidus temperature, and the heat source is rather diffuse. This is the zone that does not experience any plastic deformation. The central nugget region is the one which experiences the most severe deformation, and is a consequence of the way in which a tool deposits material from the front to the back of the weld. The thermo-mechanically affected zone (TMAZ) lies between the HAZ and weld nugget; the grains of the original microstructure are often in a deformed state and effected by thermal gradients.

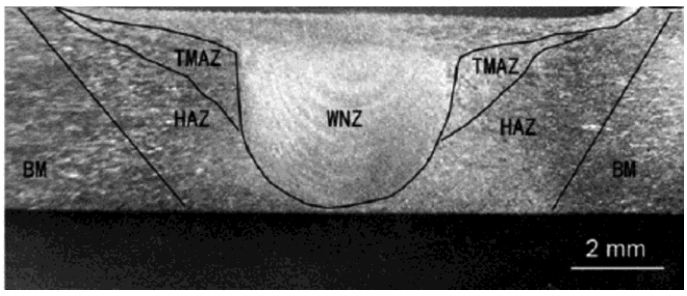

Figure 2.11Typical cross-section of the FSW joint.[102]

Though the application of friction stir welding process has been demonstrated successfully to joining of various aluminium alloys; however the wide usage of FSW in the fabrication of steels was hindered by non-availability of a suitable tool material.The tool material should have higher melting point than the work material, and shall possess a good combination of strength and toughness, thermal and chemical stability and oxidation resistance [104,105].

2.8.2.1. Tool materials

Tool consists of a shoulder and a probe which can be integral with the shoulder or as a separate insert possibly of a different material .The design of the shoulder and the probe is very important for the quality of the weld. The probe of the tool generates the heat and stirs the material being welded but the shoulder also plays an important part by providing additional frictional treatment as well as preventing the plasticized material from escaping the weld region. The plasticized material is extruded from the leading to the trailing side of the tool but it is trapped by the shoulder which moves along the weld to produce a smooth surface finish. The FSW tool is subjected to severe stresses and high temperature particularly during the welding of hard alloys. With the development of new generation tool materials FSW has potential applications for joining of high temperature materials such as steels, nickel -base superalloys and titanium alloys [106].

Polycrystalline cubic boron nitride (PcBN) tool

PcBN tool is selected as potential tool material for FSW of high strength alloys because of its high temperature strength, superior wear resistance and abrasive properties. The properties of PcBN tool is given in Table 2.3.High thermal conductivity of PcBN aids in the design of liquid cooled tools therefore avoids the formation of hot spots on tools. The low coefficient of friction for PcBN results in the occurrence of smooth weld

surface. However, the tool is very expensive due to high temperatures and pressures required in the manufacturing of the tool.

Table 2.3 Properties of PcBN tool and other tool materials for FSW [107].

Properties	PCBN	Tungsten carbide	4340 steel
Hardness (VHN)	2600-3500	1300-1600	280
Coefficient of Thermal expansion ($10^{-6}K^{-1}$)	4.6-4.9	4.9-5.1	11.2-14.3
Thermal Conductivity ($Wm^{-1}K^{-1)}$	100-250	95	48
Coefficient of friction	0.10-0.15	0.2	0.78
Tensile strength(MPa)	-	1100	620
Fracture toughness(MPa√m)	3.5-6.7	11	100
Transverse rupture strength(MPa)	500-800	2200	-
Compressive strength(MPa)	2700-3500	6200	690

2.8.2.2. Research on friction stir welding of steels

With the development of Poly Crystalline Cubic Boron Nitride (PcBN) tools, FSW of steels is now receiving considerable attention .The microstructure evolution in FSW of steels is quite complex unlike aluminum alloys, due to the occurrence of phase transformations that can cause multiphase microstructures. The microstructure evolution in FSW of steels is related to composition of the BM and cooling rate. The major parameters that control the heat input in FSW are tool rotational speed, tool traverse speed, axial force, shape of tool and tool material. Out of these, the variation in tool rotational speed is the major parameter that determines the peak temperature and cooling rate achieved during FSW [103].

In recent years FSW has been successfully used to join various steels including carbon steels [108-110], low alloy steel grade DH36 used for ship building [111,112],

maraging steel for aerospace applications [113] and ferritic stainless steel [114-116], austenitic steels [117,118] and ODS steels [119,120]. Some attempts have been made in the past to demonstrate the feasibility of producing clean welds on high chromium ferritic-martensitic steel by FSW process [121-127]. However a critical assessment of the microstructure evolution in various zones of RAFM steel friction stir weld joint with respect to variation in rotational speeds and its influence on mechanical properties and temperature measurement in SZ has not yet been reported in literature.

References

1. R.L.Klueh, E.E.Bloom, The development of ferritic steels for fast induced radioactive decay for fusion reactor applications, Nuclear Engineering and Design 2 (1985) 383-389.

2. R.L Klueh, D.R .Harries, High chromium (7-12%Cr) ferritic and martensitic steels for nuclear applications, ASTM monograph, ASTM International (2001) 3.

3. N.Baluc, R.Schaublin, P.Spatig, M.Victoria, On the potentiality of using ferritic/martensitic steels as structural materials for fusion reactors, Nuclear Fusion, 44 (2004) 56-61.

4. A.F.Tavassoli, Present limits and improvements of structural materials for fusion reactors –a review, Journal of Nuclear Materials, 302 (2002) 73-88.

5. H.Bolt, A.Brendel, D.Levchuk, H.Greuner, H.Maier, Materials for the plasma facing components of fusion reactors, Energy Materials, 1 (2006) 121-126.

6. F.Abe, H.Araki, M.Okada, Development of reduced activation 9Cr steels for fusion reactors, Journal of Nuclear Science and technology, 31 (1994) 279-292.

7. R.L.Klueh, Ferritic steel for next–generation reactors, Journal of Nuclear Materials, 371 (2007) 37-52.

8. S.N.Rosenwasser, P.Miller, J.A,Dalessandro, W.E.Toffolo, W.Chen, The application of martensitic stainless steels in long life time fusion first wall/blankets Journal of Nuclear Materials, 85-86 (1979) 177-182.

9. F.Abe, S.Nakazawa, Microstructural evolution and creep behaviour of Bainitic, martensitic and martensitic-ferrite dual phase Cr-2W steels, Material Science and Technology, 8 (1992) 1063-1069.

10. F.Abe, Precipitate design for creep strengthening of 9%rempered martensitic steel for ultra-supercritical power plants, Science and Technology of Advanced Materials, 9 (2008) 1-15.

11. V.K.Sikka, Development of Modified 9Cr-1Mo steel for elevated temperature Service, Proceedings, AIME topical conference. Ferritic Alloys for use in nuclear energy technologies, Snowbird, Utah (1983) Eds. J.W.Davies, D.J.Michael, 317-327.

12. V.K.Sikka, Substitution of modified 9Cr-1Mo steel for austenitic stainless steel, in American Society for Metals Workshop on Conservation and Substitution Technology for Critical Materials, Nashville, TN, USA. 1981.

13. J.M.Vitek, R.L.Klueh, Precipitation reactions during heat treatment of Ferritic steels, Metallurgical Transactions, 14A (1983) 1047-1055.

14. G.J. Butter-worth, Objectives and prospects for low-activation materials, Journal of Nuclear Materials, 179-181 (1991) 135-142.

15. G.J. Butterworth, L. Giancarli, Some radiological limitations on the compositions of low-activation materials for power reactors, Journal of Nuclear Materials, 155-157 (1988) 575-580.

16. J.F. Salavy, I.V. Boccacini, P. Chaudhuri, S. Cho, M. Enoeda, L.M. Ginacarli, R.J. Kurtz, T.Y. Loo, K. Bhanu Sankara Rao, C.P.C. Wong, Must we use ferritic steel in TBM?, Fusion Engineering and Design, 85(2010) 1896-1902.

17. R.L. Klueh, D. S. Gelles, T.A. Lechtenberg, Development of ferritic steels for reduced activation; The U.S. program, Journal of Nuclear Materials, 141-43 (1986) 1081-1087.

18. R.L.Klueh D.S.Gelles, S.Jitsukawa, A.Kimura, Van der Schaaf, G.R.Odette M.Victoria, Ferritc/martensitic steel-overview of recent results, Journal of Nuclear Materials , 307-311 (2002) 455-465.

19. T.Noda, F.Abe, H.Araki, M.Okada, Development of low activation ferritic steels, Journal of Nuclear Materials, 141-143 (1986) 1102-1106.

20. N.Yamanouchi, M. Tamura, H. Hayakawa, A. Hishinumao, T. Kondo, Accumulation of engineering data for practical use of reduced activation ferritic steel,8%Cr-2%W-0.2%V-0.04%Ta-Fe, Journal of Nuclear Materials, 191-194 (1992) 822.

21. A.Kimura, Current status of reduced activation ferritic/martensitic steel for fusion energy, Materials Transactions, 46 (2005) 394-404.

22. B.Van der Schaaf, D.S. Gelles, S. Jitsukawa, A. Kimura, R.L. Klueh , A. Mo Èslang, G.R. Odette, Progress and critical issues of reduced activation ferritic/martensitic steel development, Journal of Nuclear Materials, 283-287 (2000) 52-59.

23. R.L. Klueh, D.J. Alexander, M.Reith, The effect of tantalum on the mechanical properties of a 9Cr-2W-0.25V-0.07Ta-0.1C steel, Journal of Nuclear Materials, 273 (1999) 146-154.

24. C.A. Wang, R.L. Klueh, B.A. Chin, The weldability of low activation Cr-W steels, Journal of Nuclear Materials, 191-194(1992) 831-835.

25. R.L. Klueh, P.J. Maziasz, Reduced–activation ferritic steels, A comparision with Cr-Mo, Journal of Nuclear Materials, 155-157 (1988) 602-607.

26. S Jitsukawa, M Tamura, B Van der Schaaf, R.L Klueh, A Alamo, C Petersen, M Schirra, P Spaetig, G.R Odette, A.A Tavassoli, K Shibaa, A Kohyamai, A Kimurai, Development of an extensive database of mechanical and physical properties for reduced-activation martensitic steel F82H, Journal of Nuclear Materials, 307–311 (2002) 179–186.

27. S.Jitsukawa, A.Kimura, A.Kohyama, R.L.Klueh, A-ATavvasoli, B. Van der Schaaf, G.R.Odette, J WRensman, M.Victoria, C.Peterson, Recent results of the reduced activation ferritc/martensitic steel development, Journal of Nuclear Materials, 329-333 (2004) 39-46.

28. H.Kayano, H.Kurishita, AKimura, M.Naruyi, MYamazaki, Y.Suzuki, Charpy impact testing using miniature specimen and its application to the study of irradiation behaviour of low activation, Journal of Nuclear Materials, 179-181 (1991) 425-428.

29. A.Kohyama, Y.Kohno, K.Asakura, H. Kayano, R& D of low activation ferritic steels for fusion, Journal of Nuclear Materials,212-215 (1994) 684-689.

30. K.Ehrlich, S.Kelzenberg, H.D.Rohrig, LSchafer, M.Schirra, The development of ferritic-martensitic steels with reduced long term activation, Journal of Nuclear Materials, 212-215 (1994) 678-683.

31. N.Baluc, R.Schaublin C.Bailat, F.Paschoud, M.Victoria, The mechanical properties and microstructure of the OPTIMAX series of low activation ferritic-martensitic steels Journal of Nuclear Materials, 283-287 (2000) 731-735.

32. M.Tamura, H.Hayakawa, M.Tanimura, A.Hishinuma, T.Kondo, Development of potential low activation ferritic and austenitic steels Journal of Nuclear Materials, 141-143 (1986) 1067-1073.

33. M.Tamura, H.Sakasegawa, A.Kohyama, H.Esaka, K.Shin, Creep deformation of iron strengthened by MX type precipitates, Journal of Nuclear Materials, 329-333 (2004) 328-332.

34. F.Abe, T.Noda, H.Araki, S.Nakazawa, Alloy composition selection for improving strength and toughness of reduced activation 9Cr-W steels, Journal of Nuclear Materials, 179-181 (1991) 663-666.

35. Q.Huang, J.Li, Y.Chen, Study of irradiation effects in China low activation martensitic steel CLAM, Journal of Nuclear Materials, 329–333 (2004) 268–272.

36. J.Onoro, Martensitic microstructure of 9-12%Cr steels weld metals, Journal of materials processing technology, 180 (2006) 137-142.

37. A. Alamo, J.C. Brachet, A. Castaing, C. Lepoittevin, F. Barcelo, Physical metallurgy and mechanical behaviour of FeCrWTaV low activation martensitic

steels, Effects of chemical composition, Journal of Nuclear Materials, 258-263 (1998) 1228-1235.

38. F.B. Pickering, A.D.Vassiliou, Effect of austenitizing temperature on constitution, transformation and tempering of 9Cr-1Mo steel, Metals technology, 7 (1980) 409-413.

39. L.Tan, J.T. Busby, P.J. Maziasz, Y. Yamamoto, Effect of thermomechanical treatment on 9Cr feritic–martensitic steels, Journal of Nuclear Materials, 441(2013)713-717.

40. T. Hasegawa, Y. Tomita, A. Kohyama, Influence of tantalum and nitrogen contents, normalising conditions and TMCP process on the mechanical properties of low-activation 9Cr-2W-0.2V-Ta steels for fusion application Journal of Nuclear Materials, 258-263(1998)1153-1157.

41. F. Abe, T. Noda, H. Araki and M. Okada, Development of Reduced- Activation Mar tensitic 9Cr Steels for Fusion Reactor, Journal of Nuclear Science and Technology, 31(1994) 279-292.

42. F. Abe, H. Araki, T. Noda and M. Okada, Microstructure and Toughness of Cr-Wand Cr-V Ferritic Steel, Journal of Nuclear Materials, 155-157(1988)656-661.

43. F. Abe, H. Araki, T. Noda and T. Noda ,The role of microstructural Instability on creep behaviour of a martensitic 9Cr-2W steel, Metallurgical and Materials Transactions, 23A (1992) 460-477.

44. F. Abe and S. Nakazawa, The effect of Tungsten on creep behaviour of tempered martensitic 9Cr steels, Metallurgical and Materials Transactions, 23A (1992) 3025-3034.

45. H. Ogiwara, H. Mori, H. Tokuichi, K. Saida, K. Nishimoto, H. Tanigawa ,Hot cracking susceptibility of F82H with controlled Ta content, Journal of Nuclear Materials ,417(2011)59–62.

46. H. Hayakawa, A. Yoshitake, M. Tamura, N.Natsume, A. Gotoh, A. Hishinuma, Mechanical properties of reduced-activation ferritic steel :8% Cr-2%W-0.2%V-0.04% Ta-Fe, Journal of Nuclear Materials, 179-181(1991)693-696.

47. B.Raj, K.Bhanu Sankara Rao, A.K. Bhaduri, Progress in the development of reduced activation ferritic martensitic steels and fabrication technologies in India, Fusion Engineering and Design, 85(2010)1460-1468.

48. B.Raj, T. Jayakumar, Development of Reduced Activation Ferritic –Martensitic Steels and fabrication technologies for Indian test blanket module, Journal of Nuclear Materials 417 (2011)72–76.

49. V.Shankar, K.Mariappan, A.Nagesha, G.V.Prasad Reddy, R.Sandhya, M.D.Mathew, T.Jayakumar, Effect of tungsten and tantalum on low cycle fatigue behavior of reduced activation ferritic/martensitic steels, Fusion Engineering and Design, 87(2012)318-324.

50. Ravikirana, Study of Transformation Characteristics and Microstructural Evolution in 9Cr Reduced Activation Ferritic/Martensitic Steel Using Electron Microscopy, Calorimetry and Computational Methods, Ph.D. Thesis, Homi Bhabha National Institute, August 2014.

51. B.Jeya Ganesh, S. Raju, Arun Kumar Rai, E. Mohandas, M. Vijayalakshmi, K.Bhanu Sankara Rao and B. Raj, Differential scanning calorimetry study of diffusional and martensitic phase transformations in some 9 wt-%Cr low carbon ferritic steels, Materials Science and Technology, 27(2011)500-512 .

52. K. Laha, S. Saroja, A. Moitra, R. Sandhya, M.D. Mathew, T. Jayakumar, E. Rajendra kumar, Development of Indian specific RAFM steel through optimisation of tungsten and tantalum contents for better combination of impact, tensile, low cycle fatigue and creep properties, Journal of Nuclear Materials, 439(2013)41-50.

53. J. Vanaja, K. Laha, M.D. Mathew, T. Jayakumar, E. Rajendra Kumar, Effects of tungsten and tantalum on creep deformation and rupture properties of reduced activation ferritic-martensitic steel, Procedia Engineering, 55(2013)271-276.

54. S. Saroja, A. Dasgupta, R. Divakar, S. Raju, E. Mohandas, M. Vijayalakshmi, K.Bhanu Sankara Rao, B. Raj, Development and characterization of advanced 9Cr ferritic/martensitic steels for fission and fusion reactors, Journal of Nuclear Materials, 409(2011)131-139.

55. J. Vanaja, K. Laha, , R. Mythili, K.S. Chandravathi, S. Saroja, M.D. Mathew Creep deformation and rupture behaviour of 9Cr–1W–0.2V–0.06Ta Reduced Activation Ferritic–Martensitic steel, Materials Science and Engineering, 533A(2012) 17–25.

56. G.V. Prasad Reddy, R. Sandhya, K. Laha, M.D. Mathew, An anomalous cyclic stress evolution in reduced activation ferritic/martensitic steel ,Materials Science and Engineering , 527A (2010) 6449–6453.

57. R. Mythili, R. Ravikirana, J. Vanaja, K. Laha, S. Saroja, T. Jayakumar, M.D.Mathew, E. Rajendrakumar, Microstructural modification due to tungsten and tantalum in 9Cr reduced activation ferritic-martensitic steels on creep exposure, Procedia Engineering, 55(2013)295-299.

58. Ravikirana, R. Mythili, S. Raju, S. Saroja, G. Paneerselvam, T. Jayakumar and E. Rajendra kumar, Effect of alloy content on microstructure and microchemistry of phases during short term thermal exposure of 9Cr–W–Ta–0·1C reduced activation Ferritic /martensitic (RAFM) steels, Bulletin of Material Science, 37 (2014) 1453–1460.

59. S. Raju, B. Jeya Ganesh, R. ArunKumar, R. Mythili, S. Saroja, E. Mohandas, M. Vijayalakshmi, K.Bhanu Sankara Rao, B. Raj, Measurement of transformation temperatures and specific heat capacity of tungsten added reduced activation ferritic–martensitic steel, Journal of Nuclear Materials, 389(2009)385-393.

60. M.D.Mathew, J.Vanaja, K.Laha, G.Varaprasad Reddy, K.S.Chandravathi, K. Bhanu Sankara Rao ,Tensile and creep properties of reduced activation ferritic martensitic steel for fusion energy application, Journal of Nuclear Materials 417 (2011) 77–80.

61. M.Akiba, M.Enoeda, S.Tanaka, Overview of the TBM R&D activities in Japan, Fusion Engineering and Design, 85 (2010) 1766-1771.

62. H.Tanigawa, T.Hirose, Technical issues of reduced activation ferritic/martensitic steels for fabrication of ITER test blanket modules, Fusion engineering and design 83(2008)1471-1476.

63. Y.Poitevin, L.V.Boccaccini, M.Zmitko, I.Ricapito, J.-F.Salavy, E.Diegele, F.Gabriel, E.Magnani, H.Neuberger, R.Lässer, L.Guerrini, Tritium breeder blankets design and technologies in Europe: Development status of ITER Test Blanket Modules, test &qualification strategy and roadmap towards DEMO, Fusion Engineering and Design, 85(2010)2340-2347.

64. M.Akiba, M.Enoeda, D.Tsuru, H.Tanigawa, T.Hirose, K.Mohri, Y.Seki, K.Ezato, S.Suzuki, H.Nishi, S.Mori, Development of water-cooled solid breeder test blanket module in JAEA, Fusion Engineering and Design, 84(2009)329-332.

65. T.Hirose, Fabrication of First Wall Component of ITER Test Blanket Module by HIPping Reduced Activation Ferritic/Martensitic Steel Presented at the 2011 International Conference on Hot Isostatic Pressing Kobe, Japan, 12-14, April 2011.

66. H.Hayakawa, Mechanical properties of welded joints of the reduced –activation ferritic steel: 8%Cr W-0.2%V-0.04%Ta-Fe, Journal of Nuclear Materials, 179-181(1991)693-696.

67. T Hirose, Structural material properties and dimensional stability in first wall components of a breeding blanket module, Fusion engineering and design, 83(2008)1176-180.

68. Q.Huang,C.Li,Q.Wu,S.Liu,S.Gao,Z.Guo,Z.Yan,B.Huang,Y.Song,Z.Zhu,.Y.Chen,X. Ling,Y.Wu,FDS Team, Progress in the development of CLAM steel and fabrication of small TBM in China, Journal of Nuclear Materials,417(2011)85-88.

69. M.Rieth, J.Rey, Specific welds for test blanket modules, Journal of Nuclear Materials, 386-388(2009)471- 474.

70. S.Cho, D.H.Kim, M.Y.Ahn, Development of low activation ferritic/martensitic steel welding technology for the fabrication of KO HCSB TBM, Journal of Nuclear Materials,386-388 (2009) 491-494.

71. C.Li, Q.Huang, Q,Wu, S.Liu, Y.Lei, T.Muroga, T.Nagasaka, J,Zhang, J.Li,Welding techniques Development for CLAM steel, Fusion engineering and design, 84(2009)1184-1187.

72. X.Chen,Y.Huang,B.Madigan, J.Zhou, An overview of the welding technologies of CLAM steels for fusion application ,Fusion Engineering and Design, 87(2012) 1639–1646.

73. J.Zhang, B. Huang,Y. Zhai, Overview on the welding technologies of CLAM steel and the DFLL TBM fabrication, Nuclear Materials and Energy,860(2016)1-7.

74. P.Aubert, F.Tavassoli, M.Rieth, E.Diegele, Y.Poetivin, Review of candidate welding processes of RAFM steels for ITER test blanket modules and DEMO, Journal of Nuclear Materials,416(2011)43-50.

75. T.Jayakumar, M.D.Mathew, K.Laha, S.K.Albert, S.Saroja, E.Rajendrakumar, C.V.S.Murthy, G.Padmanabham, G.Apparao, S.Narahariprasad , Reduced activation ferritic martensitic steels and fabrication technologies for Indian TBM in ITER, Fusion Science and Technology,65(2014)171-185.

76. Q. Zhu, Microstructure and mechanical properties in TIG welding of CLAM steel, Fusion Engineering and Design, 86 (2011) 407–411.

77. E. Lucon, A. Leenaers, W. Vandermeulen, Post-irradiation treatment of three EUROFER97 joints, Fusion Engineering and Design, 83(2008) 620– 624.

78. L. Schafer, Influence of delta-ferrite and dendritic carbides on the impact and tensile properties of martensitic chromium steel, Journal of Nuclear Materials 258-263 (1998) 1336-1339

79. K. Anderko, L. Schafer, E. Materna-Morris, Effect of the Delta-ferrite phase on the impact properties of martensitic chromium steels, Journal of Nuclear Materials, 179-181 (1991) 492-495.

80. G.R.Odette. G.E.Lucas, Analysis of cleavage fracture potential of martensitic stainless steel fusion structures: Part II. Fracture analysis procedures for flawed fusion structures Part I Micromechanical models and material properties Journal of Nuclear Materials, 117(1983)276.

81. P.J.Ennis, C-Filemonowicz, Recent advances in creep –resistant steels for power plant applications, Sadhana, 28 (2003) 709-730.

82. P.Parameswaran, K. Laha, K.S. Chandravathi, K. Bhanu Sankara Rao, Microstructural aspects of the causes of Type IV cracking in Cr-Mo steel weld joint, Transactions of the Indian Institute of Metals, 63(2010)479-483.

83. K.Laha, K.S.Chandravathi ,P.Parameswaran, K.Bhanu Sankara Rao, Type IV cracking susceptibility in weld joints of different grades of Cr-Mo Ferritic Steel, Metallurgical and Materials Transactions, 40A(2009)386-397.

84. J.A.Francis, W.Mazur, H.D.K.Bhadeshia, Type IV cracking in ferritic power plant steels, Material Science and Technology 22(2006)1387-1395.

85. P.Mayr, H. Cerjak, The impact of welding on the creep properties of advanced 9-12 % Cr steels, Transactions of the Indian Institute of Metals, 63(2010)131–136.

86. F.Abe, M.Tabuchi, Microstructure and creep strength of welds in advanced ferritic power plant steel, Science and Technology of Welding and Joining 9 (2004) 22–30.

87. M.Tabuchi, M.Kondo, K.Kubo, S.K.Albert, Improvement of Type-IV creep cracking resistance of 9Cr heat resisting steels by boron addition, OMMI 3(2004) 1-11.

88. S.K.Albert, M.Matsui, T.Watanabe, H.Hongo, K.Kubo, M.Tabuchi, Variation in the Type IV cracking behaviour of a high Cr steel weld with post weld heat treatment, International Journal of Pressure Vessels and Piping, 80(2003)405-413.

89. K.Shinozaki, D.J.Li, H.Kuroki, H.Harada, K.Ohishi, Analysis of Degradation of Creep Strength in Heat-affected Zone of Weldment of High Cr Heat-resisting Steels Based on Void Observation ISIJ International, 42(2002)1578–1584.

90. P.J.Ennis, The Mechanical Properties and Microstructures of 9% Chromium Steel P92 Weldments, OMMI, 1(2002).

91. R.Mythili, V.ThomasPaul, S.Saroja, M.Vijayalakshmi, V.S.Raghunathan Microstructural modification due to reheating in multi-pass manual metal arc welds of 9Cr–1Mo steel, Journal of Nuclear Materials, 312 (2003) 199–206.

92. T.Jayakumar, E.Rajendra Kumar, Current status of technology development for fabrication of Indian Test Blanket Module (TBM) of ITER, Fusion Engineering and Design 89 (2014) 1562–1567.

93. Z.Jiang, L.Ren, J.Huang, X.Ju, H.Wu, Q.Huang, Y.Wu, Microstructure and mechanical properties of the TIG welded joints of fusion CLAM steel, Fusion Engineering and Design, 85(2010)1903–1908.

94. V.Thomas Paul, C.Sudha, S.Saroja, Influence of Alloy Content and Prior Microstructure on Evolution of Secondary Phases in Weldments of 9Cr-Reduced Activation Ferritic-Martensitic Steel, Metallurgical and Materials Transactions, 46A(2015)3378-3392.

95. B.Arivazhagan, G.Srinivasan, S.K.Albert, A.K.Bhaduri A study on influence of heat input variation on microstructure of reduced activation ferritic martensitic steel weld metal produced by GTAW process, Fusion Engineering and Design, 86(2011) 192–197.

96. S.Zheng, Q.Wu, Q.Huang, S.Liu, Y.Han, Influence of different cooling rates on the microstructures of HAZ and welding CCT diagram of CLAM steel, Fusion Engineering and Design, 86(2011)2616-2619.

97. P.Vasantharaja, M.Vasudevan, Studies on A-TIG welding of low activation ferritic/martensitic (LAFM) steel, Journal of Nuclear Materials, 421(2012) 117–123.

98. G.Srinivasan, B.Arivazhaghan, S.K.Albert, A.K.Bhaduri, Development of filler wires for welding of reduced activation ferritic-martensitic steel for India's test blanket module of ITER, Fusion engineering and design, 86(2011)446- 451.

99. Schultz, Helmut, Electron beam welding, Cambridge England, Woodhead Publishing, The Welding Institute, 1993, ISBN1-85573-050-2.

100. W.M.Thomas, E.D.Nicholas, J.C.Needham ,M.G. Murch, P.Temple-Smith, G.J.Dawes , Friction stir butt welding (1991), GB Patent No.9125978.8, International Patent No. PCT/GB92/02203.

101. R.S.Mishra, Z.Y.Ma, Friction stir welding and processing, Material Science and Engineering R:Reports, 50(2005)1-78.

102. P.L.Threadgill, A.J.Leonard, H.R.Schercliff, P.J.Withers, Friction stir welding of aluminium alloys, International Material Reviews, 54(2009)49-93.

103. R. Nandan, G.G. Roy, T.J. Lienert, T. Debroy, Three dimensional heat and material flow during FS welding of mild steel, Acta Materialia,55(2007)883-895

104. R. Nandan, T. DebRoy, H.K.D.H. Bhadeshia, ―Recent advances in friction-stir welding—Process, weldment structure and properties, Progress in Materials Science, 53(2008)980-1023.

105.H.K.D.H.Bhadeshia, T. Deb Roy, Critical assessment: friction stir welding of steels, Science and Technology of Welding and Joining, 14(2009).

106.R.Rai, A. De, H.K.D.H. Bhadeshia, T. Deb Roy, Review: Friction stir welding tools, Science and Technology of Welding and Joining, 16(2011)325-343.

107.www.slb.com

108.H.Fujii, L.Cui, N.Tsuji, K.Nogi, Friction stir welding of carbon steels, Materials Science and Engineering, 429A (2006) 50-57.

109.R.Ueji, H.Fujii, L.Cui, A.Nishioka ,K.Kunishige, K.Nogi, Friction stir welding of ultrafine grained plain low-carbon steel formed by the martensite process, Materials Science and Engineering, 423A(2006)324–330.

110.Y.D.Chung, H.Fujii, R.Ueji, K.Nogi, Friction Stir Welding of Hypereutectoid steel below eutectoid temperature, Science and Technology of welding, 47(2007) 299–306.

111.NA McPherson, A.M. Galloway ,S.R .Cater ,S.J .Hambling, Friction stir welding of thin DH36 steel plate, Science and Technology of Welding and Joining, 18(2013)441-450.

112.A.Toumpis, A Galloway, S.Cater, N.A.McPherson, Development of a process envelope for friction stir welding of DH36 steel-A step change, Materials and Design, 62(2014)64-75.

113.S.D.Meshram, G.M.Reddy, S.Pandey, Friction stir welding of maraging steel, Materials and Design, 49(2013)58-64.

114.B.M.Bilgin, C.Meran, The effect of tool rotational speed and traverse speed on friction stir weldability of AISI 430 ferritic stainless steel, Materials and Design, 33(2012)376-383.

115.H-H.Cho, H.Han, S-T,Hong, J-H.Park, Y-J.Kwon, S-H.Kim, R.J.Steel, Microstructural analysis of friction stir welded ferritic stainless steel, Materials Science and Engineering, 528(2011) 2889–2894.

116.J.Han, H.Li, Z.Zhu, F.Barbaro, L.Jiangc, H.Xu, Li.Ma, Microstructure and mechanical properties of friction stir welded 18Cr–2Mo ferritic stainless steel thick plate, Materials and Design, 63(2014)238–246.

117.C.Meran, O.E.Canyurt, Friction stir welding of austenitic stainless steels, Journal of Materials and Manufacturing Engineering,43(2010)432-439.

118. Y.S. Sato, N. Harayama, H. Kokawa, H. Inoue, Y. Tadokoro, S. Tsuge, Evaluation of microstructure and properties in friction stir welded superaustenitic stainless steel, Science and Technology of Welding,14(2009)202-209.

119. B. Baker, L.N. Brewer, E.S.K. Menon, S. Sanderson, Influence of heat input on friction stir welding for the ODS steel MA956, Friction Stir Welding and Processing VII, TMS, January 2013.

120. J.Wang, W.Yuan, S.Rajiv Mishra, Indrajit Charit, Microstructural evolution and mechanical properties of friction stir welded ODS alloy MA754, Journal of Nuclear Materials, 442(2013)1–6.

121. J.-Gu.Lee, M.-K.Lee, C.-K.Rhee, T.-K. Kim, J.-M.Kim, Microstructural evolution as-rolled modified 9Cr-1Mo steel during friction stir welding, International Journal of Material Research, 104 (2013)823-826.

122. Y.Chung H.Fujii, Y.Sun, H.Tanigawa, Interface microstructure evolution of dissimilar friction stir butt welded F82H steel and SUS304, Materials Science and Engineering,52A8(2011)5812–5821.

123. S.Noh, H.Tanigawa, H.Fujii, A.Kimura, J.Shim, T.K.Kim, Microstructural evolutions of friction stir welded F82H steel for fusion applications, Trans. Korean Nuclear Soc. Autumn Meeting, Gyeongju, Korea, October 25-26, 2012.

124. Z.Yu, Z.Feng, D.Hoelzer, L.Tan, M.A.Sokolov, Friction stir welding of ODS and RAFM steels, Metallurgical and Materials Transactions, 2E(2015)164-172.

125. W.Tang, J.Chen, X.Yu, D Frederick, and Z.Feng, Heat input and post weld heat treatment effects on reduced activation ferritic martensitic steel friction stir welds, in R.S. Mishra, M.W.Mahoney, Y.Sato, Y.Hovanski(Eds), Friction stir welding and processing VIII, John Wiley & sons, Inc, New Jersey (2015)83-88.

126. Y.S.Sato, H.Kokawa, H.T. Fujii, Y.Yano, Y.Sekio, Mechanical Properties and Microstructure of Dissimilar Friction Stir Welds of 11Cr-Ferritic/ Martensitic Steel to 316 Stainless Steel, Metallurgical and Materials Transactions, 46A (2015) 5789-5800.

127. Y.S.Sato, H.Kokawa, Y.Yano, Y.Sekio, Mechanical properties of friction stir welded 11Cr-ferritic/martensitic steel, Journal of Nuclear Materials (2012), Article in press.

Chapter 3- Experimental details

3.1. Introduction

The details of the experimental procedures adopted in this study are discussed in this chapter. The composition of the base material, welding processes and parameters, temperature measurement using thermography, details of post weld heat treatments employed, characterisation techniques that includes optical microscopy, field-emission scanning electron microscopy (FE-SEM), electron backscatter diffraction (EBSD)-SEM, and Transmission electron microscopy (TEM) were discussed. Further mechanical property evaluation tests that include Vickers microhardness test, Charpy-V notch impact test and tension test are discussed in the subsequent sections.

3.2. Material

The steel used in this study was supplied by M/s MIDHANI Hyderabad, India. The chemical composition is given in Table 3.1. Alloy was produced by vacuum induction melting followed by vacuum arc refining. Steels were re-melted three or four times to ensure a high degree of homogeneity. Pure raw materials have been used to ensure the purity of the end product. A strict control over radioactive tramp elements (Mo, Nb) and elements which promote embrittlement (S, P) was practiced during the process. The ingots obtained in this process were subsequently rolled and hot forged into 6 and 12 mm thick plates. These hot forged plates have been subjected to a heat treatment following an industrial practice of a normalizing treatment at 1253 K for 30 minutes followed by tempering at 1033 K for 60-90 minutes.

Table 3.1Chemical composition of INRAFM steel (wt.%).

Elements	C	W	Mn	Cr	Ni	S	P	Mo	Ti	Co	V
wt.%	0.1	1.34	0.54	8.97	0.008	0.002	0.004	<0.002	<0.005	0.007	0.23
Elements	Ta	B	Al	Cu	O_2	N_2	Nb	As+Sn+Sb+Zr	Fe	Si	
wt.%	0.066	<0.0001	0.008	<0.002	0.008	0.031	<0.001	<0.03	Bal	0.05	

3.3. Welding processes

In the present study, advanced methods of joining such as friction stir welding (solid-state welding) and electron beam welding (fusion welding) processes were employed.

3.3.1. Friction stir welding process

In the present work rolled plates of 6 and 12 mm thick RAFM steel in as-received (normalized 1253 K for 30 minutes followed by tempering at 1033 K for 60-90 minutes) condition were cut into size 300×150 mm. The surface of the plates was prepared by milling and the plate is rigidly fixed by mechanical clamps in FSW fixture. FSW was carried out in the transverse direction to that of rolling direction of the plate. The tool containing the pin is rotated and plunged into the plate. The tool is protected by an argon gas environment against oxidation due to the high temperatures of the FSW process.The details of FSW machine, welding parameters and FSW tools employed in the study are discussed in subsequent sections.

3.3.1.1. Friction stir welding machine

The friction stir welding machine with a capacity of 200 kN force z-axis (vertical) manufactured by Manufacturing Technology Inc., USA, Model (RM-3-FSW) supplied by Mega Stir Technologies Pvt. Ltd.is shown in Figure 3.1 The machine is capable of welding a variety of materials including Al alloys, Ti, steels and high temperature alloys

using PcBN tools. The machine is designed for advanced research in the field of FSW. The control system represents the latest technology in machine control. Machine movements are accomplished from the HMI and also from the hand held pendant. A provision exists in the machine for supply of shielding gas and chiller which provides the coolant and takes away the warm coolant. The tool head of the machine can accommodate a liquid-cooled tool holder and temperature telemetry system as shown in Figure 3.2. The equipment is instrumented with load cells on tool holder and high frequency online data acquisition system to record spindle speed, spindle torque, positions on x, y and z axis, forces acting on x, y and z directions. Provision is built in the machine for maintaining constant thrust on tool, constant feed along x-axis and position control during welding. This machine is designed for friction surfacing and friction stir welding of plates of aluminium, steel and titanium alloys using appropriate welding tools. The spindle and tool traverse speeds are to be selected depending on the material, its thickness, tool diameter and tool material. The machine is controlled through a PC based system and software. All the parameters such as spindle speed, traverse speed, positions on x, y and z axis, forces acting on x, y and z directions during welding are recorded and can be retrieved.

3.3.1.2. Friction stir welding tools

The friction stir welding tool has a circular shank to which there is a probe or pin with different profiles and geometries. The junction between the cylindrical portion, shank and tool profile is known as tool shoulder. The tools used in this study are PcBN cylindrical tool Q70 grade supplied by MegaStir Technologies Pvt. Ltd. The pin penetrates into the work piece whereas the shoulder rubs with the top surface. The heat is generated primarily by friction between rotating translational tool, the shoulder of which rubs against the workpiece. Frictional heat is generated between the tool and the

workpieces. This heat, along with that produced by the mechanical mixing process and the adiabatic shearing within the material causes the stirred materials to soften without melting. As the tool is moved forward, a special profile on the probe forces plasticised material to the rear where clamping force assists in a forged consolidation of the weld.

Figure 3.1 Photograph of FSW machine used in this study.

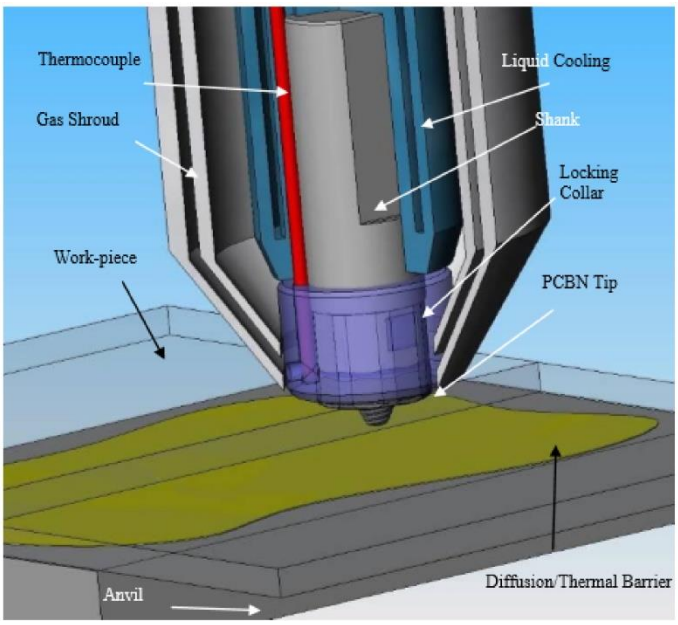

Figure 3.2 Schematic of a tool system depicting FSW tool, liquid-cooled tool holder and a telemetry system

3.3.1.3. To study the effect of tool rotational speed

In this study majority of FSW experiments have been conducted on 6 mm thick plate of INRAFM steel using polycrystalline cubic boron nitride (PcBN) tool at rotational speeds of 200, 300, 500 and 700 rpm with a tool traverse speed of 30mm/min. The profile of the tool and dimensions is shown in Figure 3.3.The tool was tilted by 2 degrees from the plate normal. The tool rotating in anti-clock wise direction is plunged into the plate to a depth of 5.5 mm and moved along welding direction. Based on several trial experiments, the tool traverse speed of 30 mm/min was chosen to minimise temperature gradients, obtain defect-free welds, and avoid tool breakage. The heat input values are computed as per the equation (3.1) [1,2]

Heat input, $H=\varepsilon 2\pi RT/1000V$,

Where ε, a dimensionless factor of FSW process efficiency,

R= rotational speed in rpm,

T= average steady state torque on the tool in N-m, and

V= traverse speed in mm/min (Equation 3-1)

The detailed FSW parameters employed in this study are given in Table 3.2

Table 3.2 The FSW parameters employed in the study of tool rotational speed effects

Tool rotational speed (rpm)	Traverse speed (mm min^{-1})	Heat Input (kJ/mm)
200	30	4.57
300	30	5.27
500	30	5.02
700	30	5.27

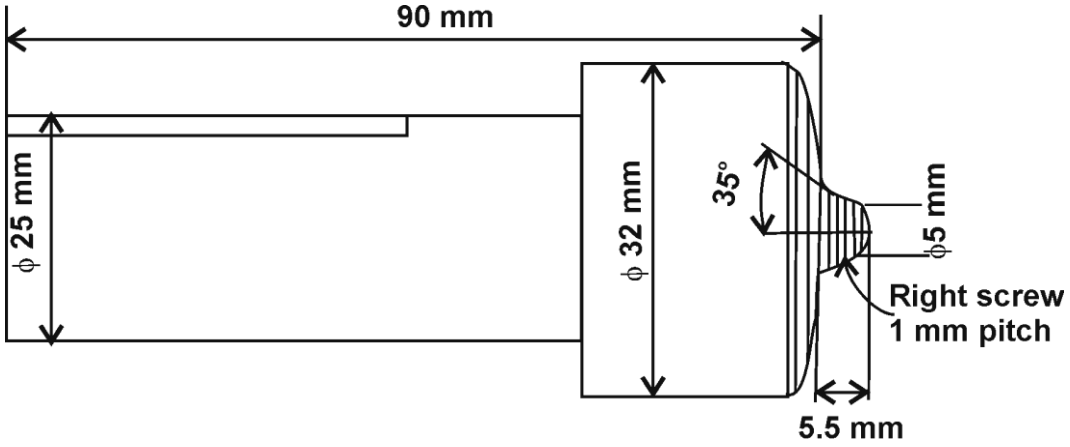

Figure 3.3 Illustrates the profile and dimensions of the PcBN tool employed for 6 mm thick INRAFM steel plate.

3.3.1.4. To study the effect of section thickness on microstructure and mechanical properties

Bead-on-plate welds were made on 150mm×75mm×12mm rectangular plates using polycrystalline cubic boron nitride tool shown in Figure 3.4. The tool was tilted by 2 degrees from the plate normal. The tool rotating in anti-clock wise direction is plunged into the plate to a depth of 11.5 mm and moved along welding direction. FSW was accomplished at 500 and 900 rpm at the tool traverse speed of 20 mm/min to obtain

defect-free welds, and avoid tool breakage. The detailed FSW parameters employed in this study are given in Table 3.3.

Table 3.3. The FSW parameters employed in the study of section thickness effects in FSW of RAFM steel.

Tool rotational speed (rpm)	Traverse speed (mm min^{-1})	Heat Input (kJ/mm)
500	20	11.49
900	20	12.71

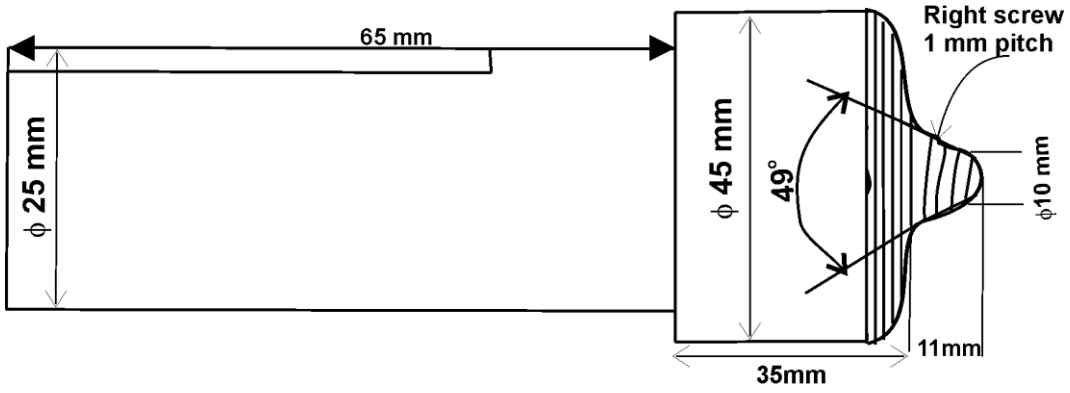

Figure 3.4 Illustrates the profile and dimensions of the PcBN tool employed for 12 mm thick INRAFM steel plate.

3.3.2. Electron beam welding

Autogenous full penetration electron beam welds was carried out on 12 mm -thick plates of INRAFM steel employing Hawker Siddeley Dynamics Eng. Ltd., a high-voltage machine. The welding parameters employed in this study is listed in Table.3.4

Table 3.4 Electron beam welding parameters

Gun voltage	55kV
Welding speed	800 mm/min
Electron beam current	95 m A
Vacuum	10^{-2} m bar

3.4. Temperature measurements-(Thermography)

The temperature was measured by non-contact in-line thermography which enabled to measure the interface temperature between the bottom of the tool shoulder and top surface of the plate conveniently. The experimental set-up is shown in Figure 3.5.The CEDIP Infrared Camera was operated with Indium-Antimony detector with a focal plane array of 350×256 detectors, frame rate of 50 to 380 Hz and accuracy less than 25 milli K at 298 K. Thermal images were acquired at a rate of 50 frames/s. The thermographic calibration of an IR system was based on the measurements obtained on effective blackbody radiance and temperature. Several samples of the INRAFM steel were used for calibration. On each of the samples half-part of the surface was coated with soot using candle, which would act as black body, and other half-part kept uncoated. These samples were kept at different known temperatures in separate furnaces. After achieving the steady temperature in the furnace, images were captured by IR camera lens both in coated and uncoated regions. The difference in temperature obtained between these regions was minimized by adjusting the emissivity in the uncoated region. This corrected emissivity values thus obtained at different temperatures was used to generate the calibration plot of effective blackbody radiance as a function of temperature up to 773 K. The emissivity values of blackbody lies between 0.90-0.92 for the INRAFM steel. The peak temperature attained at a particular speed represents the near surface temperature of the plate. These measurements gave information on peak temperatures attained in the SZ.

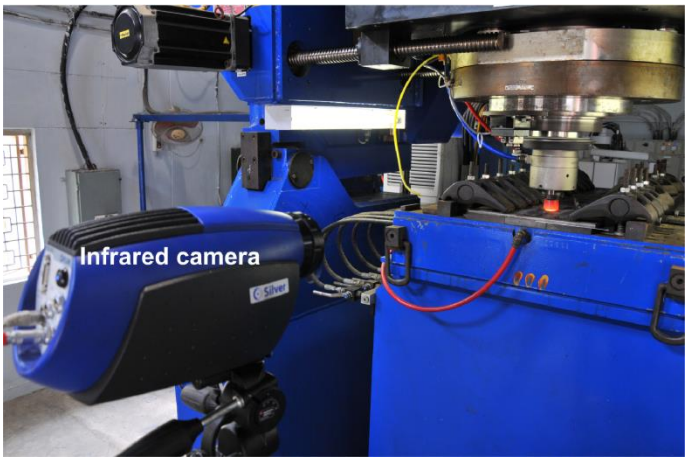

Figure 3.5 FSW experimental set up with Infrared camera arrangement for monitoring interface temperature

3.5. Post weld heat treatments

The FSW and EBW joints were subjected to two types of PWHTs, namely (i) post weld direct tempering (PWDT) at 760^{o}C /90 min, followed by air cooling and (ii) post weld normalizing and tempering (PWNT) comprising of post weld austenitizing at 980^{o}C/30 min followed by air cooling plus tempering at 760^{o}C /90 min and air cooling. Post weld heat treatments were carried out using muffle furnace. The furnace is well calibrated with a temperature accuracy of ± 5 K.

3.6. Microstructural characterization

The metallographic samples of base metal, transverse cross-section of the FSW and EBW weldments have been studied on samples prepared by standard metallographic methods [3].The various regions of the welded sample used for metallography and hardness in case of friction stir and electron beam weldments are shown in Figures 3.6 and 3.7 respectively. The various characterization techniques employed in this study and operation parameters are discussed in subsequent sections.

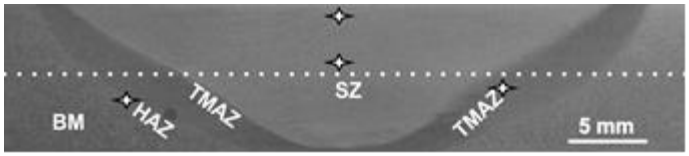

Figure 3.6 Macrograph showing transverse cross-section of friction stir weld joint indicating various zones and the points used for obtaining micro hardness profile. Star marks pertain to the areas where the microstructures are taken in the near-surface and central regions of SZ.

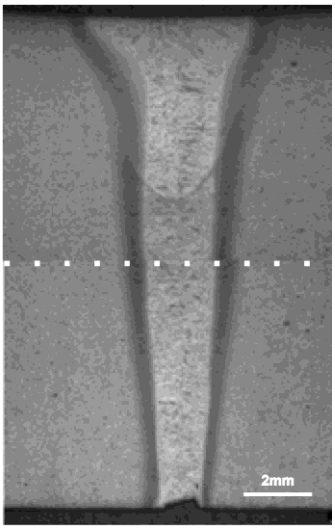

Figure 3.7 Macrograph showing transverse cross-section of electron beam weld joint indicating the points used for obtaining micro hardness profile.

3.6.1. Optical microscopy

Metallographic samples were etched with Villella's reagent (100 ml ethanol, 5ml HCL, and 1 g picric acid) to reveal the microstructure for base metal, various zones in friction stirred and electron beam weldments at various magnifications using optical microscope (LEICA make) .

3.6.2. Field emission-scanning electron microscopy (FE-SEM)

Field emission scanning electron microscopy was carried out using Carl-Zeiss, Merlin Compact FESEM on etched samples to observe the microstructure using secondary electron mode at an accelerating voltage in the range of 10-15 kV. To analyse the fracture surface of weldments the samples were sectioned from impact tested specimens and subjected to ultrasonic cleaning with acetone and observed under SEM at an accelerating voltage of 20 kV.

3.6.3. EBSD-SEM

The EBSD was carried out for measuring the grain size, crystal orientation and grain boundary misorientation. Initially the samples were ground and polished with SiC grit paper and diamond abrasives down to a 3 μm finish and then electropolished in 10% perchloric acid and 90% methanol solution to remove the residual surface damage from the previous polishing. EBSD maps were obtained using FEI quanta 200 HV SEM with TSL EDX OIM system which was operated at an accelerating voltage of 20 kV and measurements were obtained at a step size of 0.1micron and area of 100×100 microns. The sample was tilted at 70 ^{o} with respect to the horizontal during the test. Line intercept method was used for measurement of grain size**.**

3.6.4. Transmission electron microscopy (TEM)

TEM studies were carried out using a Philips CM200 Analytical TEM fitted with Oxford X-Max SDD detector for microstructural and microchemical analysis. The operating voltage used was 200 kV. Samples for TEM examination were sectioned from the top and central regions of the stir zone as shown in Figure 3.6 using slow speed Isomet cutting machine. The slices were mechanically thinned down to 100 microns and 3 mm discs were punched. These discs were electro-polished using Struers Tenupole-5 electropolisher, in a solution containing 90% methanol and 10% perchloric acid, at 15V and 250K, in a twin jet apparatus. Thin foils were examined in an electron microscope operating at an acceleration voltage of 200 kV.

The images were acquired by a bottom mounted on axis TVIPS CCD camera with a resolution of 2048 × 2048 pixels. Analysis of selected area electron diffraction (SAED) and dark field microscopy was carried out to identify the presence of different phases. An aperture of 10 μm size was used for obtaining the SAED pattern and dark field images. A spot size of 50 nm was used to collect the characteristic X-rays from the

constituent phases for determining the composition. A low background single tilt holder was used to reduce the noise due to spurious X-rays.

The martensite lath width and size of different precipitates was deduced from the analysis conducted on several samples. The precipitate size distribution was based on automated image analysis procedure carried out on the bright field images and dark field micrographs acquired with the reflections of the corresponding precipitates in the electron diffraction pattern. For the image analysis, Image J, freely available software was used; 8-10 images in the magnification range of 10000 to 34000X were used for the above analysis.

For indexing electron diffraction patterns, the angles and d-spacing were measured with accuracy of $<1^{o}$ and $0.2A^{o}$ respectively. The measured d-spacing values are compared with standard JCPDS data, the angle between the planes were calculated [4] and matched to measured values.

The composition of coarse $M_{23}C_6$ carbides from the matrix was estimated by EDS spectra and quantified by Cliff-Lorimer method using standard K_{AB} values [5].

The following Cliff-Lorimer equation was used for quantification of the spectra.

$$C_A/C_B = k_{AB} I_A/I_B$$

Where C_A and C_B refer to the concentration of elements A and B in the region of interest and I_A and I_B refer to their respective intensities in the X-ray spectrum.

3.7. Mechanical characterisation

3.7.1. Hardness

Samples used for hardness measurements were mounted and polished by using standard metallographic techniques. The Vickers microhardness profiles were measured at the mid-thickness of the weld on the cross-section perpendicular to the welding direction

employing Mitsuzawa make, MMT-3 model digital microhardness tester. A standard load of 500 g was applied for a dwell time of 20 seconds at a regular interval of 0.5 mm in the case of friction stir welds and 0.1 mm in the case of electron beam weldments. A schematic diagram of hardness survey of the friction stir and electron beam weldments is shown in Figures 3.6 and 3.7 respectively.

3.7.2. Tensile test

The transverse tensile samples were prepared in accordance with ASTM standard E-8. The weld zone was located at the centre of gauge length. Tensile properties were evaluated using Instron 1185 universal testing machine, capacity of 200 kN, at a cross head speed of 1mm/min at ambient temperature. Three samples were tested in each condition for repeatability and an average value of three samples is reported. The geometry and dimensions of the standard tensile specimens of EB weld is shown in Figure 3.8.

3.7.3. Impact test

Impact test was carried out on Tinius Olson machine at ambient room temperature for all conditions. The Charpy samples comprising sub-size (55 mm × 10 mm × 5 mm) and full-size (55 mm × 10 mm × 10 mm) samples were machined as per ASTM standard E-23 employing electric discharge machining (EDM). The V-notch was machined at the weld centre. Charpy impact test blanks were initially profiled using wire to very near final dimensions. The current during EDM was kept very low and other parameters adjusted such that the recast layer would lie always below 20 microns. The final dimensions of impact test samples were obtained by polishing with fine-grit emery papers. Four samples were tested in each condition and an average value is reported. The location and orientation of the notch is shown in Figure 3.9.

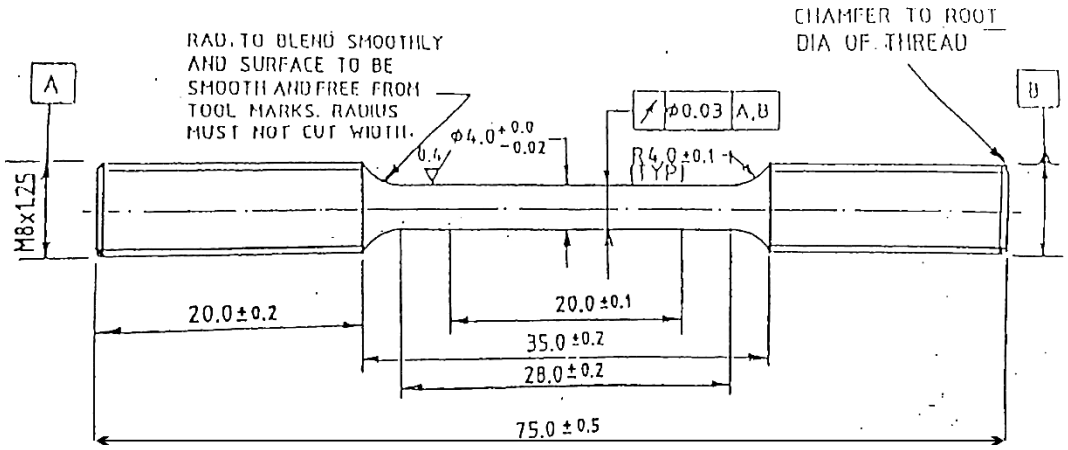

Figure 3.8 Round threaded tensile test specimen .

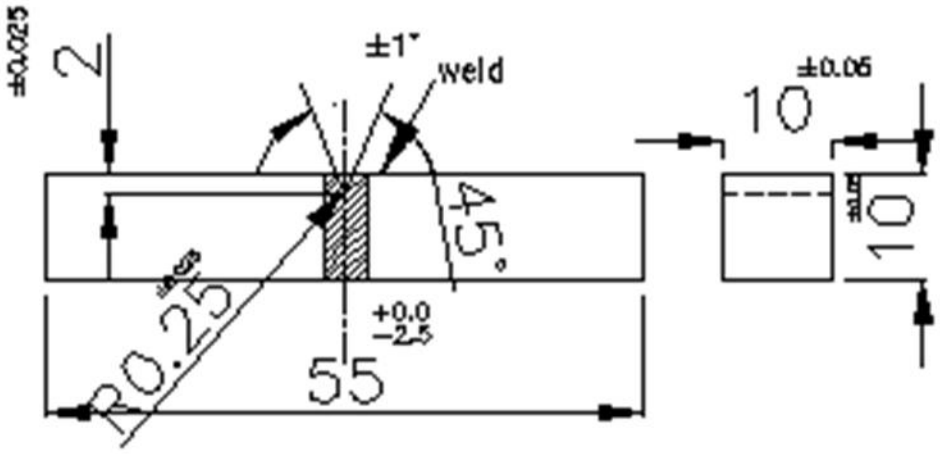

Figure 3.9 Configuration of Charpy –V notch impact test specimen

References

1. N.A.McPherson , A.M.Galloway, S.R.Cater, S.J.Hambling, Friction stir welding of thin DH36 steel plate, Science and Technology of Welding and Joining, 18(2013)441-450.

2. A.Toumpis, A.Galloway, S.CaterS, N.A.McPherson, Development of a process envelope for friction stir welding of DH36 steel-A step change, Materials and Design, 62(2014)64-75.

3. G.F Vander Voort, Metallography principles and practice McGraw Hill book company, (1984)410.

4. Powder diffraction file:Alphabetical indexes inorganic phases, international centre for diffraction data, USA, 1994.

5. G.Cliff, G.W.Lorimer, Quantitative Microanalysis with high spatial resolution M.HJacobsG.W.Lorimer and P.Daig (eds), The metal society London.

Chapter 4- Results and discussion

4.1. Effects of tool rotational speed on microstructure and mechanical properties

4.1.1. Introduction

In general, fusion welding processes develop a wider heat affected zone (HAZ) in ferritic-martensitic steels and generate an inhomogeneous microstructure in the HAZ, resulting in a marked variation in mechanical properties across the weld joint. Premature failures have been noticed very often in the ferritic-martensitic steel weld joints, fabricated with high heat input, due to the pronounced localization of creep deformation and cracking at the parent metal/HAZ interface; these are classified as Type IV cracking failures [1, 2]. Fusion welds are also often containing δ- ferrite that is detrimental for mechanical properties at elevated temperatures [3, 4]. In both these aspects, the solid state friction stir welding holds a key in that it does not produce pronounced heat affected zone and eliminates the δ-ferrite entirely in the weld region since no liquid formation and subsequent solidification is involved. There have been few investigations exploring the possibility of using FSW in case of conventional Ferritic-Martensitic and RAFM steels [5-8]. In general, these investigations have revealed that the microstructure in FSW joint of RAFM steels is composed of SZ, thermo-mechanically affected zone (TMAZ), and HAZ. The microstructures in each of these zones bear no resemblance with one another and could be significantly different from those observed in BM. The current investigation has been conducted with the following objectives: (i) to establish the feasibility of FSW on Indian RAFM steel plate of 6 mm thickness by conducting bead-on-plate experiments, (ii) to study the effect of

rotational speed on the development of the microstructure and hardness in various zones, (iii) demonstrate the usage of on-line thermography to monitor the temperature changes resulting from the variation in rotational speed of tool and (iv) explore the relationship between the microstructures developed across the SZ and their mechanical properties that include hardness and impact toughness .

4.1.2. Process plots and temperature measurement by thermography

FSW was accomplished at 200, 300, 500 and 700 rpm and full penetration defect-free bead-on-plate welds were successfully produced on 300×75×6 mm rectangular plates using PcBN tool under position control of the machine. The process plots, pertaining to the traverse position (X), tool position (Z), feed rate (mm/min), spindle speed (rpm), spindle torque (N-m), Z-force (kN) and X-force (kN) as a function of time, in the FSW experiment conducted with 200,300 rpm and 500,700 rpm are presented in Figures 4.1.1(a, b) and 4.1.2 (a, b) respectively. The analysis of force and torque data revealed that the steady state welding condition is obtained beyond the first 30 mm of welding. The region of steady state condition was also marked by the good quality surface without excessive flash occurrence, and no defects as evidenced by visual examination and metallographic analysis. The samples for metallographic analysis, hardness and impact toughness evaluation were sectioned in the steady state welding region. The temperature was measured by non-contact in-line thermography (Figure 3.5), which enabled to measure the interface temperature between the bottom of the tool shoulder and top surface of the plate. The thermal profiles (time-temperature plots) obtained for 200,300,500 and 700 rotational speeds with respect to tool and interface temperatures are given in Figures 4.1.3 and 4.1.4 respectively. The selection of rotational speeds of 200 rpm, 300 and 500 rpm, and 700 rpm were chosen such that the peak temperature

attained in the SZ during FSW was below A_{c1}, between A_{c1} and A_{c3}, and above A_{c3} respectively.

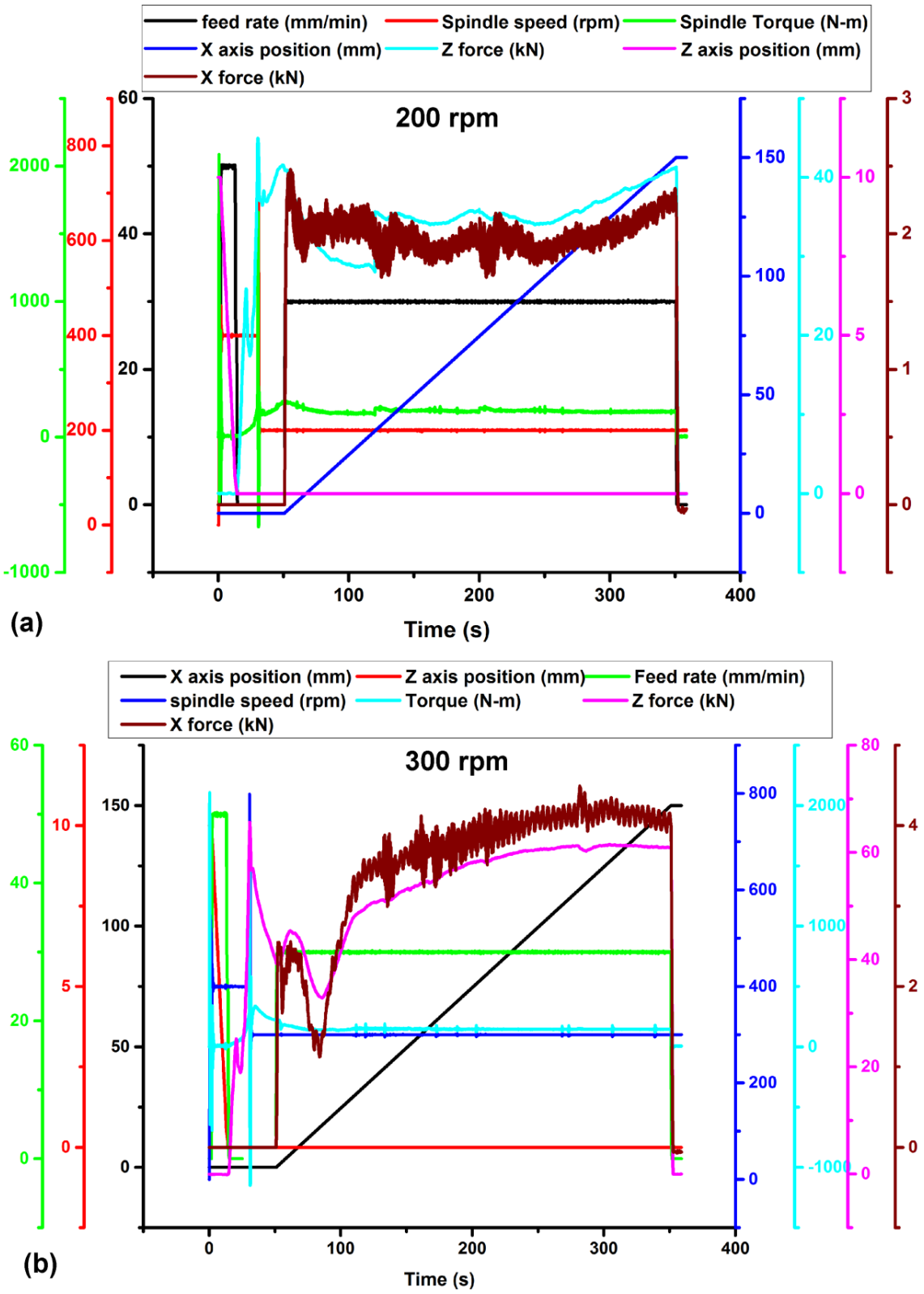

Figure 4.1.1 Process parameters recorded by the welding machine during FSW process (a) 200 rpm and (b) 300 rpm.

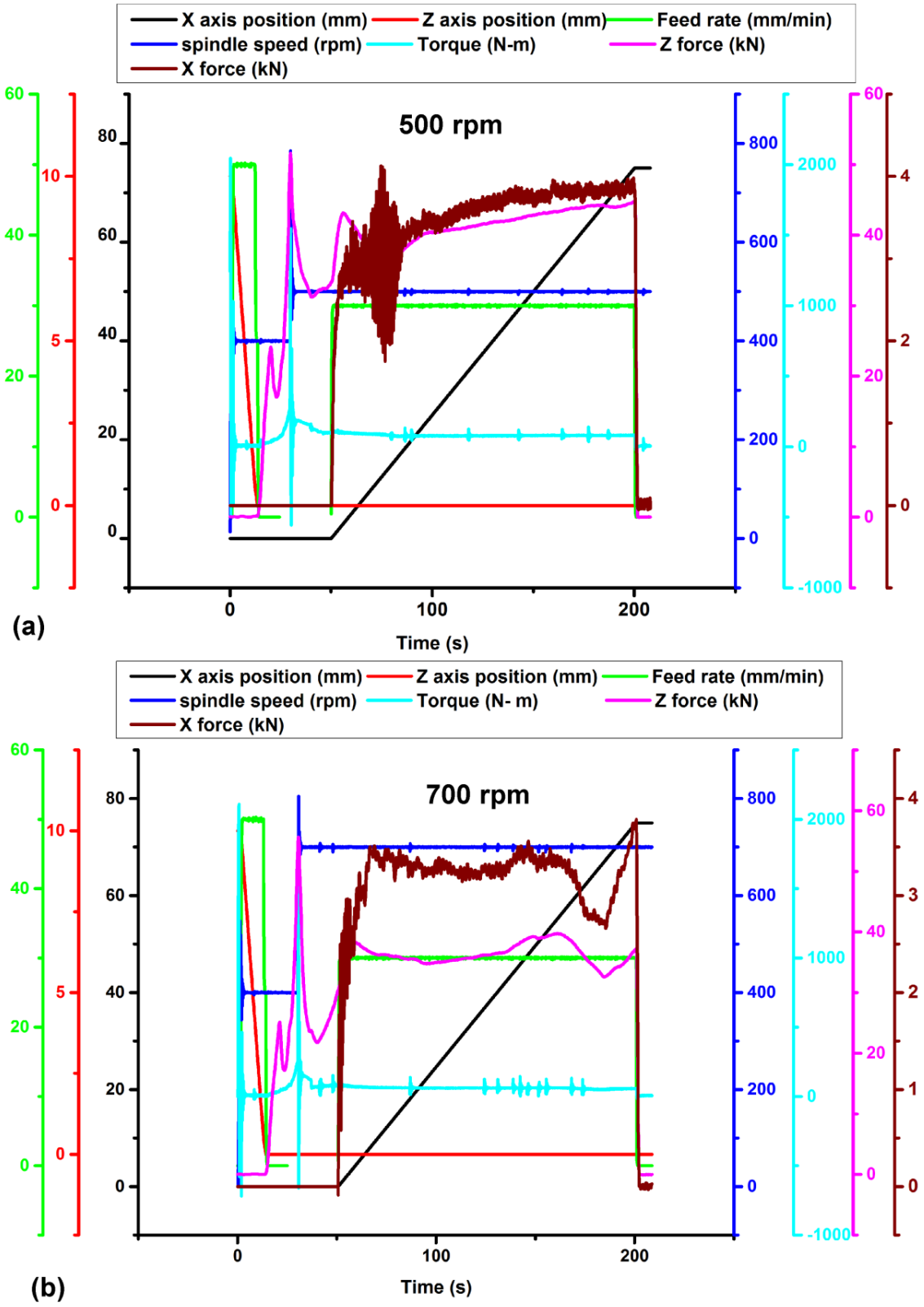

Figure 4.1.2 Process parameters recorded by the welding machine during FSW process (a) 500 rpm and (b) 700 rpm.

The transformation temperatures are recorded in Table 4.1.1[9]. The details of heat input, tool and interface temperatures and their corresponding location w.r.t. transformation temperatures are given in Table 4.1.2. The heat input values recorded in Table 4.1.2 are computed as per the equation given in [10, 11]. The interface temperature between the top surface of the plate and bottom surface of the shoulder varied as a function of heat input which is dependent upon rotational speed. The heat input increased with rotational speed but does not show a linear dependence. Similar observations were reported during FSW of DH36 steel by Toumpis et.al [11]. The photograph of FSW joint for 700rpm is shown in Figure 4.1.5 (a) .The transverse cross-section macrostructure of the FSW joints in all the four conditions as shown in Figure.4.1.5 (b) showed through thickness full penetration welds with no indication of defects. All the conditions displayed SZ (weld nugget), thermo-mechanically affected zone (TMAZ), heat affected zone (HAZ) and base metal. Higher rotational speed led to widening of TMAZ and weld nugget.

Table 4.1.1Transformation temperatures of 9Cr-1.4 W RAFM steel [9].

Melting Temperature	Martensite start M_s	Martensite finish M_f	Recrystallization Temp($0.4T_M$)	Austenite start A_{c1}	Austenite finish A_{c3}
1791 ± 5 K (1518 ± 5 ^oC)	640± 5K (367 ± 5^oC)	583 ± 5K (310± 5^oC)	716 ±5K (443 ±5^oC)	1091±5K (818 ± 5^oC)	1130 ± 5K (857 ± 5^oC)

Table 4.1.2 Details of heat input, tool and interface temperatures w.r.t. transformation temperatures.

Tool rotational speed (rpm)	Tool temp (^oC)	Interface temp(^oC)	Location of Interface temp(^oC)	Heat Input (kJ/mm)
200	650-750	450-500	Below A_{c1}	4.21
300	1000-1050	750-800	Between A_{c1}&A_{c3}	5.27
500	100-1050	800-850	Between A_{c1}&A_{c3}	5.07
700	1150-1200	950-1000	Above A_{c3}	5.27

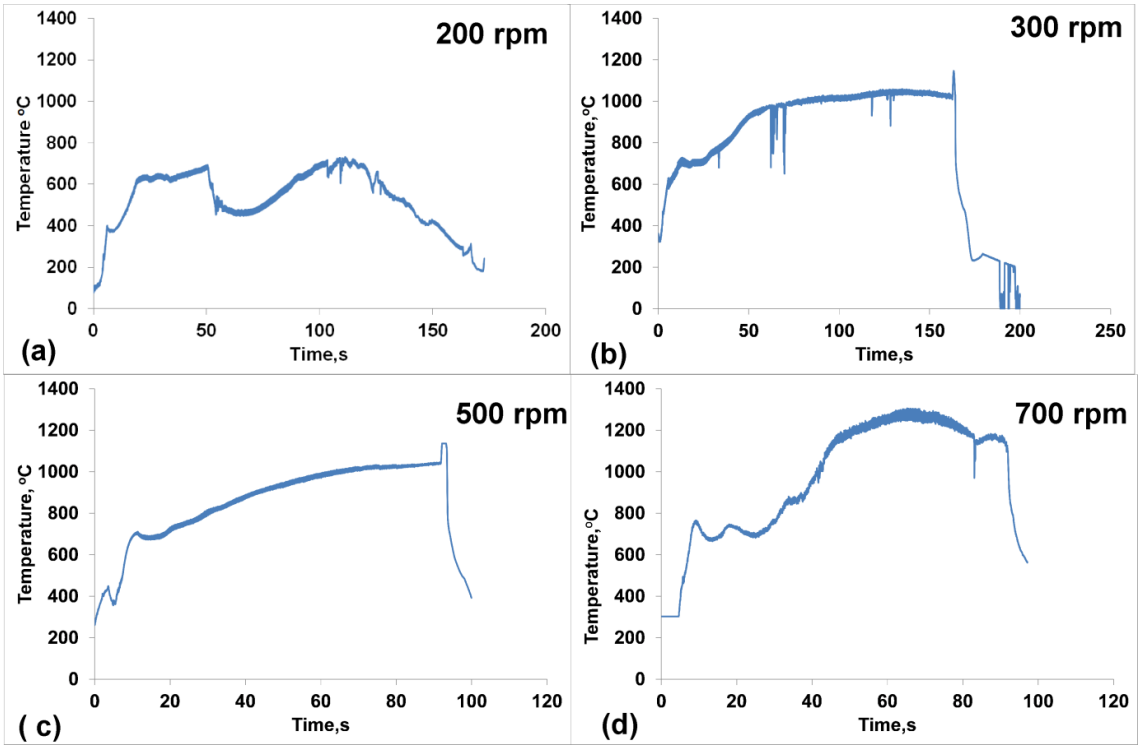

Figure 4.1.3 Thermal profile obtained from tool (a) 200 rpm (b) 300 rpm (c) 500 rpm and (d) 700 rpm.

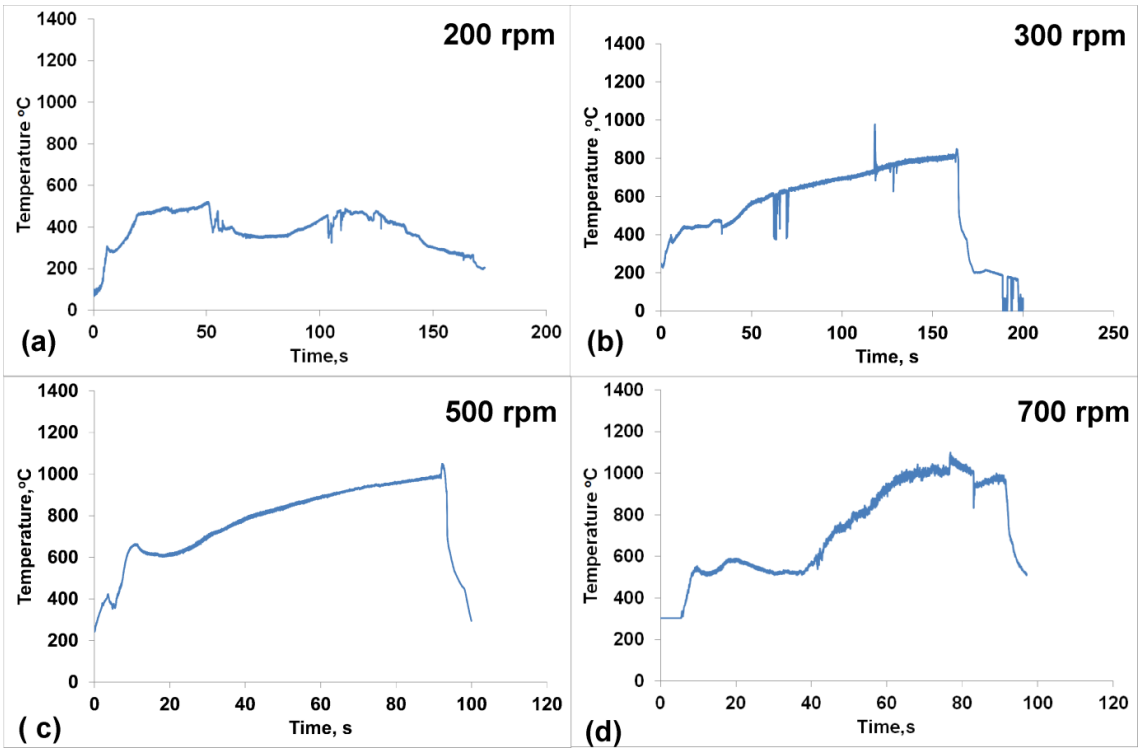

Figure 4.1.4 Thermal profile obtained from the interface (a) 200 rpm (b) 300 rpm (c) 500 rpm and (d) 700 rpm

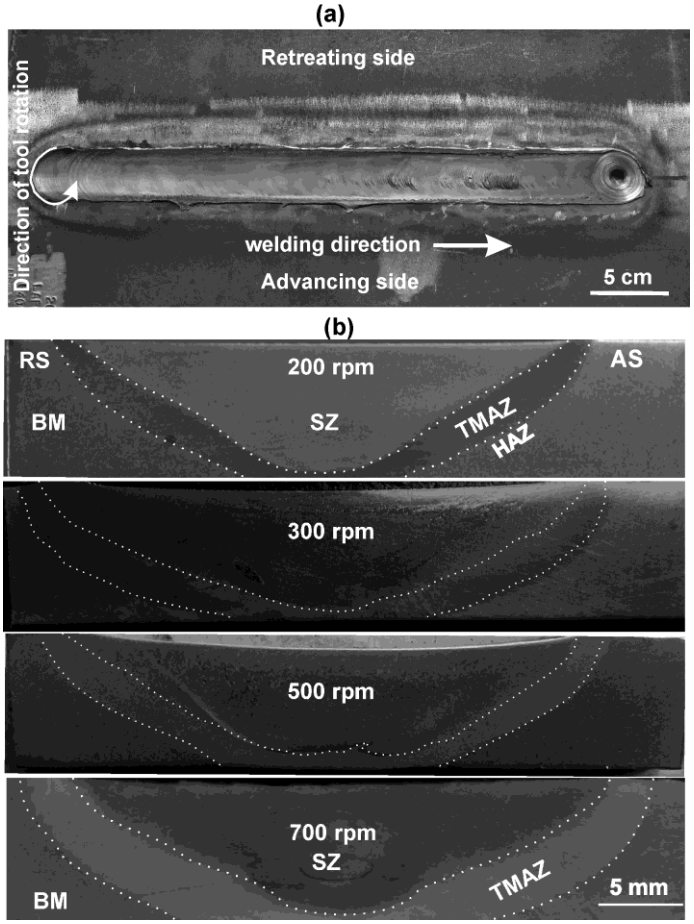

Figure 4.1.5 (a) Macrograph of bead- on- plate friction stir weld at 700 rpm describing advancing side (AS), retreating side (RS) and direction of tool rotation.(b) Macrographs of transverse cross section of FSW samples.

4.1.3. Microstructure (Base metal)

The optical and SEM microstructure of base metal in normalised and tempered condition revealed both intra- and inter-granular precipitation, as shown in Figure 4.1.6(a, b). The TEM micrographs as shown in Figure 4.1.7 confirmed precipitation of relatively coarse chromium and tungsten rich $M_{23}C_6$ type carbides on prior austenite grain boundaries and martensite lath boundaries (arrow marked in Figure 4.1.7 (a)) while finer particles observed in the intra-lath regions corresponded to Ta, V rich MX type of precipitates (circled in Figure 4.1.7 (a)). The SAD patterns from $M_{23}C_6$ and MX along $[\bar{8}\ 3\ 3]$ and $[\bar{2}\ 2\ 3]$ zone axis respectively are shown in Figure 4.1.7 (c, d). The average prior austenite grain size was found to be 6 µm. The martensite lath size varied between 300 to 700nm with an average of 400 nm.

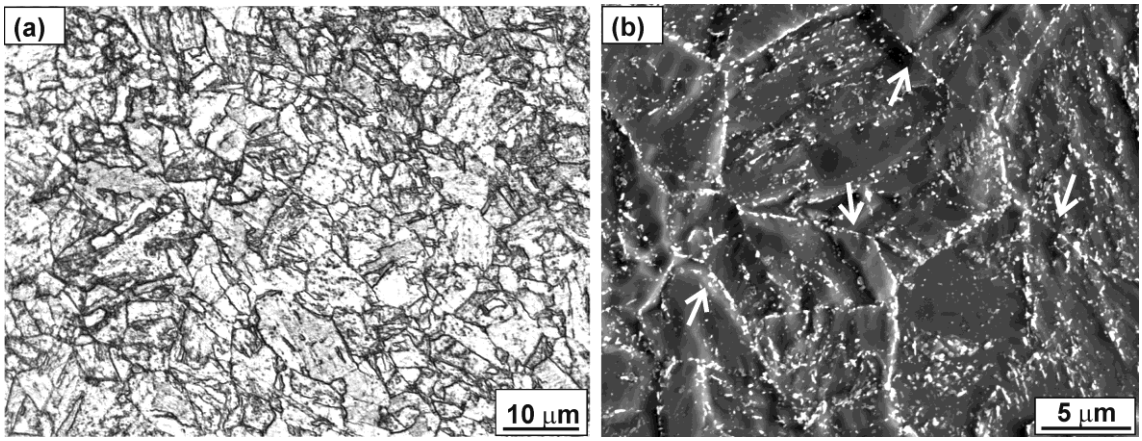

Figure 4.1.6 Microstructure of RAFM steel in normalised and tempered condition. (a) Optical microstructure. (b) SEM microstructure illustrating the precipitation of carbides on PAGBs and in intra-granular regions.

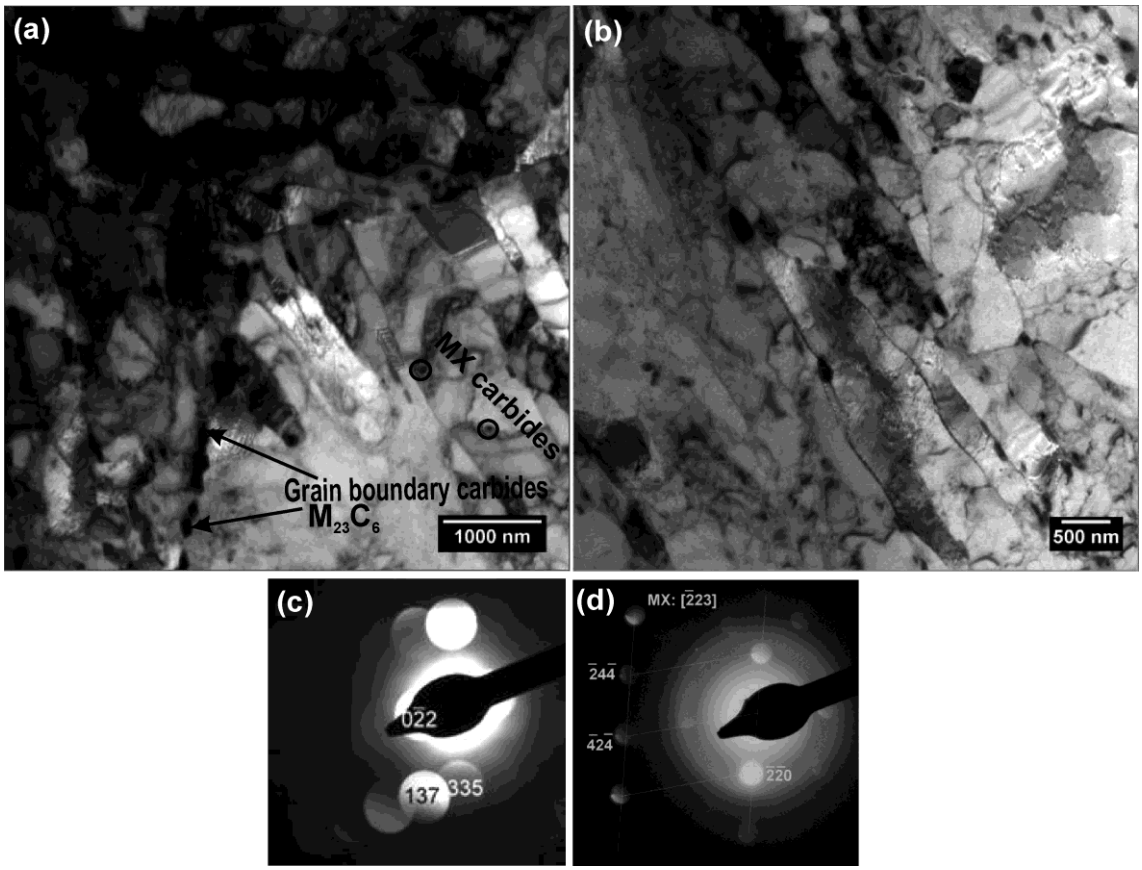

Figure 4.1.7 (a, b)Transmission electron micrograph of base metal showing precipitation of carbides in the intra- and inter-granular locations, and (c, d) diffraction patterns of $M_{23}C_6$ and MX type precipitates respectively shown in (a).

The size of $M_{23}C_6$ and MX precipitates were in the range of 60-130 nm and 20-40 nm respectively. The intergranular $M_{23}C_6$ provides resistance against grain boundary sliding whereas ultrafine MX precipitates act as barriers for dislocation movement during prolonged exposure at operating temperatures of the steel in service and also effectively improve the impact toughness [12]. The average grain size, martensite lath size and size of different precipitates were deduced from the analysis conducted on several samples.

4.1.4. Microstructure evolution in stir zone

Optical, SEM and TEM studies indicated that the microstructure in the SZ of FSW welds is very complex. The comparative evaluation of top and centre locations of SZ indicated more or less similar microstructure (Figure 4.1.8). Therefore, it is inferred that there are no temperature gradients across the thickness of 6 mm plate. SEM images of SZ centre for 200, 300,500 and 700 rotational speeds are shown in Figure 4.1.9. At all rotational speeds, the SZs revealed grain boundaries free from $M_{23}C_6$ precipitates. Indeed, in 200 rpm condition too, the grain boundaries containing the carbides have decreased alarmingly. The microstructures in the SZs can be understood on the basis of the interface temperatures attained by different rotational speeds. The interface temperature in 700 rpm condition was above A_{C3}. At these high temperatures the carbides which impede the austenite grain growth dissolve during FSW and hence relatively coarse grained austenite would develop. On subsequent cooling, the transformation to martensite occurs in coarse grain austenite, resulting in the microstructure as shown in Figure 4.1.9 (d). When the interface temperature attained is in the range between A_{c3} and A_{c1}, only partial transformation to austenite can occur during FSW. Consequently, on cooling after FSW, martensite would form in the austenite grains surrounding untransformed regions of α-ferrite. This type of structure is

typical and can be designated as the intercritical zone FSW structure that pertains to 300 and 500 rpm conditions. It was reported that the dissolution of highly cohesive alloy carbides such as $M_{23}C_6$, in highly alloyed ferritic steels, is very sluggish as it involves the transport of substitutional atoms over a large distances.

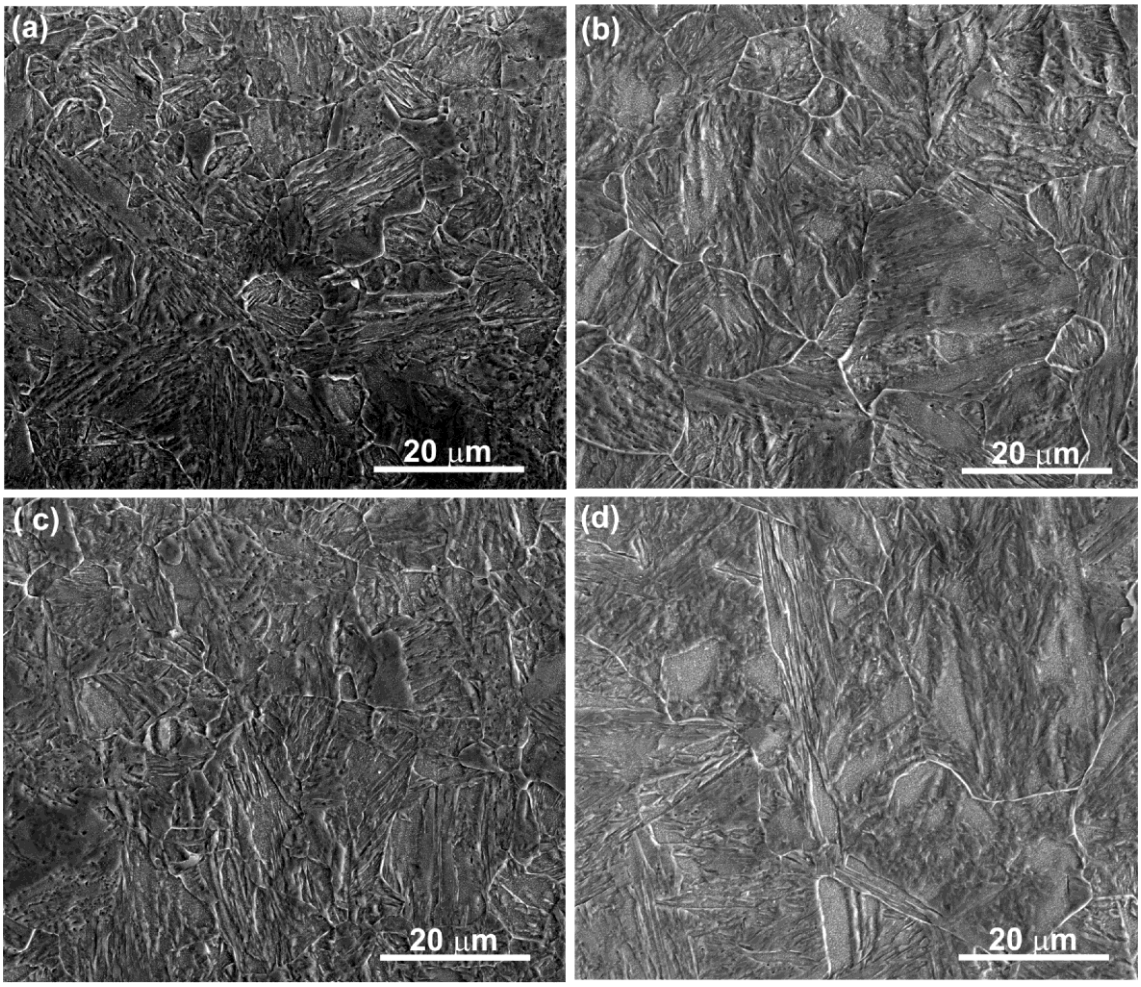

Figure 4.1.8 Scanning electron micrographss of SZs obtained on transverse sections. Surface near regions (a) 200 rpm, (b) 700 rpm and central portions of stir zone (c) 200 rpm and (d) 700 rpm.

The dissolution of carbide is being diffusion controlled process, it continues even after A_{C3} point is reached [13]. Therefore, it must be understood that all the ferrite grains would not transform to coarse austenite grains at rotational speeds greater than 300 rpm. At low rotational speed (200 rpm), since the peak temperature attained is much lower than A_{c1}, the sequential phase changes described above were absent. The interface

temperature in the 200 rpm condition is also much less than the tempering temperature (1033K) adopted for the parent metal but higher than that of approximate recrystallization temperature (Table 4.1.1), which is not too high to cause either rapid coarsening of precipitates or grain growth.

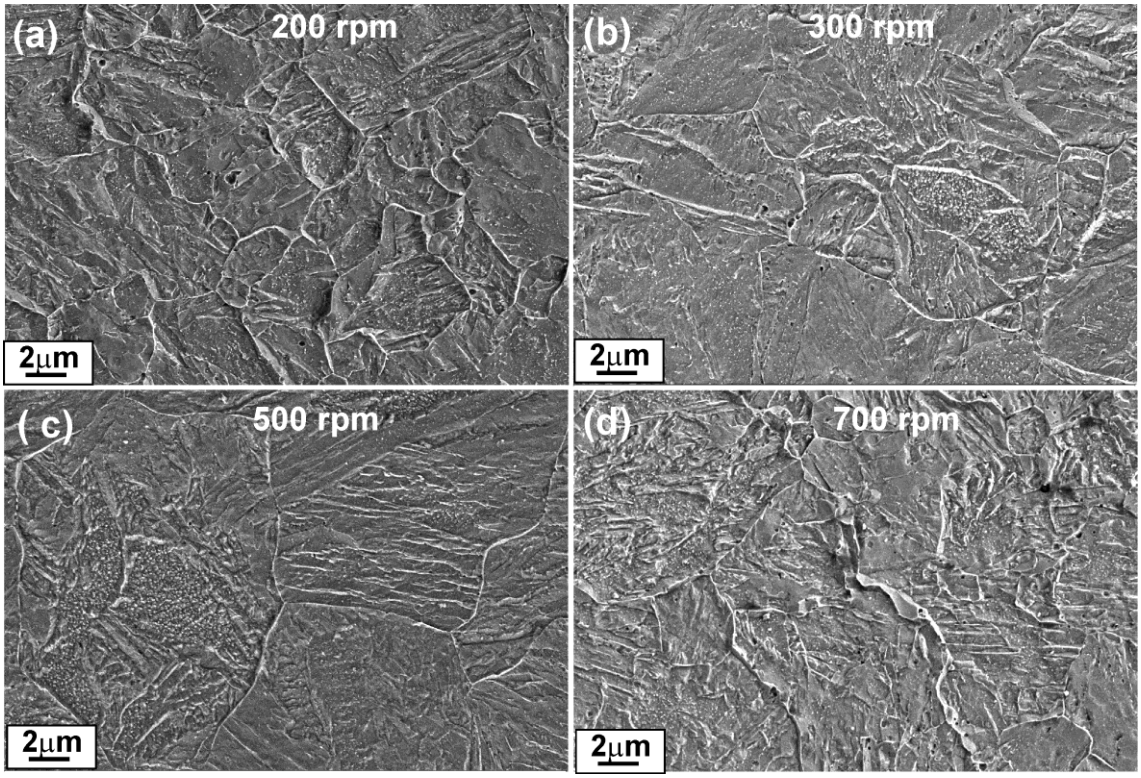

Figure 4.1.9. Field-emission scanning electron micrographs in the central portion of the SZs revealing precipitate-free grain boundaries and very fine precipitates in the intra-lath regions at 200, 300, 500 and 700 rpm.

Figure 4.1.10 illustrates the EBSD grain orientation maps. Corresponding EBSD image quality figures delineating high angle grain boundaries (HAGBs) and low angle grain boundaries (LAGBs) for the conditions mentioned in Figure 4.1.10 are shown in Figure 4.1.11. In Figure 4.1.11 HAGBs (defined by misorientation angle θ min $\geq$ 15 deg.) are represented by blue colour while red colour lines indicate LAGBs (defined by 2 deg. $\leq \theta$ min $\leq$ 15 deg.). The grains are clearly discerned in the EBSD crystal orientation image maps in Fig.4.1.10. No evidence for preferred orientation was observed. There was no obvious change in the microstructure of BM which was

remote from the centre of the weld. There has been substantial increase in the number of LAGBs in SZs compared to BM (Figure 4.1.11 (a)).These observations suggest that the dislocations introduced due to plastic deformation were re-organized into a low energy configuration such as cells and sub-grains, indicating the occurrence of dynamic recovery, and resulting in increased density of LAGBs. The simultaneous increase in the number density of HAGBs seems to have resulted from the progressive transformation of some of the low angle sub-grain boundaries. It is suggested that the sub-grains grow and rotate as they accommodate more dislocations into their boundaries, forming equiaxed recrystallized grains with high angle grain boundaries.Figure 4.1.12 depicts the grain size distribution and variation that occurred in BM and SZs. The grain size distribution in the SZ of 200 rpm resembles to that in the BM, while at higher rotational speeds it is very broad, with the presence of both fine and coarse grains. The average grain size in SZs increased with the increase in rotational speed. The average grain size in SZs of 200 rpm, 300 and 500 rpm, 700 rpm were 6, 11 and 12 μm respectively. Very fine recrystallized grains were seen at the boundaries of coarse grains at higher rotational speeds.

Detailed microstructure analysis was carried out using analytical TEM to investigate the phase transformation, dislocation substructure and carbide precipitation aspects. The salient features obtained through TEM studies are shown in Figure 4.1.3, for 200 rpm (Figure 4.1.13(a, b, c), 300 rpm (Figure 4.1.13 (d, e, f)) and 700 rpm (Figure 4.1.13(g, h, i)) conditions.

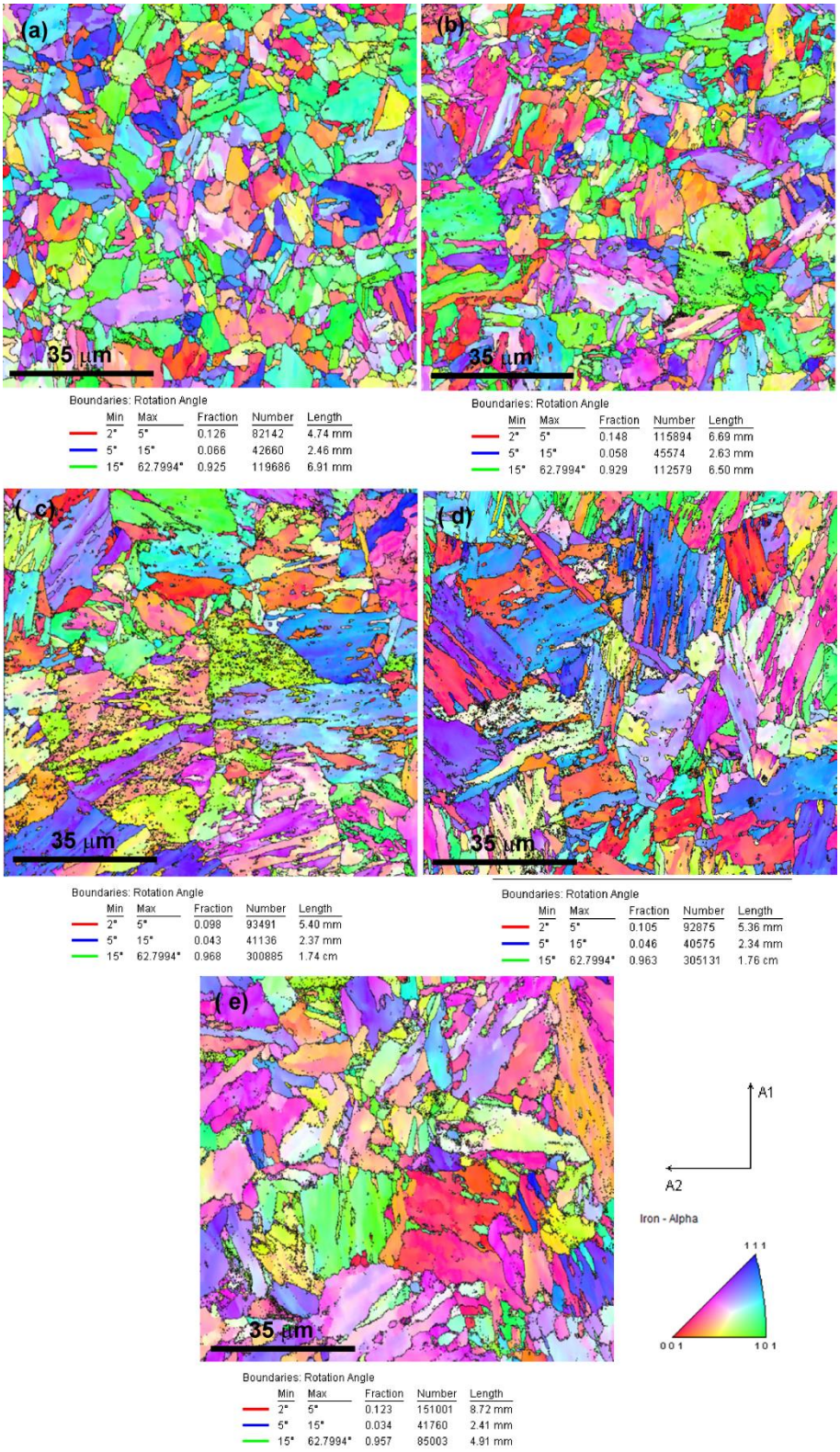

Figure 4.1.10 Grain boundary orientation maps of base metal and stir zones. (a) Base metal, (b) 200 rpm, (c) 300 rpm, (d) 500 rpm, and (c) 700 rpm.

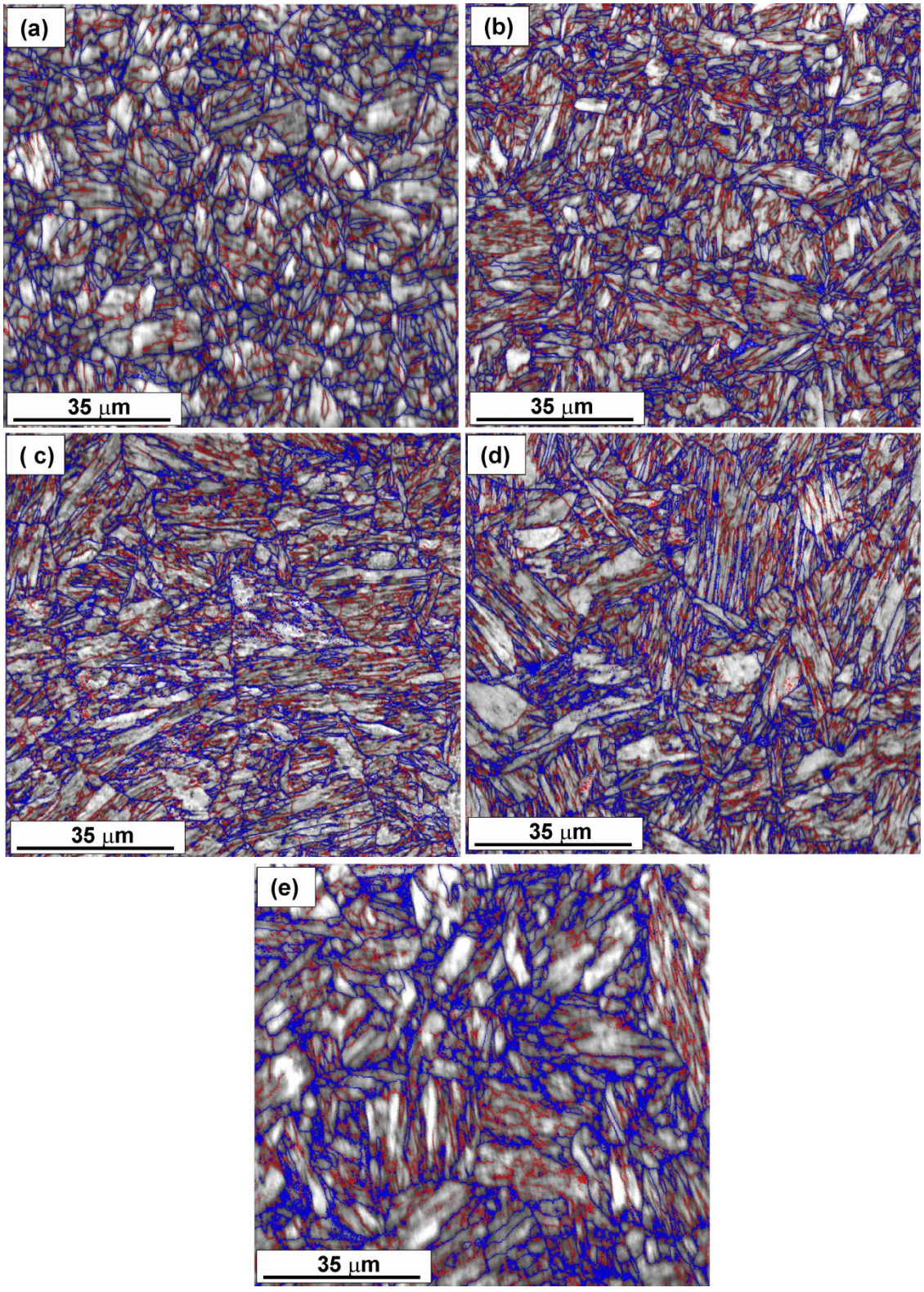

Figure 4.1.11 EBSD image quality maps of BM and SZs ,illustrates low and high angle boundaries depicted as red and thick blue lines respectively.(a) BM, (b) 200 rpm, (c) 300 rpm (d) 500 rpm and (e) 700 rpm.

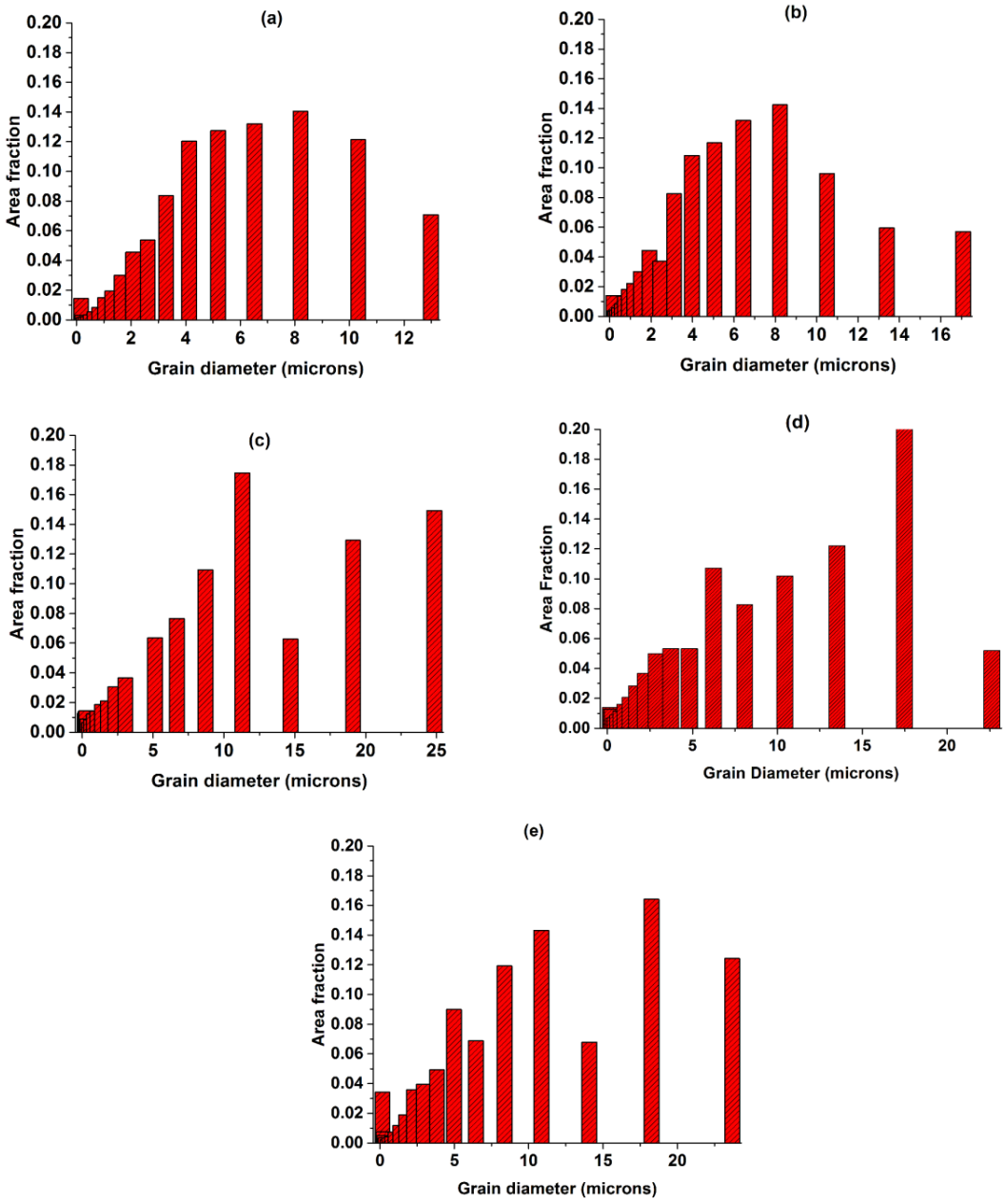

Figure 4.1.12 .Grain size distribution of base metal and centre of stir zones (a) BM (b) 200 rpm (c) 300 rpm (d) 500 rpm and (e) 700 rpm.

The important points that emerge from these investigations are:

The dislocations introduced due to plastic deformation during FSW at all rotational speeds were re-organised into a lower energy configuration such as elongated cells with randomly distributed dislocations in cell interiors, indicating the occurrence of dynamic recovery (Fig.4.1.13 (a, d, g))

- The dislocation density in cell interiors decreased with increasing rotational speed and the walls of elongated cells were made up of disordered arrays of dislocations. The elongated cells were formed in 'α' grains and the cell size was in the range 120-350 nm.

- Very fine needle type precipitates were formed at all rotational speeds (Figure 4.1.13(b, e, h)) in 'α' grains of about 1-2 µm; the selected area diffraction patterns from these precipitates indeed confirm that these correspond to the stoichiometry of Fe_3C and forms along [2 $\bar{1}$ 2] zone axis at 200 rpm, [$\bar{4}$ $\bar{5}$ 3] zone axis at 300 rpm, and [1 $\bar{2}$ 6] zone axis at 700 rpm (Figure 4.1.13 (c, f, i)). The presence of a high density of fine acicular Fe_3C precipitates of about 8-12 nm width and 50-100 nm length were also observed in some large 'α'grains of about 1-1.5 µm. The formation of M_3C within α grains could have occurred during cooling below A_{c1}.

- Fine martensite plates of 10-60 nm (arrow marked in Figure 4.1.13 (d and e)) were formed at the boundaries of recrystallized 'α' grains. The presence of these martensite plates was more predominant in 700 rpm condition compared to 300 rpm condition. The nucleation of austenite occurs at 'α' grain boundaries during exposure in the intercritical temperature regime that lies between A_{c1} to A_{c3} and subsequently transformed to martensite in 300 and 500 rpm conditions.

- Figure 4.1.13(g) shows the presence of fine martensite plates of 10-50 nm width at the boundaries of α grain in the SZ of 700 rpm. In this case, nucleation of γ at the 'α' grain boundaries occurred during exposure at temperatures above A_{c3}, with subsequent transformation to martensite. RAFM steels are prone to hardening and embrittlement due to martensite formation in the stir zone.

- At 300, 500 and 700 rpm the microstructures were composed of freshly formed martensite plates, α-ferrite and M_3C needle-like particles. The major driving force for Fe_3C precipitation appears to be carbon supersaturation; an increase in the carbon content should favour this type of carbides.

- TEM studies revealed the presence of relatively coarse primary undissolved TaC precipitates and very few fine MX precipitates in the matrix of SZ pertaining to 200 rpm (Figure 4.1.14). These precipitates have been found in close proximity to the precipitate-free grain boundaries. It is believed that these could be those MX type precipitates, formed in ferrite matrix during the tempering treatment of parent material and escaped dissolution. These fine precipitates however acted as anchoring sites for dislocations in the intragranular regions (Figure 4.1.14) and appear to have a delaying effect on recovery process.

From TEM investigations of SZs it was observed that Fe_3C precipitates within wider ferrite laths at all rotational speeds, which can be seen more evidently in Figure 4.1.13. The occurrence of Fe_3C in FSW welds of RAFM steels has not been reported so far. Detailed investigations were performed to ascertain the heat treatment conditions responsible for the formation of Fe_3C in Mod.9Cr-1Mo [14], and INRAFM steels with W varying between 1 to 2% [13]. It was reported that the occurrence of Fe_3C in these alloys is preceded by reformation of austenite. Subsequent air cooling from austenite phase field (normalizing treatment) was shown to be a pre-requisite for the nucleation of Fe_3C, while the high cooling rates that prevailed during water quenching suppressed the generation of Fe_3C. Based on the results of TEM and DSC analysis, it was concluded that the Fe_3C formation in

1.4%W steel occurs prior to the γ-α' transition under normalising conditions, reducing the carbon concentration in austenite with concomitant decrease in the driving force for martensitic transformation.

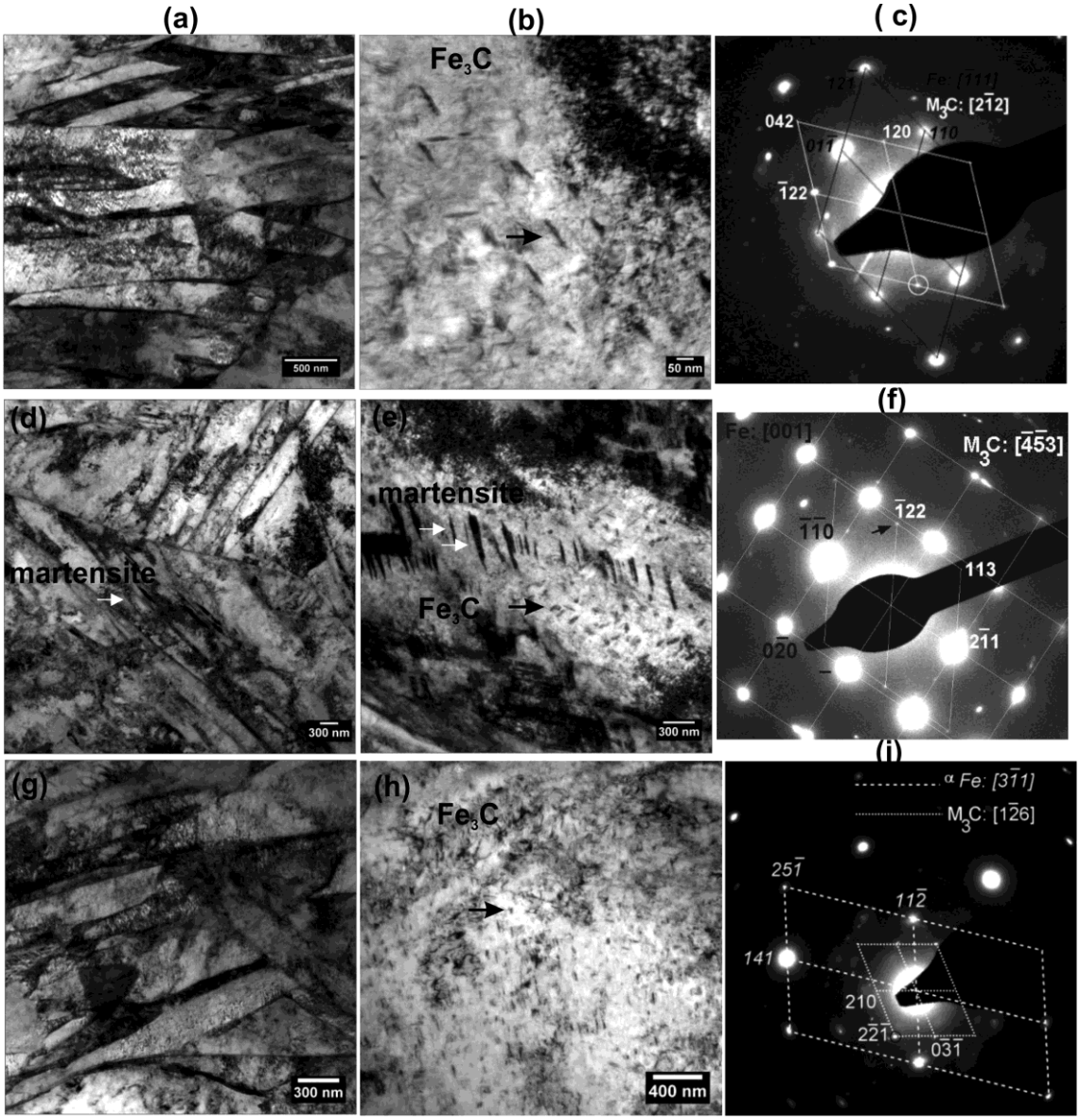

Figure 4.1.13 Transmission electron micrographs of stir zones 200 rpm (a, b, c), 300 rpm (d ,e ,f) and 700 rpm (g,h,i). Figure shows substructure, freshly formed martensite, Fe_3C and corresponding SAD patterns for Fe_3C

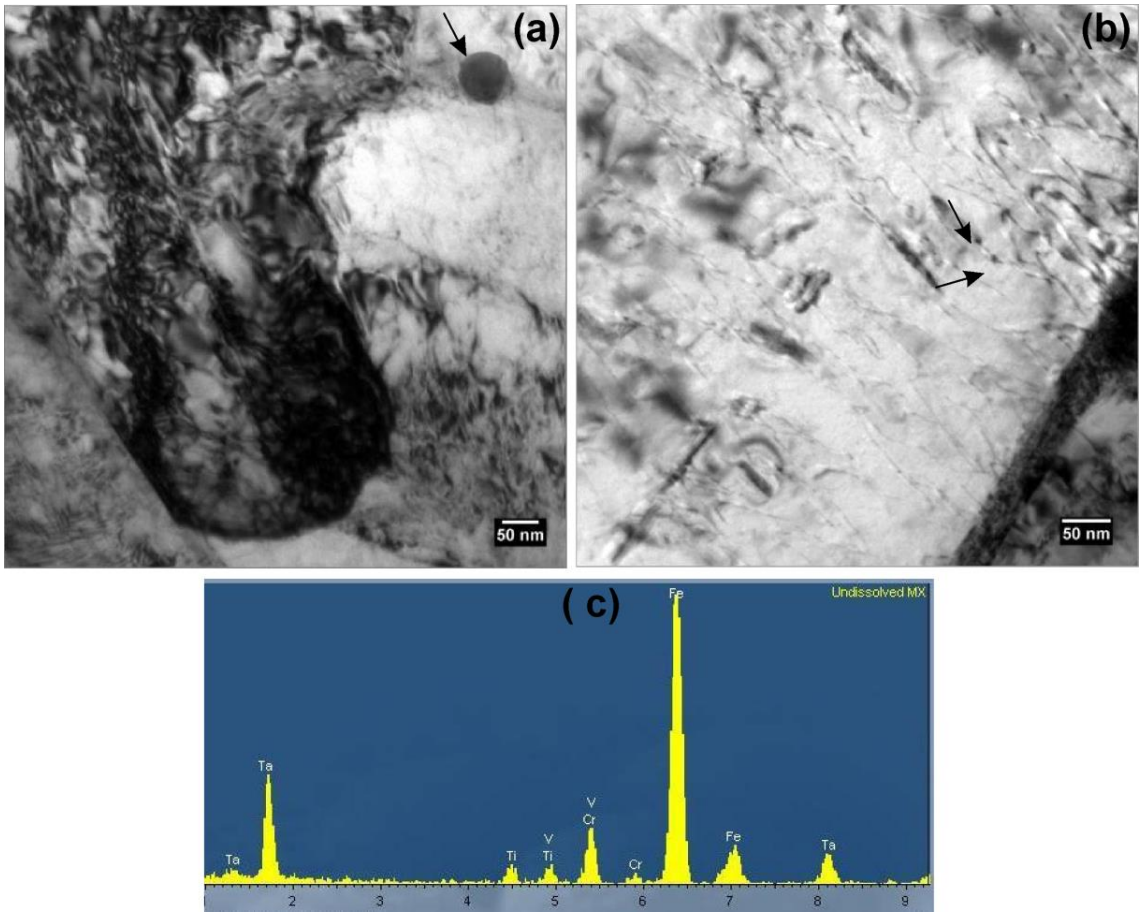

Figure 4.1.14 (a) Undissolved primary MX type precipitates in SZ of 200 rpm. (b) EDX spectra on undissolved MX precipitate showing Ta and V. (c) Dislocations pinned by very fine precipitates of MX at 200 rpm.

Though the rotational speeds greater than 300 rpm have seen the peak temperatures above $A_{c1,}$ the peak temperature obtained during FSW in 200 rpm condition was much lower than A_{c1}. Hence no transformation from α-γ and associated precipitation of Fe_3C during cooling in air is to be expected. Surprisingly Fe_3C could be precipitated even at lower temperatures, implying that the transformation to γ is not an absolutely necessary requisite. It appears that plastic deformation occurring during FSW generates large number of dislocations and non-equilibrium vacancies and perhaps the later would cause the accelerated diffusion of solute atoms promoting Fe_3C formation. Some of the $M_{23}C_6$ precipitates during FSW deformation appear to

have been fragmented making them to be subcritical and further leading to solid state dissolution, thereby resulting in a matrix supersaturated with carbon. The effects of tool rotational speed (200 and 700 rpm) on evolving microstructure in thermo-mechanically affected zone (TMAZ) and heat affected zone (HAZ) have been explored in the subsequent section.

4.1.5. Microstructure evolution in TMAZ and HAZ

Figure 4.1.15 (a, b) shows recrystallized grains with carbide precipitates in intra-granular regions in TMAZ for 200 and 700 rpm respectively. The grain boundaries are found free from carbide precipitates. In general, it appears that the microstructural changes in TMAZ are driven by the combined influence of heat generated and deformation induced by the tool. The dissolution of grain boundary $M_{23}C_6$ precipitates occurred both in SZ and TMAZ. The degree of dissolution and number of grain boundaries affected are severe in SZs of 200 and 700 rpm (Figures 4.1.9 (a) and 4.1.9 (d)). The TMAZ for 700 rpm appears to be in the intercritical temperature (between A_{c3} and A_{c1}) range where only partial transformation to austenite can occur during heating in the weld thermal cycle. Consequently, the microstructure resulting after cooling would be a mixture of austenite transformed product (martensite) and untransformed ferrite, which has been merely tempered during the weld thermal cycle. Unlike in SZ, the TMAZ showed considerable number of relatively coarse $M_{23}C_6$ and fine MC precipitates in the intragranular regions at 700 rpm (Figure 4.1.15(b)) albeit these precipitates are less in number in relation to BM structure. The non-dissolution of these carbides in TMAZ and high fraction of finer grains act as pointers to the peak temperature attained in this zone. The peak temperature did not cross A_{c3} and appears to be in the intercritical zone. A critical examination of TMAZ microstructures revealed higher density of intragranular carbides at 700 rpm most probably due to very fine scale

precipitation on large number of dislocations and sub-grain boundaries developed during FSW. The TMAZ in the 200 rpm condition (Figure 4.1.15 (a)) has undergone partial recovery and recrystallization as the temperature and plastic deformation experienced was much lower than those at 700 rpm. The majority of grain boundaries were free from carbides and few undissolved carbides were present in the matrix. It appears that dynamic recovery and recrystallization facilitated the preferential occurrence of sub-grains in the vicinity of grain boundaries. It is probable that the recrystallized sub-grains in the grain boundary regions grow and migrate by absorbing the high density of dislocations present and sweeping out few undissolved MX type carbides into the matrix (Figure 4.1.15 (a, b)).

The microstructure in HAZ as shown in Figure 4.1.15 (c, d) was different than those prevailed in SZ and TMAZ. Carbides persisted on grain boundaries but found coarsened, coalesced and agglomerated. At 700 rpm the precipitate coarsening and agglomeration took place in those grains that have not been transformed to austenite. The SZ in 200 rpm condition experienced a peak temperature of 773K (500^{o}C). Therefore, it is to be expected that the temperature in HAZ would be much less than 773K (500^{o}C).The temperature attained in HAZ at 200 rpm is not conducive to cause rapid coarsening of precipitates.

4.1.6. Microhardness

Vickers hardness profiles on transverse cross section of welds in the mid thickness zone for the four rotational speeds are given in Figure 4.1.16. Stir zones exhibited very high hardness irrespective of the rotational speed. This observation is in qualitative agreement with the results obtained on Eurofer-97 [15]. A rapid fall in the hardness in TMAZ was

observed as the distance from the stir zone increased and finally attained a dip in a very narrow zone between TMAZ and unaffected BM (Fig.4.1.16). This very small transition zone could pertain to HAZ. Hardness of the BM is about 250 HV. Very high hardness in the SZ and dip in hardness in HAZ was more pronounced in case of 500 rpm. As discussed above, microstructure in SZ changed with rotational speed and the individual constituents seem to exert profound effect in the domain of their operation.

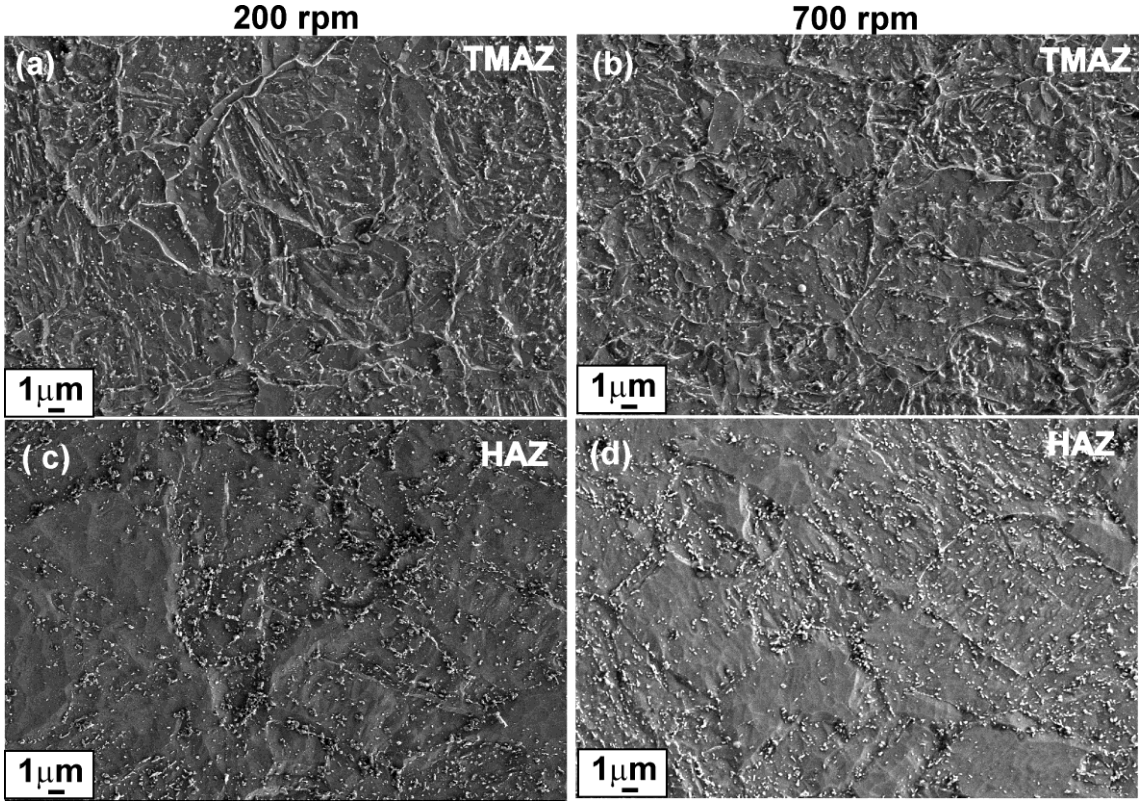

Figure 4.1.15 Scanning electron micrographs illustrating microstructures in (a) TMAZ and (c) HAZ at 200 rpm, (b) TMAZ and (d) HAZ at 700 rpm. TMAZs reveal recrystallized grains with carbide precipitates in intragranular regions with no precipitation on grain boundaries. HAZs show the coalescence of coarsened carbides.

There are several competing factors that dictate the hardness of SZ. Higher hardness in SZs of high rotational speeds could be associated with the strengthening effects of Fe_3C and martensite whereas at 200 rpm fine grain size, high dislocation density, the undissolved fine MX type of precipitates during FSW and Fe_3C contribute to higher hardness.

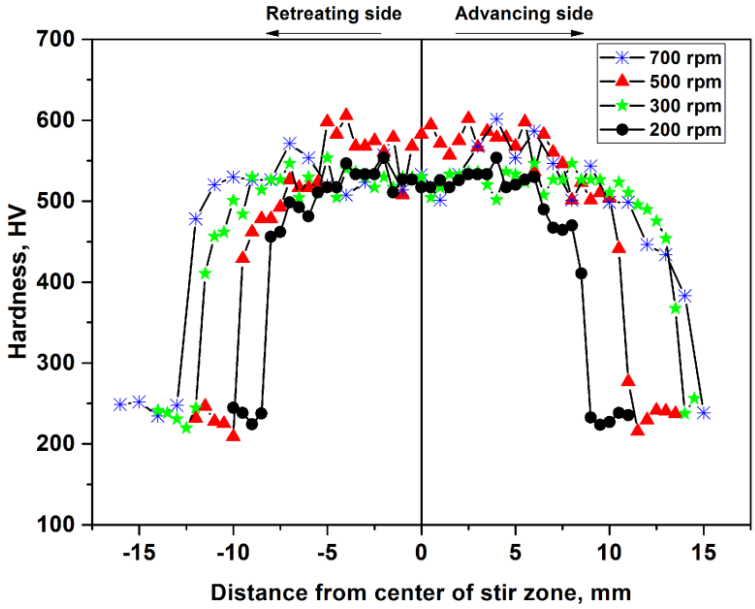

Figure 4.1.16 Microhardness profile of friction stir welded joint in the transverse section at mid-thickness.

4.1.7. Impact toughness

In the development of RAFM steels, one of the important properties considered was Charpy impact toughness. In this study, room temperature impact toughness of the BM and weld joints prepared by FSW (with 200 and 700 rpm) is evaluated employing sub-size (55×10×5mm) Charpy samples. The full-size Charpy specimen (55×10×10mm) values were deduced from the data on sub-size samples using a scaling factor of 3/2 [10, 11] and shown in Table 4.1.3. The results presented in Table 4.1.3 indicate high impact toughness for the FSW weld joint fabricated with 200 rpm (150 Joules), which is very close to the value obtained on parent material (159 Joules). The 700 rpm FSW welds exhibited poor toughness i.e., as low as 13.5 Joules. The low toughness at high rotational speed may be attributed to the combined effects of coarse grain size and martensite formed in the SZ. Investigations on fracture surface of impact tested samples indicated ductile mode of fracture for 200 rpm condition whereas cleavage mode of fracture dominated at 700 rpm (Figure 4.1.17). The poor impact toughness achieved at 700 rpm highlights the deleterious effect induced by freshly formed

martensite in SZ. The high toughness at low rotational speed could be attributed to average fine grain size and to the similar grain size distribution like in base metal, and non-existence of austenite-martensite transformation. These observations are in conformity with similar trends reported in steels [16]. Fine grain size helps to minimize stresses arising out of dislocation pile-ups and improves the resistance to cleavage fracture.

Table 4.1.3 Details of Charpy V-notch impact toughness values in as-welded condition. The sub-size Charpy impact values obtained in this study were converted to full size data given in the below table by using a scaling factor of 3/2 following the ref.10

Material condition	Impact energy, J
Base metal	159
200 rpm	150
700 rpm	14

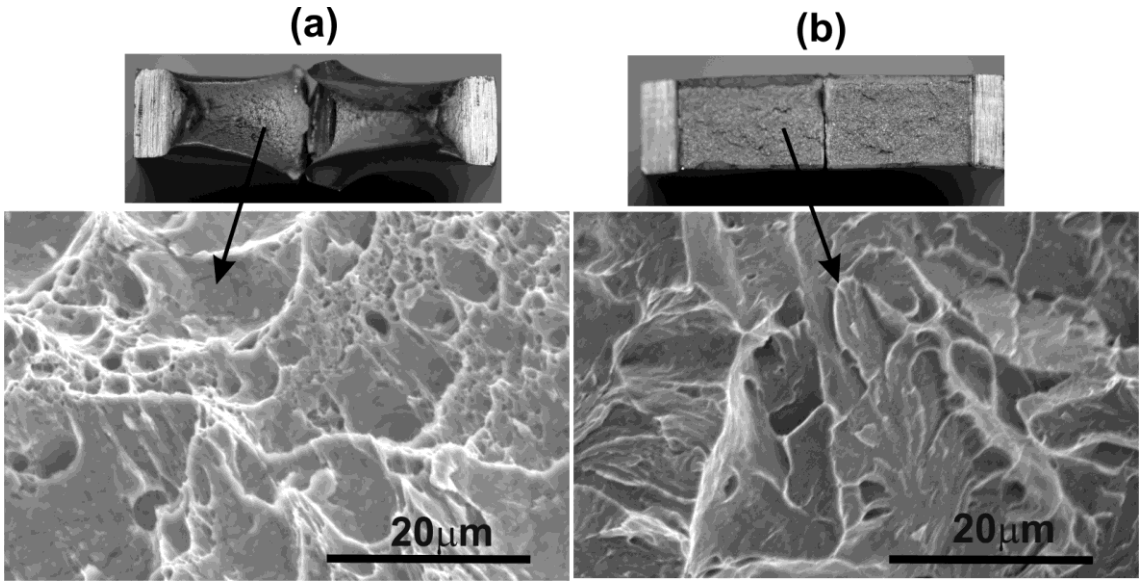

Figure 4.1.17 Scanning electron micrographs of the fracture surface of impact tested samples. (a) Ductile mode of fracture in stir zone at 200 rpm. (b) Cleavage mode of fracture at 700 rpm. Figure also shows macroscopic images of fracture surfaces of two halves arranged together after fracture.

4.2. Influence of tool rotational speed and PWHTs on microstructure and mechanical properties

4.2.1. Introduction

The SZ of RAFM steel friction stir weld joint revealed carbide-free lath and grain boundaries and precipitation of Fe_3C in the form of needles irrespective of the rotational speeds employed [7,8,17]. It must be remembered that RAFM steels were designed to have adequate creep resistance. Lack of precipitates on grain boundaries can be considered as a serious concern. The absence of grain boundary carbides are known to promote grain boundary sliding and associated intergranular cavities and cracks leading to intergranular fracture. These damages features are very harmful for creep and creep-fatigue interaction resistance at elevated temperatures. Consequently, PWHTs are necessary even in FSW process to lower the hardness to the level of base metal, re-precipitate the grain boundary $M_{23}C_6$ precipitates and achieve the transformation of Fe_3C to suitable phases for improving the room temperature and elevated temperature mechanical properties. Therefore the present study has been carried out with the intention of establishing suitable PWHT for restoring the mechanical properties of FSW joints to the level of BM, and developing a comprehensive understanding of evolving microstructure during the PWHTs across various zones of the weld joint. The details of PWHTs are given in section [3.5].The correlations between evolving microstructure and hardness in various zones of FSW joints as a function of rotational speed, and the dependence of impact strength on rotational speed and PWHTs are presented and discussed in subsequent sections. The low and high rotational speed FSW welds at 200 and 700 rpm were subjected to two types of PWHTs, namely PWDT and PWNT to study their influence on microstructure and mechanical properties.

4.2.2. Microstructure evolution after PWDT

The SEM micrographs of SZ, TMAZ and HAZ after PWDT for both 200 and 700 rpm conditions are shown in Figure 4.2.1.TEM microstructures of SZs, their SAD pattern and EDX spectra are illustrated in Figures (4.2.2 and 4.2.3). PWDT caused the re-appearance of $M_{23}C_6$ on grain boundaries in SZ and TMAZ.

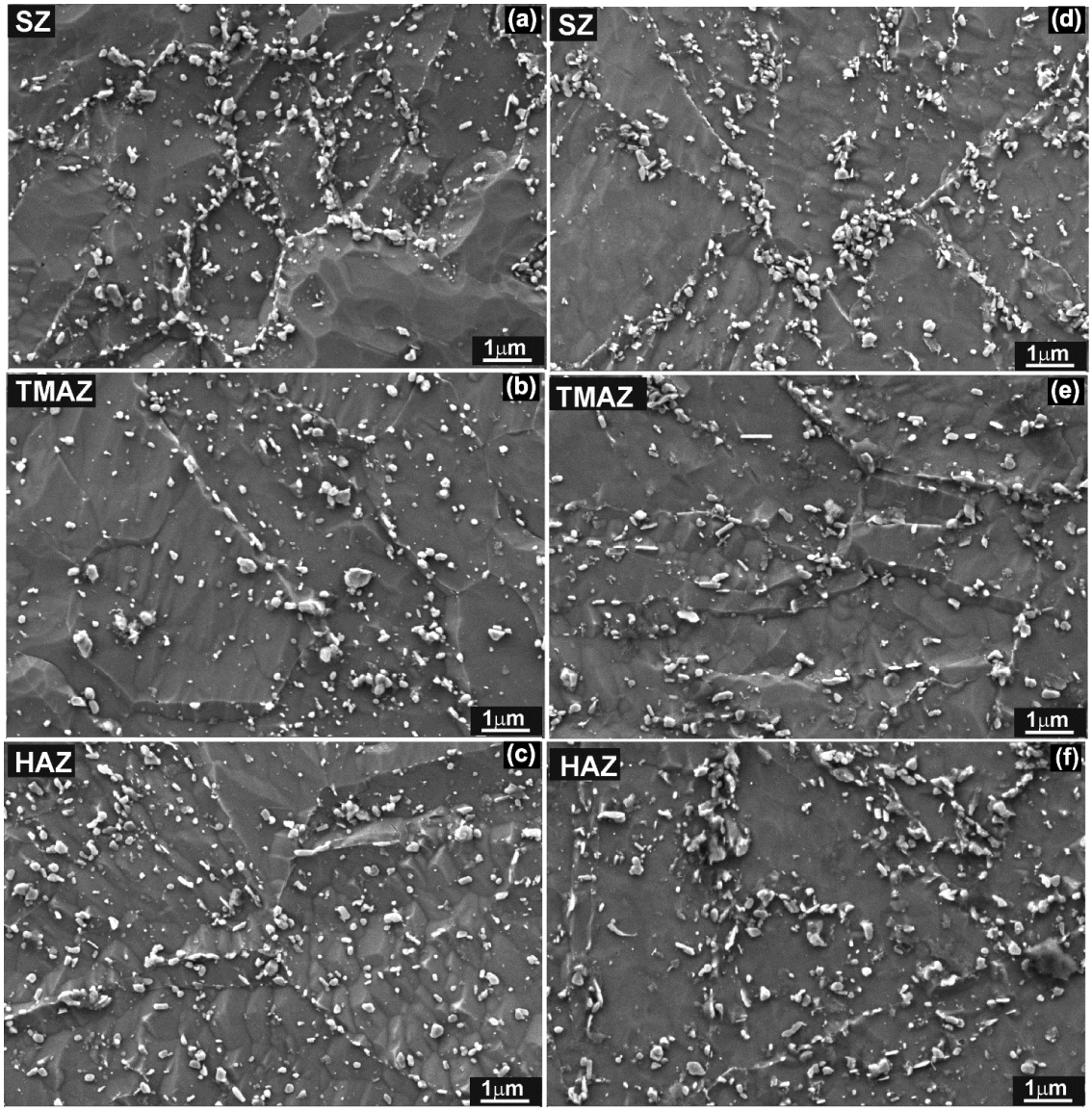

Figure 4.2.1 High magnification FE-SEM microstructures in PWDT condition illustrating precipitation behaviour of carbides in different zones for 200 rpm (a, b, c) and 700 rpm (d, e, f) conditions.

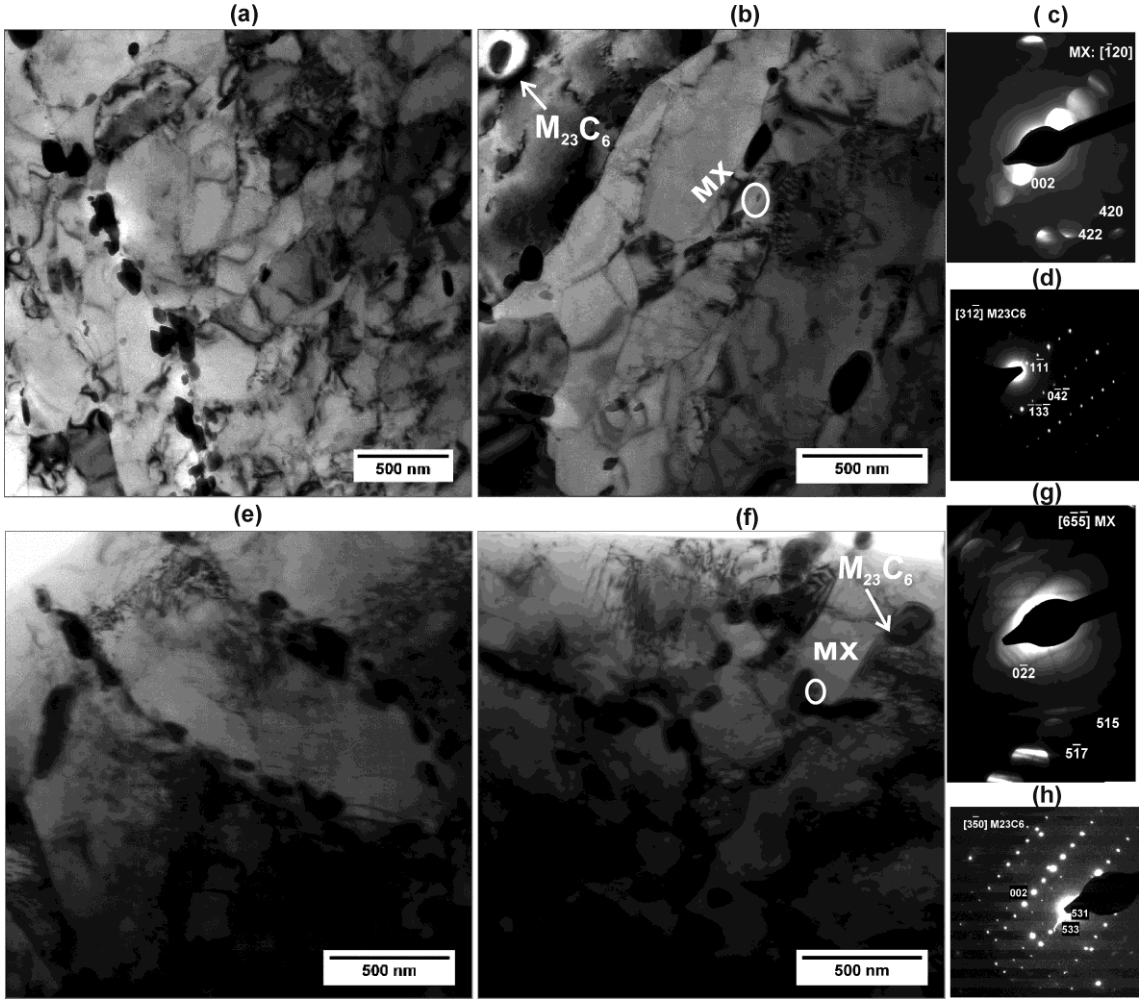

Figure 4.2.2 Transmission electron micrographs of stir zone centre after post weld direct tempering treatment for 200 rpm condition (a-d) and 700 rpm condition (e-h).

The precipitation of carbides was more heterogeneous in the intra-granular regions at high rotational speed; some grains displayed very coarse and clustered precipitates whereas few grains had regions that are free from precipitation (Figures 4.2.1(a) and 4.2.1 (d)). The precipitate ripening was more intense in HAZ of 700 rpm (Figure 4.2.1(f)). All the three zones experienced a temperature of 1033 K (760^{o}C) (below A_{c1}) during PWDT. In general, the precipitation of intra-granular carbides in SZ, TMAZ and HAZ of 200 rpm was more or less homogeneous (Figure 4.2.1 (a-c)). Further investigations conducted by TEM revealed the type, composition and size of various precipitates in the SZs. The SZ microstructure at 200 rpm as shown in Figures 4.2.2 (a)

and (b) clearly revealed recovery, indicated by the occurrence of sub grains with low dislocation density. Analysis of the diffraction patterns shown in Figures 4.2.2(c) and (d) confirmed the presence of $M_{23}C_6$ and MC along (3 1 $\bar{2}$) and ($\bar{1}$ 2 0) axes respectively. The MX carbides were found to be rich in V or Ta.

It was found that $M_{23}C_6$ prevalently occur along the sub-grain and grain boundaries while MX precipitates formed within sub-grains (Figures 4.2.2 (a) and (b)). The grain boundary $M_{23}C_6$ precipitation was discrete while very fine MX precipitated in the intra lath regions along with the presence of coarse $M_{23}C_6$ on lath boundaries. The dislocation density was low since no fresh martensite has formed during FSW at 200 rpm. The size of $M_{23}C_6$ was in the range of 160 to 250 nm, suggesting very marginal coarsening of prior existing precipitates while that of V rich MX precipitates was less than 20 nm. The lath size showed a wide range varying from 250 to 900 nm. The recovery was faster in the case of 200 rpm weld as no fresh martensite occurred during FSW. The SZ microstructure at 700 rpm as shown in Figure 4.2.1(d) and Figure 4.2.2 (e, f) consisted of tempered martensite with intra lath precipitation. The lath width was found to be in the range of 280-600 nm, which is finer than that in the case of 200 rpm. However, qualitatively the dislocation density in the lath interiors was apparent to be higher due to martensitic transformation at 700 rpm. It was also observed that Cr rich $M_{23}C_6$ carbides prevalently occur along the sub-grain and grain boundaries, while Ta rich or V rich MX precipitates formed within the sub-grains. The size of $M_{23}C_6$ was in the range of 40 to 160 nm suggesting fine re-precipitation while that of MX was less than 20 nm. Figure 4.2.2 (g) and Figure 4.2.2 (h) show the diffraction patterns of $M_{23}C_6$ and MX precipitates indicated in Figure 4.2.2(f). Analysis of the energy dispersive X-ray spectra of $M_{23}C_6$ obtained for 200 and 700 rpm indicated the presence of 48-50 wt. % Cr and 10-12 wt. % W (Figures 4.2.3 (a) and 4.2.3 (b)). The composition of $M_{23}C_6$

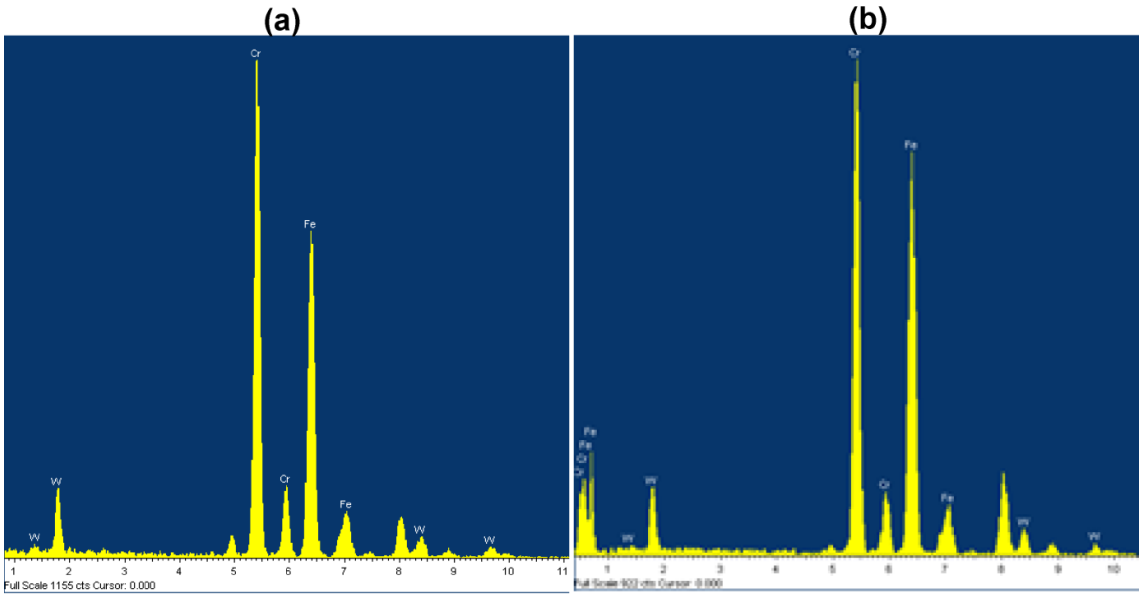

Figure 4.2.3 EDX spectra of $M_{23}C_6$ precipitate of 200 rpm (a) and 700 rpm (b) indicated in Figure (b, f).

was similar at both the rotational speeds. The presence of Fe- rich M_3C was not observed after PWDT, suggesting the metastable nature of these precipitates. This result is in agreement with those reported in literature [18, 19] for P91 and RAFM steel on the evolution of chromium-rich $M_{23}C_6$ precipitates and Ta or V rich MX precipitates during tempering at 1033K (760^{o}C). The transformation of Fe_3C into chromium carbide during tempering may result in two ways [20, 21].

(i) In-situ transformation where individual cementite particles appear to transform directly to groups of chromium carbide particles. The chromium carbide may nucleate at numerous points at the Fe_3C–ferrite interface and grow through diffusion until the less stable Fe_3C completely disappears. Coarse $M_{23}C_6$ precipitates observed in the matrix could be attributed to this mode of transformation.

(ii) Separate nucleation of chromium carbide where original Fe_3C dissolves in the ferrite matrix and chromium carbide nucleates independently at new sites, preferably on dislocations. These carbides are much finer than carbides precipitated by in-situ mechanism.

4.2.3. Microstructure evolution after PWNT

The A_{c1} and A_{c3} values for INRAFM steel are given in Table 4.1.1. In the SZ, the $M_{23}C_6$ precipitates were fragmented and appear to have undergone solid-state dissolution, leaving behind the grain boundaries which are devoid of these carbides. In SZ few MX type of precipitates were still present in the as-welded state. This observation suggests that considerable amount of super heating above A_{c3} is essential for the complete dissolution of MX precipitates, since the dissolution reactions of MX in γ-austenite will be decided by the diffusional mobility of substitutional solutes like W, Ta and V [20]. Detailed investigations were performed in order to obtain the optimum normalizing condition for RAFM steels [22]. The optimum normalizing treatment condition was arrived at based on the variation of prior austenite grain size and hardness with austenitizing heat treatment temperature [22]. The choice of the normalizing treatment at 1253K (980^{o}C) was made in order to realize the full dissolution of $M_{23}C_6$ type carbides in SZ if any, and to ensure the full austenite grains, which would promote the ease of formation of martensite upon subsequent air cooling. The normalizing treatment at 1253K (980^{o}C) resulted in fully martensitic structure. Employing low normalizing temperatures that would make $M_{23}C_6$ to dissolve and re-austenite fully are expected to yield high impact toughness**.** PWNT restored the microstructures of SZ, TMAZ and HAZ to the state existing in parent metal prior to FSW. Post-weld normalizing heat treatment led to the formation of martensite in fine grains at 200 rpm while martensite occurred in coarse grains at 700 rpm in the SZs (Figure 4.2.4).

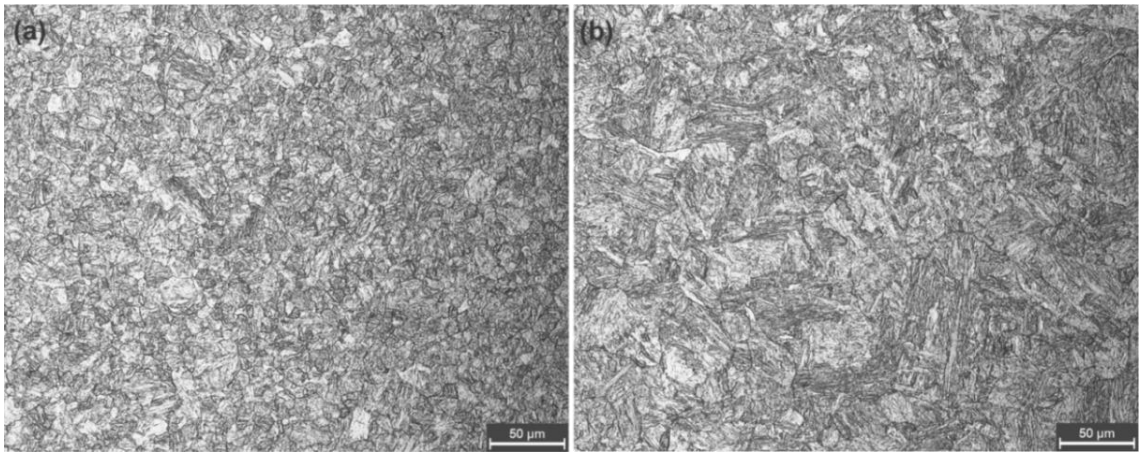

Figure 4.2.4 Optical images after post weld normalising heat treatment showing (a) martensite in fine grains at 200 rpm and (b) martensite in coarse grains at 700 rpm.

The normalizing (re-austenitizing) treatment dissolved most of the prior existing $M_{23}C_6$ precipitates. Subsequent tempering led to re-precipitation of $M_{23}C_6$ and MX at appropriate locations in optimum size and distribution in SZ (Figure 4.2.5). TEM microstructures obtained after PWNT in SZs of 200 rpm and 700 rpm (Figures 4.2.5 (a) and (b)) clearly illustrate the precipitation of $M_{23}C_6$ on grain boundaries and the presence of tempered martensite lath structure at both the rotational speeds. The size distribution plots of $M_{23}C_6$ precipitates in SZs at 200 and 700 rpm are shown in Figure 4.2.6. The size of $M_{23}C_6$ was in the range of 60-260 nm at 200 rpm, while it was in the range of 70-160 nm at 700 rpm, while MX precipitates was only <20nm in size. The lath width was in the range of 250-850 nm in the PWNT state. The SEM photographs presented in Figure 4.2.7 (a- f) illustrate the microstructures developed in various zones after PWNT for low and high heat input conditions. After PWNT treatment the SZ has shown a uniform distribution of precipitates in the intragranular regions and eliminated the heterogeneous microstructure developed in the as-welded state in TMAZ and HAZ. The coarse $M_{23}C_6$ precipitates which are considered to be responsible for HAZ

were dissolved during the normalizing treatment and re-precipitated as fine carbides during tempering thus eliminating HAZ softening in case of 700 rpm.

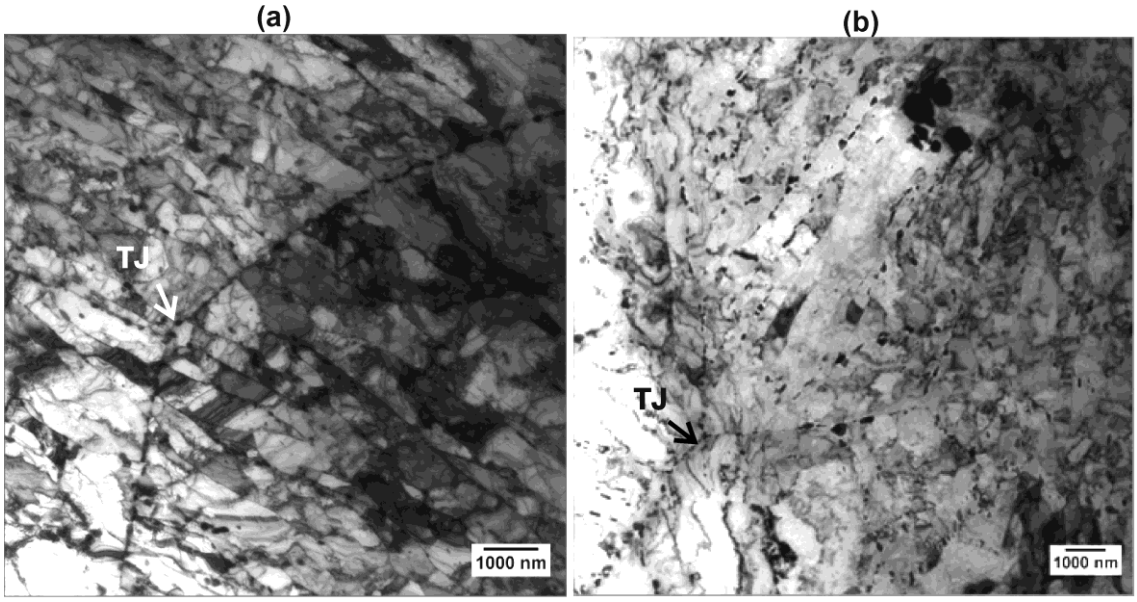

Figure 4.2.5 Transmission electron micrographs of stir zones after PWNT treatment, (a) 200 rpm and (b) 700 rpm. Figure shows re-precipitation of carbides on grain and lath boundaries.TJ–triple junction.

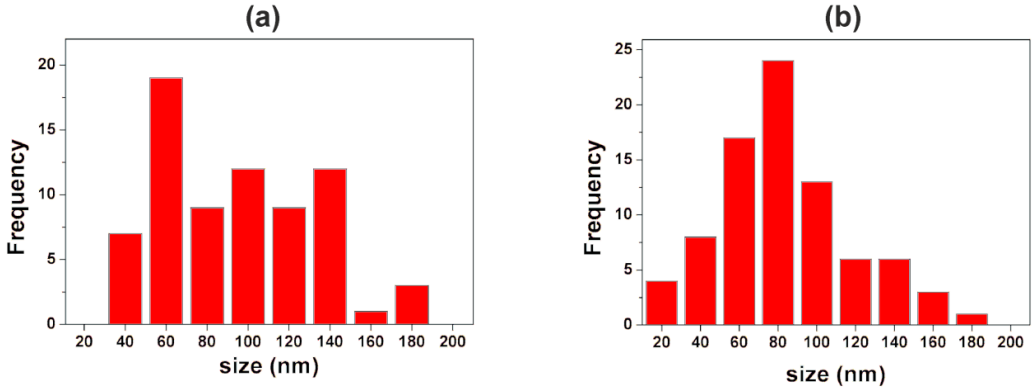

Figure 4.2.6 Size distribution of $M_{23}C_6$ precipitates in SZs of (a) 200 and (b) 700 rpm after post weld normalising plus tempering treatment.

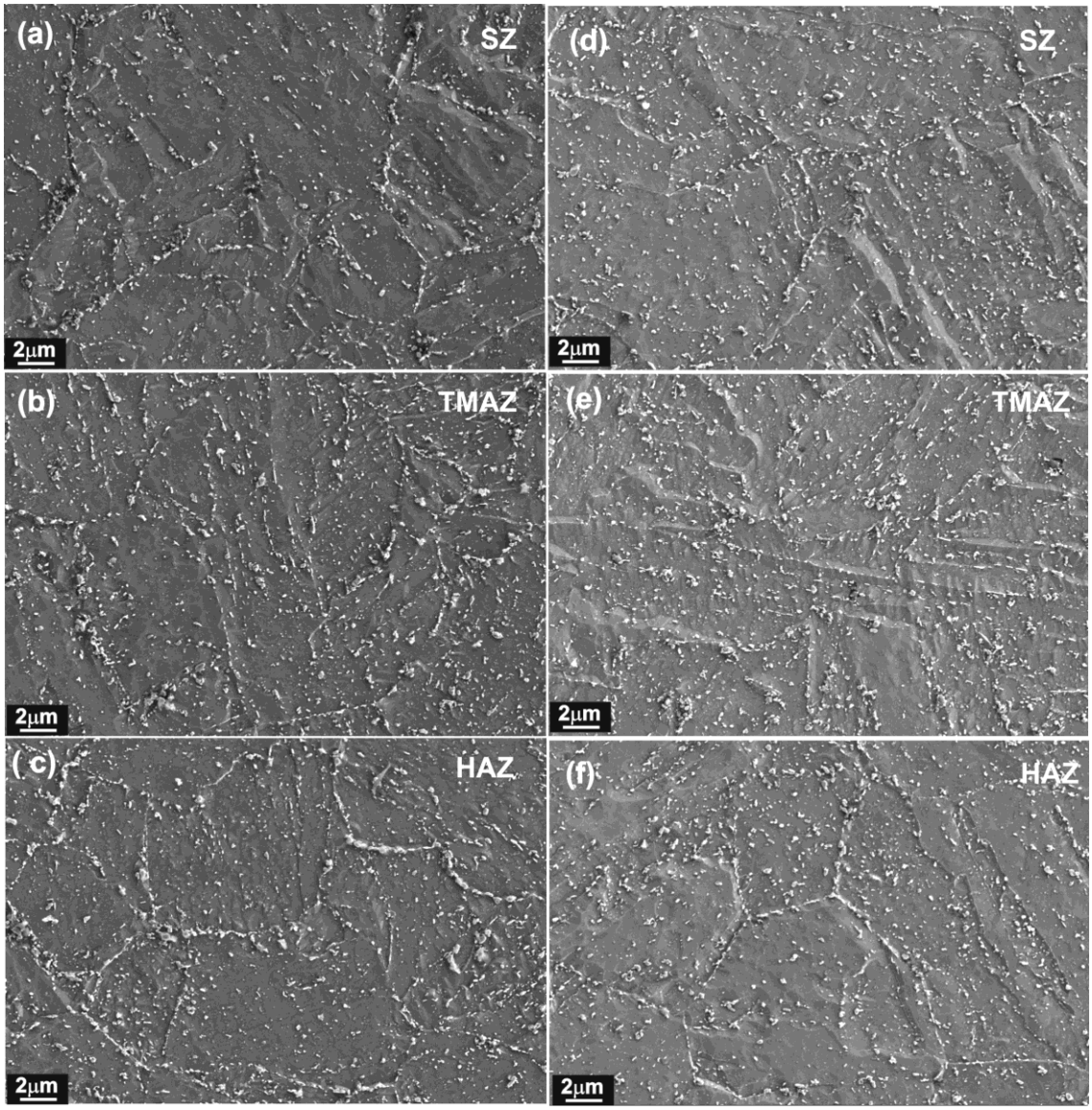

Figure 4.2.7 Scanning electron micrographs illustrating intra- and intergranular precipitation of carbides in various zones after PWNT treatment for 200 rpm (a, b, c) and 700 rpm (d, e, f) conditions.

4.2.4. Microhardness

Vickers microhardness profiles on transverse cross-section of welds in the mid-thickness region for the two rotational speeds at PWDT and PWNT conditions are shown in Figure 4.2.8. There has been substantial decrease in hardness in the SZs after PWDT (Figure 4.2.8 (b)) and the hardness trough in the HAZ was more pronounced in case of 700 rpm. Furthermore, the hardness was not uniform across the weld joints. In general, the

hardness of 700 rpm joint was lower than that of 200 rpm joint. The decrease in hardness after PWDT in SZ of 200 rpm condition could be attributed to dynamic recovery, increase in the width of prior existing laths, coarsening of intragranular carbides (Figures 4.2.2 (a) and 4.2.2 (b)) leading to depletion of carbide forming elements which lower the solid solution strengthening effects. The decrease in hardness for 700 rpm condition could be attributed to the annihilation of martensite induced dislocations, loss of solid solution strengthening elements from the matrix due to nucleation and growth of $M_{23}C_6$ and MX precipitates (Figures 4.2.2 (e) and 4.2.2 (f)). The microhardness profile suggested that PWDT could not bring down the level of hardness in SZs to the level exhibited by the BM. Dip in hardness in HAZ was more pronounced after PWDT in case of 700 rpm weld due to the agglomeration and coarsening of $M_{23}C_6$ type of carbides at grain and sub-grain boundaries (Figure 4.2.1(f)) and replacement of lath like martensite microstructure with high dislocation density by large sub-grains with low dislocation density. The PWNT treatment promoted more or less uniform hardness across 200 rpm weld joint (Figure 4.2.8(c)). The hardness was above 210 HV, which is considered to be an acceptable hardness value for achieving high creep resistance in ferritic-martensitic steels. However, the 700 rpm joint displayed very low hardness in the SZ. This could be attributed to coarse grain size, laths, sub-grain boundaries and carbides.

4.2.5. Impact toughness

Impact toughness of post weld heat treated joints was determined by employing 55×10×5mm Charpy V-notch sub-size samples. The full-size Charpy specimen (55×10×10mm) values were deduced from the data on sub-size samples using a scaling factor of 3/2[10,11]and reported in Table 4.2.1. In general, fine grain size and

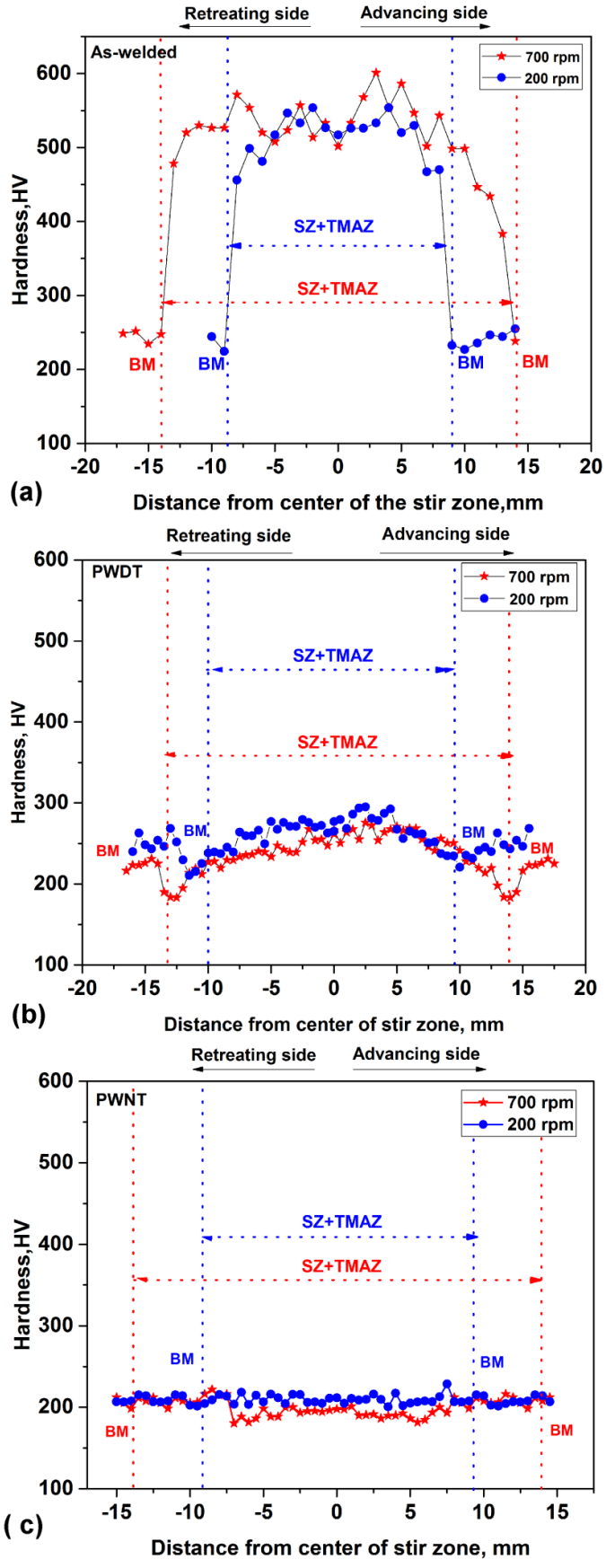

Figure 4.2.8 Hardness profiles of the friction stir welds across the stir zone for 200 and 700 rpm in (a) as-welded (b) PWDT and(c) PWNT conditions.

high fraction of low angle boundaries are beneficial for impact toughness [23].Fine grain size has been reported to provide greater resistance to cleavage cracks because of the large number of crack arrests that occur at grain boundaries. Low angle boundaries have been reported to have better atomic fitting on the grain boundary planes and this result in greater resistance to intergranular crack propagation [23]. The PWDT significantly improved the impact toughness for 700 rpm weld joints and exhibited toughness close to that of BM. The fracture surfaces of the impact tested samples as shown in Figure 4.2.9 in both PWDT and PWNT conditions exhibited ductile mode of fracture irrespective of the rotational speed. The improvement in toughness for 700 rpm weld joint could result from the tempering of martensite. The PWNT exhibited homogeneous distribution of precipitates (Figure 4.2.5) and hardness across the weld joint and the impact toughness was considerably improved compared to PWDT.

Table 4.2.1 Details of Charpy V-notch impact toughness values .The sub-size Charpy impact values obtained in this study were converted to full size data given in the below table by using a scaling factor of 3/2 following the ref[10,11] .

Material condition	Impact energy, J	Impact energy, J (PWDT)	Impact energy, J (PWNT)
Base metal	159	-	184
200 rpm	150	155	180
700 rpm	14	144	169

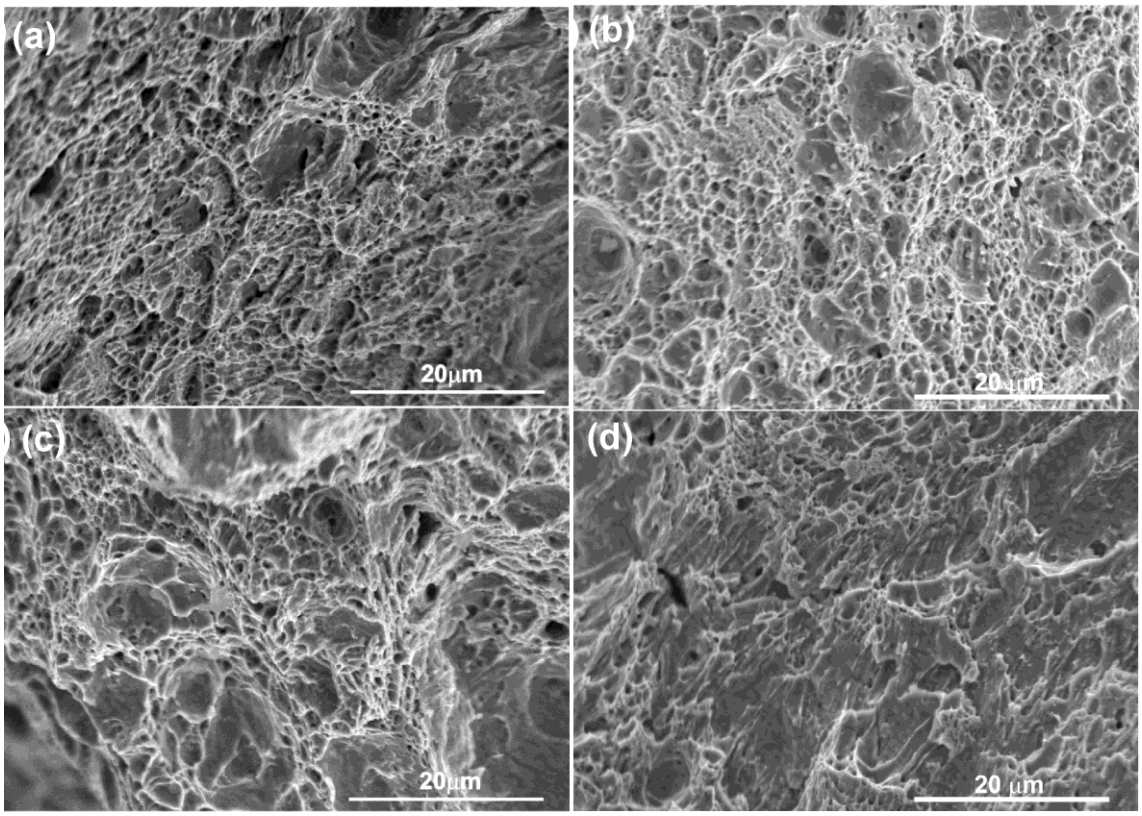

Figure 4.2.9 Scanning electron micrographs of the fracture surface of impact tested samples. Ductile fracture prevailed in case of 200 rpm in (a) PWDT (c) PWNT conditions and 700 rpm in (e) PWDT and (f) PWNT conditions.

4.3. Effect of section thickness on microstructure and mechanical properties in FSW of INRAFM steel

4.3.1. Introduction

Recent studies on FSW of RAFM steels (F82H, EUROFER and INRAFM) using PcBN and refractory tool materials have indicated that FSW could be successfully employed to join thin sections [5,7,8,17]. Although thin sections may find application, majority of the components in TBM will likely be thicker in design. FSW offers significant cost savings in joining thick sections because of its capability to join thicker sections in single pass unlike in traditional arc welding processes which require several passes to fill the weld joint. However, with the increased section thickness, FSW would generate high frictional forces and high heat input leading to severe thermal gradients across the weld joint. The effects of these on microstructure and mechanical properties are not yet explored. In this thesis, an attempt has been made to understand the metallurgical aspects pertaining to FSW of thick sections. The interesting results obtained on FSW of 12 mm thick INRAFM plate with respect to evolving microstructure and mechanical properties are discussed in the following sections. The effects of post weld heat treatment on resulting microstructure and associated mechanical properties are also addressed.

4.3.2. Microstructure evolution in as-welded condition

Full penetration defect-free bead-on-plate friction stir welds were successfully produced employing PcBN tool on 12 mm thick plates. The profile and dimensions of the PcBN tool used in this study is shown in Figure 3.4. FSW on 12 mm thick plate was accomplished at rotational speeds of 500 and 900 rpm. The process plot obtained on 12 mm plate, pertaining to the traverse position (X), tool position (Z), feed rate (mm/min),

spindle speed (rpm), spindle torque (N-m), Z-force (kN) and X-force (kN) as a function of time, in the FSW experiment conducted with 500 rpm is presented in Figure 4.3.1. The analysis of force and torque data revealed that the steady state welding condition is obtained beyond the first 50 mm of welding. The region of steady state condition was also marked by the good quality surface without excessive flash occurrence, and no defects as evidenced by visual examination and metallographic analysis. The samples for metallographic analysis, hardness and impact toughness evaluation were sectioned in the steady state welding region. The heat input increased with section thickness and rotational speed. The details of welding parameters are given in Table 3.3. The photograph of FSW joints for 500 and 900 rpm is shown in Figure 4.3.2.The excessive tool markings on the weld surface at high tool rotational speed (900 rpm) could be attributed to greater rate of heat generation and excessive softening of material.

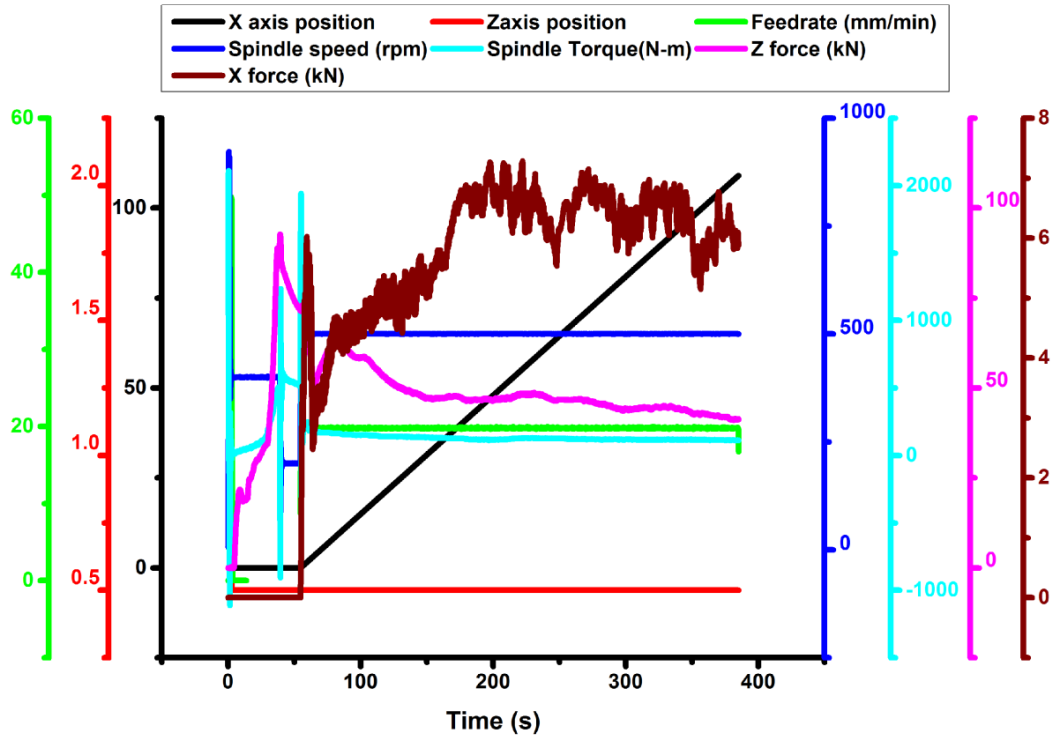

Figure 4.3.1 Process parameters recorded by the welding machine during FSW process (500rpm).

The transverse cross-section macrostructure of the FSW joints in both the rpm conditions showed through thickness full penetration welds with no indication of defects. Both the conditions displayed SZ (weld nugget), thermo-mechanically affected zone (TMAZ), heat affected zone (HAZ) and base metal (Figure 4.3.3).Higher rotational speed led to widening of TMAZ and weld nugget.

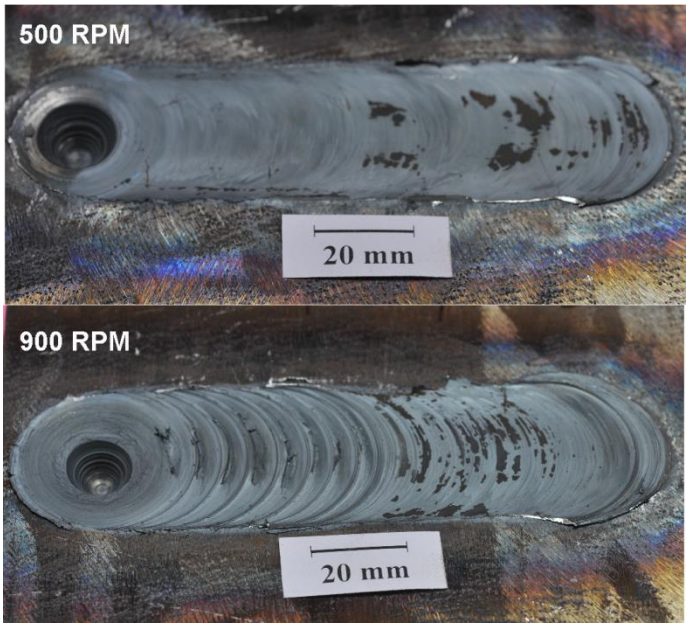

Figure 4.3.2 Macrograph of bead- on- plate friction stir weld at 500 and 900 rpm condition.

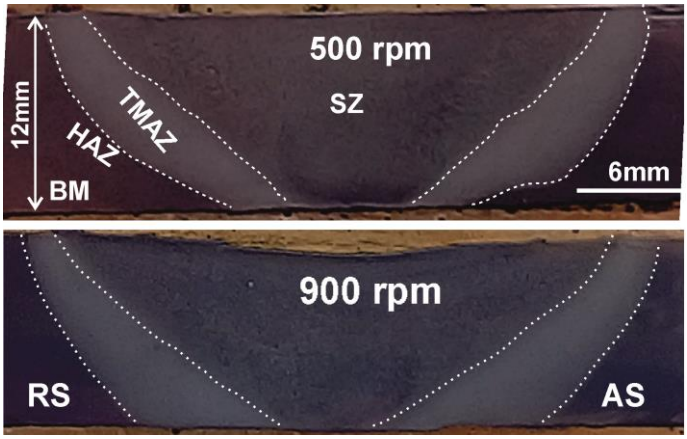

Figure 4.3.3 Macrograph of transverse cross-section of FSW joints at 500 and 900 rpm depicting SZ, TMAZ, HAZ and BM. "AS" and "RS" marked in figure denote advancing side and retreating side

Metallographic characterisation of various regions of the weld joint in the as-welded and various post weld heat treated conditions were carried out at various locations of the welded sample, as marked in Figure.4.3.4.

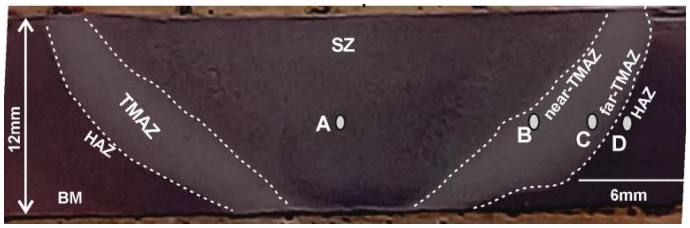

Figure 4.3.4 Macrograph showing transverse cross-section of friction stir weld joint indicating various metallurgical zones and the marks pertain to the areas where the microstructures are taken in the mid-thickness regions of SZ, TMAZ and HAZ

The optical images of various zones (marked in Figure.4.3.4) in the as-welded state for 500 and 900 rpm conditions are presented in Figures 4.3.5 and 4.3.6 respectively while corresponding FE-SEM images are depicted in Figures 4.3.7 and 4.3.8. The microstructures obtained in various zones during welding acted as pointers for the peak temperatures achieved, and also reflected on cooling rates. The SZs exhibited martensite in coarse grains and revealed carbide-free grain boundaries. The microstructures in TMAZ, lying close to SZ (near-TMAZ) and far away from SZ (far-TMAZ) were noticed to be different. The near-TMAZ displayed martensite in fine grains and some undissolved carbides in the matrix. The temperature in near-TMAZ region appears to be just above A_{c3} but not very high enough to dissolve all MC type carbides. The fine grain size could result from the continuous dynamic recrystallization occurring in austenitic region in the near-TMAZ and martensite forms on transformation of austenite on subsequent cooling.

The far-TMAZ showed some amount of tempered martensite and α- ferrite (Figures 4.3.5 and 4.3.7). The minimum cooling rate required for the onset of ferrite

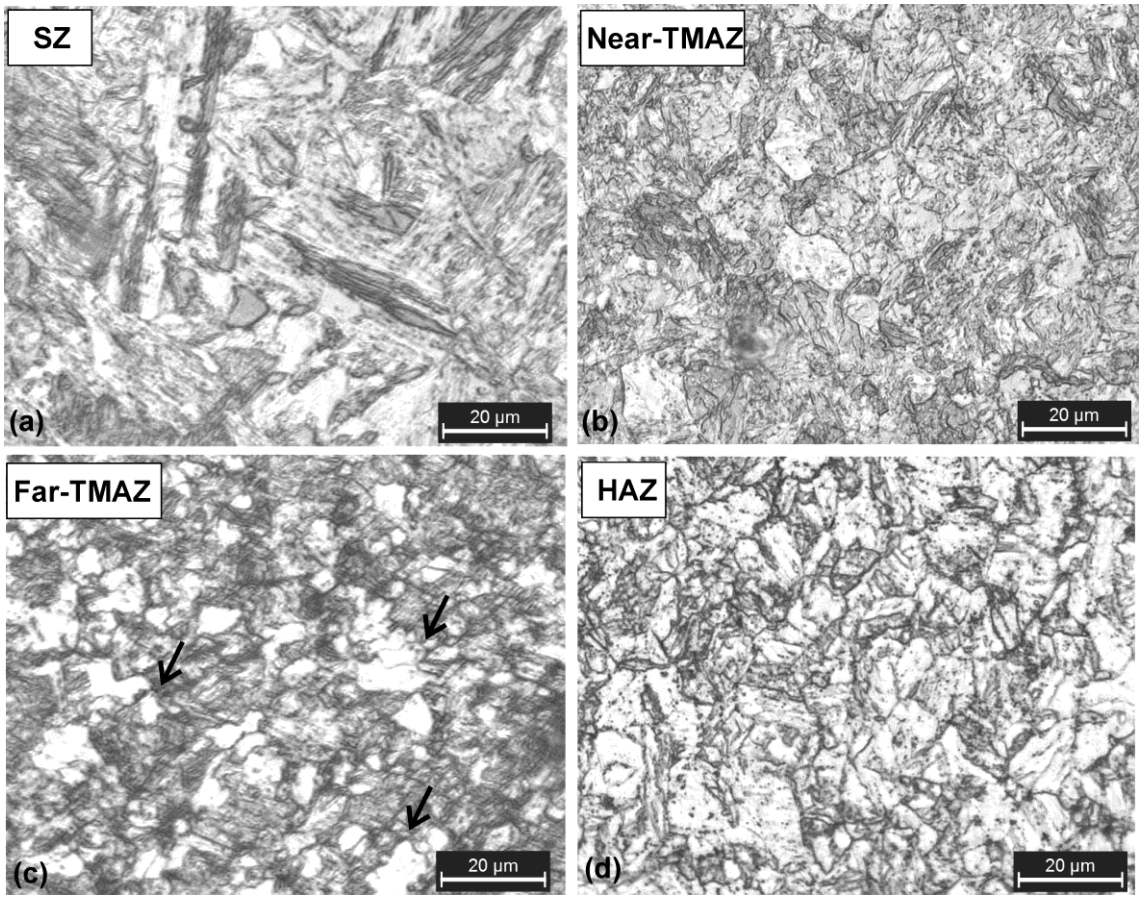

Figure 4.3.5 Optical micrographs of 500 rpm weld in as-welded condition (a) SZ (b) near-TMAZ (c) Far-TMAZ showing a mixture of α-ferrite (arrow marked) and martensite (d) HAZ.

transformation from austenite was reported to be 60 K/min [9, 23]. Cooling rates slower than 60 K/min have been reported to cause the occurrence of ferrite from austenite along the grain boundaries. This type of microstructure gives an indication that the peak temperature achieved in far–TMAZ during FSW falls in intercritical zone and cooling rates are slower than 60 $Kmin^{-1}$[9, 24].

In HAZ, the carbides persisted on grain boundaries but found coarsened in comparison to the unaffected base metal probably due to over tempering of carbides. The peak temperature experienced in HAZ (zone-d) appears to be below Ac_1 and this type of microstructure promotes greater reduction in strength and hardness.

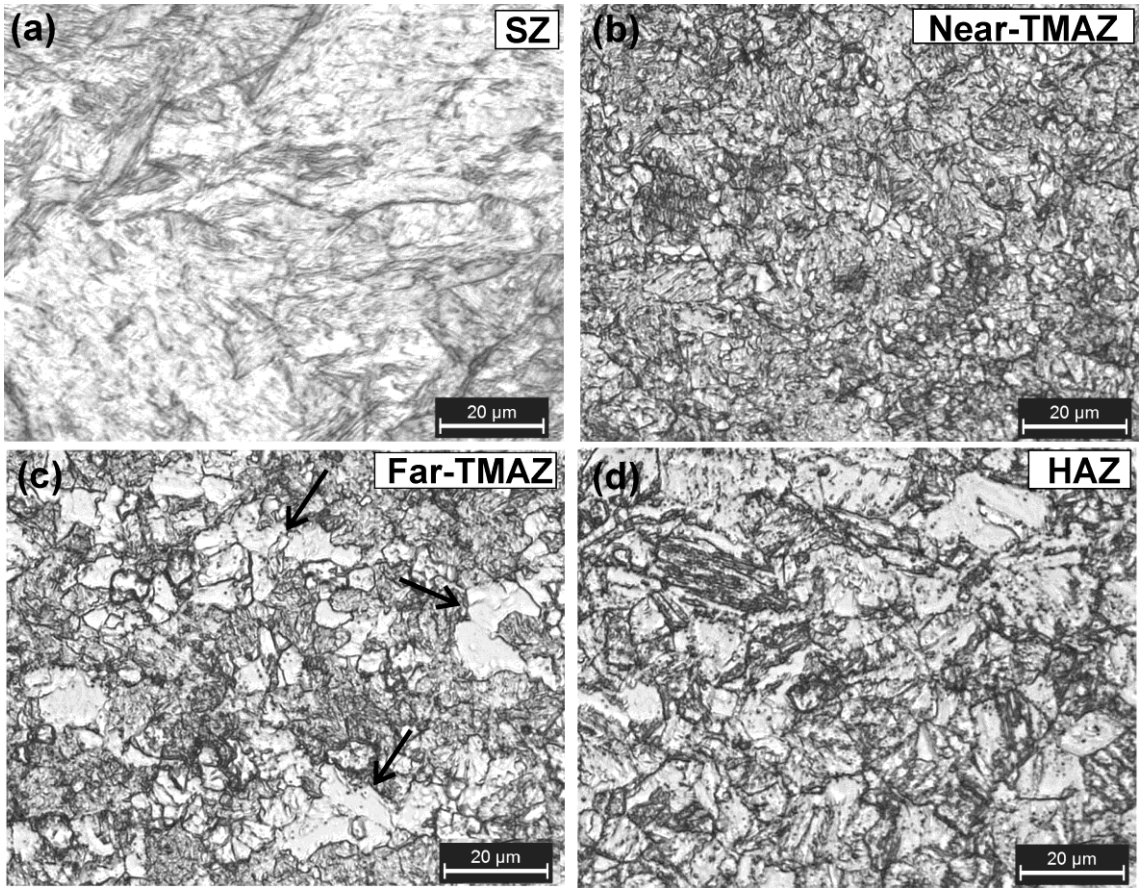

Figure 4.3.6 Optical micrographs of 900 rpm weld in as-welded condition (a) SZ (b) near-TMAZ (c) Far-TMAZ showing a mixture of α-ferrite (arrow marked) and martensite (d) HAZ

The far-TMAZ zone could not be observed in case of FSW of 6-mm-thick plate as discussed in section 4.1.The reason could be explained as follows.

The highest temperature experienced during FSW is in the surface near regions of the weld nugget. In case of FSW of thin sections, conduction can easily transmit the heat throughout the thickness of the material leading to no or very small temperature gradient. With increase in section thickness the heat imbalance also increases and therefore high welding temperatures are seen near the surface of the weld to attain the required heat throughout the rest of the weld. On increasing the thicknesses of the plate, FSW produced higher heat input, considerable temperature gradients and promotedslow cooling rates across the weld joint. This led to various zones developed across the SZ, dependent on peak temperatures achieved and cooling rates.

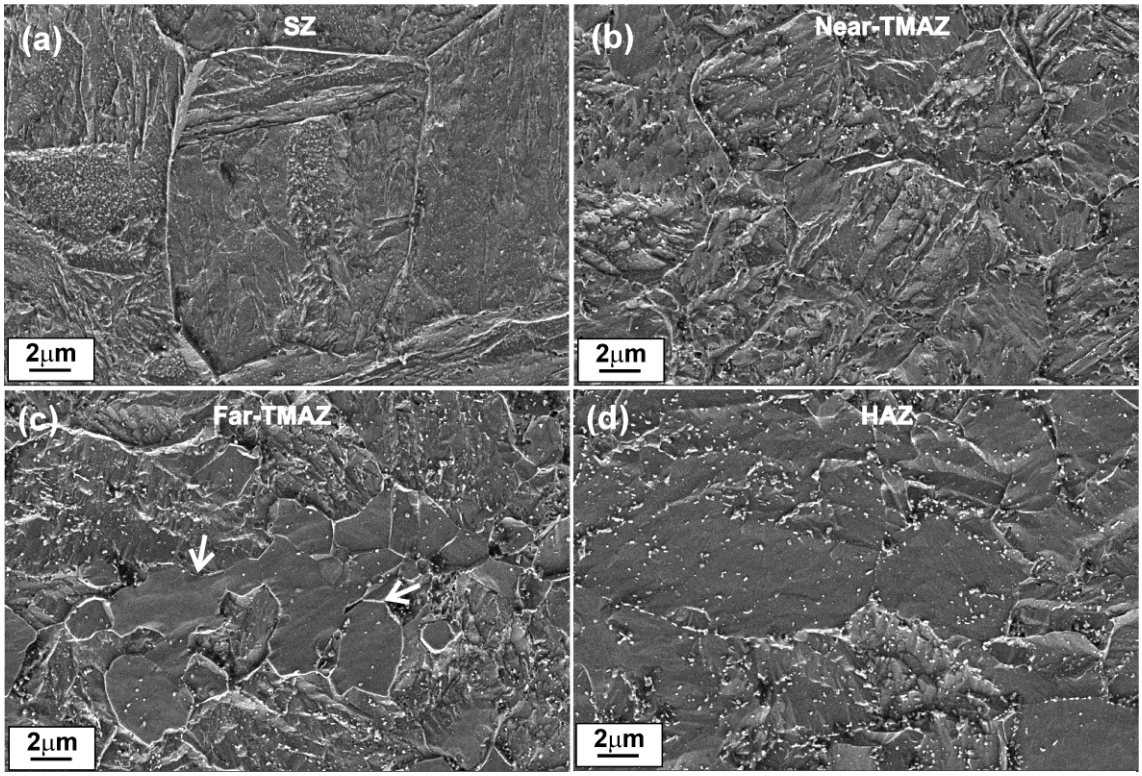

Figure 4.3.7 Field–emission scanning electron micrographs of 500 rpm weld in as-welded condition (a) SZ (b) near-TMAZ (c) Far-TMAZ showing a mixture of α-ferrite (arrow marked) and martensite (d) HAZ.

Similar microstructural aspects were noticed in case of 900 rpm condition (Figures 4.3.6 and 4.3.8). At 900 rpm, there has been slight increase in the width of SZ, TMAZ and HAZ compared to 500 rpm condition. Figure 4.3.9 illustrates the EBSD grain orientation maps of base metal and for the various zones developed at 500 rpm condition. The grains are clearly discerned in the EBSD crystal orientation image maps. No evidence for preferred orientation was observed. The fraction of low angle boundaries was higher at all zones compared with the base metal. Near-TMAZ (Figure 4.3.9(b)) showed very high fraction of fine grains and developed large number of LAGBs lending support to the hypothesis of continuous recovery and recrystallization during FSW compared to far-TMAZ (Figure 4.3.9(c)). Figure 4.3.10 depicts the grain size distribution and variation that occurred in various zones of the weld at 500 rpm condition.

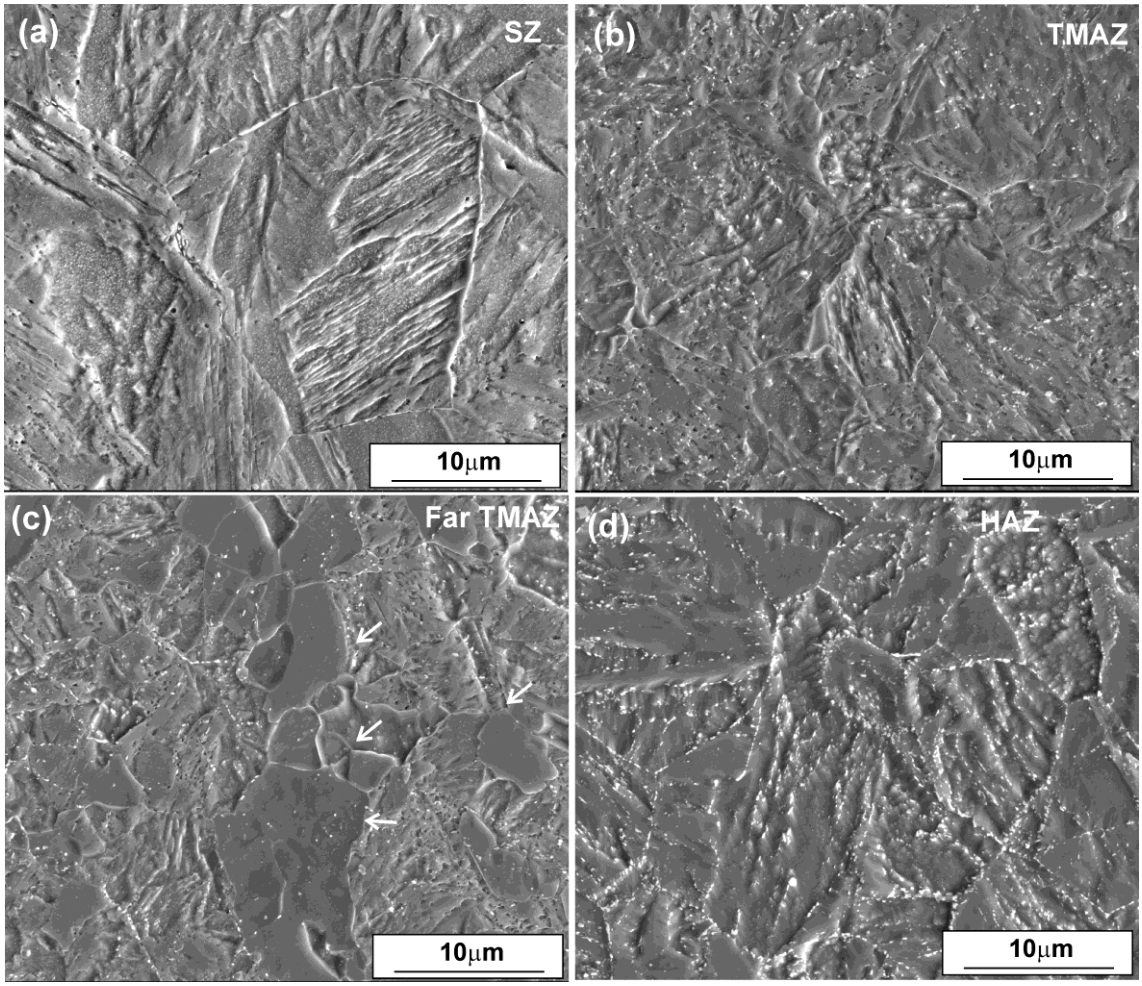

Figure 4.3.8 Field–emission scanning electron micrographs of 900 rpm weld in as-welded condition (a) SZ (b) near-TMAZ (c) Far-TMAZ showing a mixture of α-ferrite (arrow marked) and martensite (d) HAZ

The grain size distribution at far-TMAZ (Figure 4.3.10(c)) bears resemblance to that in the BM (Figure 4.3.10 (d)). In the SZ the distribution is very broad, with the presence of both fine and very high proportionate of coarse grains as shown in Figure4.3.10 (a). The grain size distribution at near-TMAZ (Figure 4.3.10(b)) reveals very high fraction of fine grains compared to base metal .The average grain size in SZ was 18 μm compared to 5 μm obtained in case of near-TMAZ. The SZs showed an average grain size of 18 and 19 μm for 500 and 900 rpm conditions respectively.

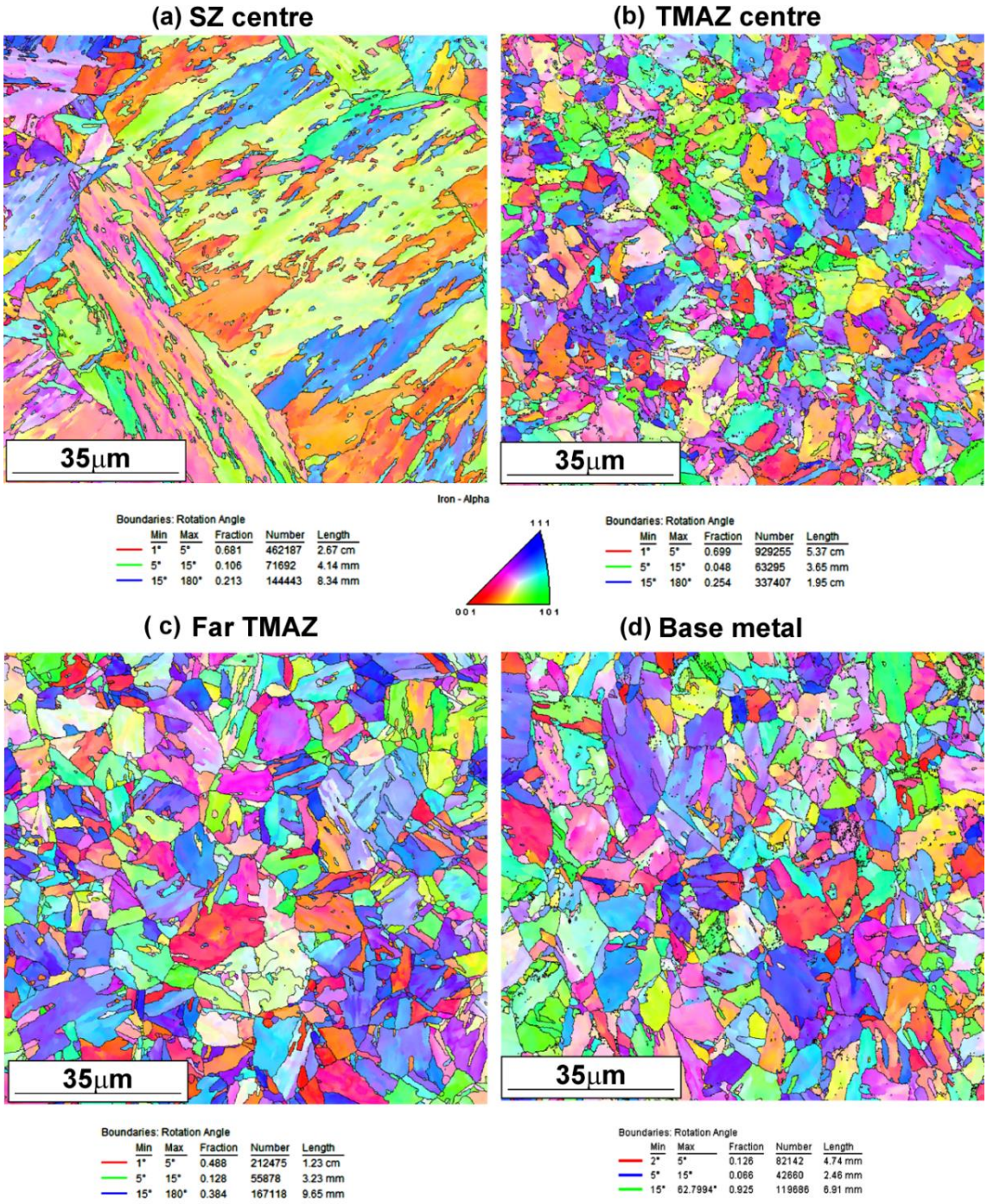

Figure 4.3.9 Grain boundary orientation maps of 500 rpm in as-welded condition (a) SZ (b) Near-TMAZ (c) Far-TMAZ, and (d) BM.

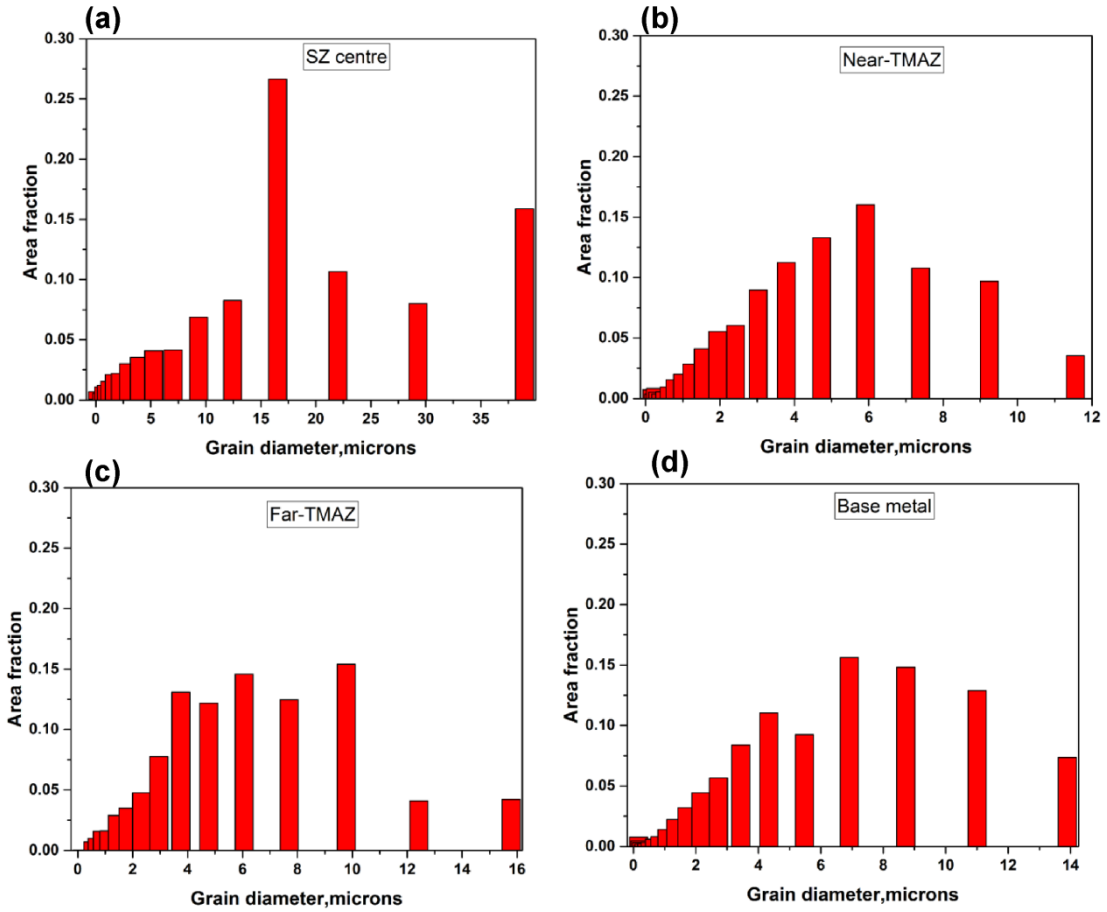

Figure 4.3.10 Grain size distribution of 500 rpm in as-welded condition (a) SZ (b) Near-TMAZ (c) Far-TMAZ , and (d) BM.

4.3.3. Microstructure of friction stir weld joints in post weld heat-treated conditions

The SEM micrographs of SZ, TMAZ, far-TMAZ and HAZ after PWDT for both 500 and 900 rpm conditions are shown in Figure 4.3.11 Figure 4.3.12. PWDT caused the re-appearance of $M_{23}C_6$ on grain boundaries in SZ and TMAZ. The SZ microstructure at 500 and 900 rpm as shown in Figure 4.3.11(a) and Figure 4.3.12 (a) consisted of tempered martensite with intra lath precipitation. In TMAZ the precipitation of carbides was more heterogeneous in the intra-granular regions; some grains displayed very coarse and clustered precipitates whereas few grains had regions that are free from precipitation (Figures 4.3.11 (b, c) and 4.3.12 (b, c)). The precipitate ripening was more intense in HAZ of 900 rpm (Figure 4.3.12 (d)).

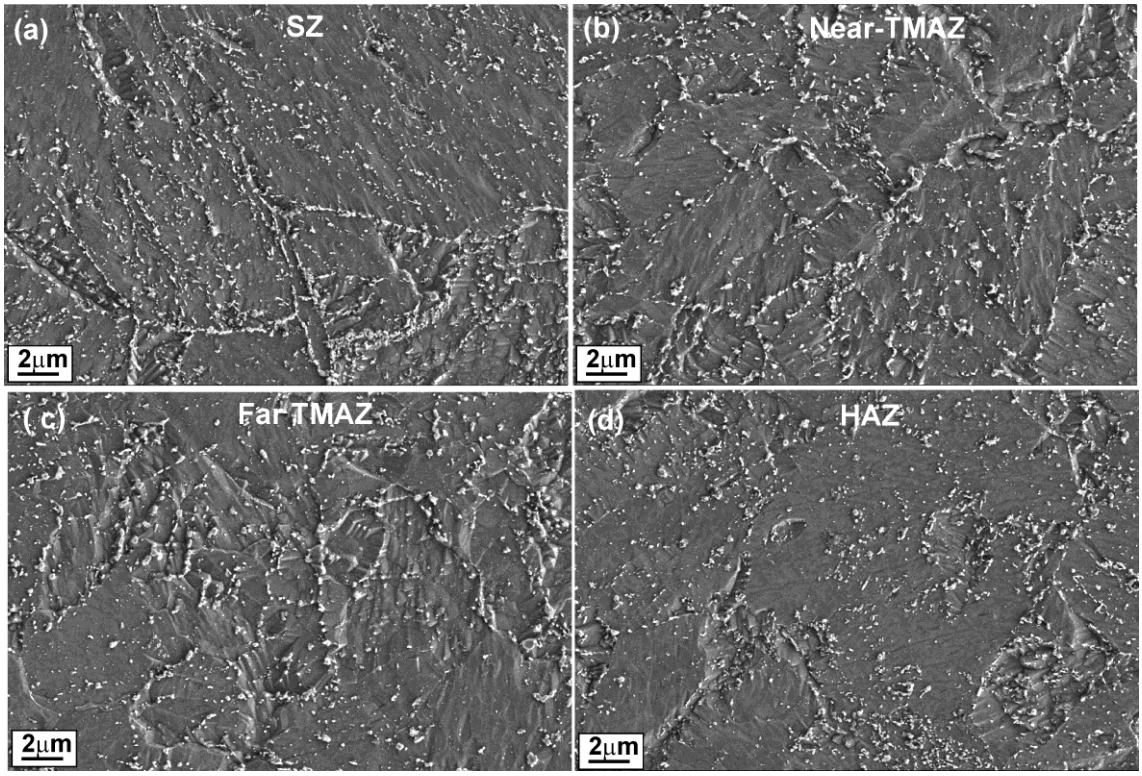

Figure 4.3.11 Field emission scanning electron micrographs in PWDT condition illustrating precipitation behaviour of carbides in different zones for 500 rpm condition

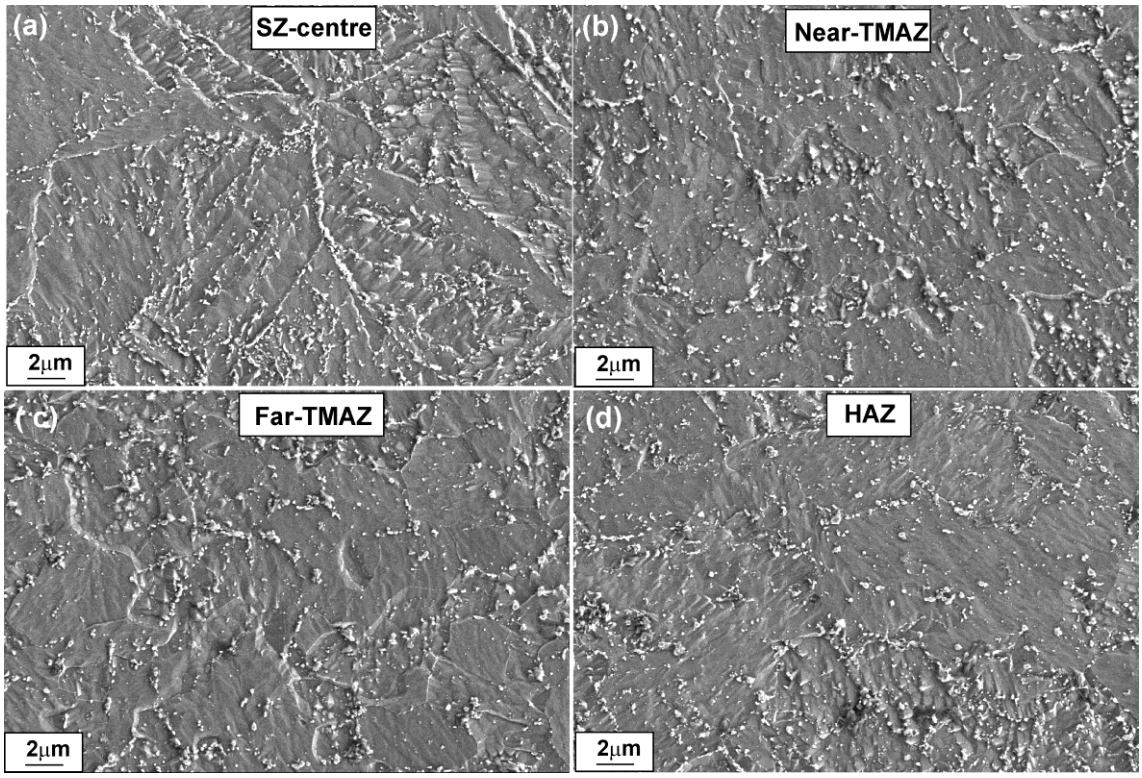

Figure 4.3.12 Field emission scanning electron micrographs in PWDT condition illustrating precipitation behaviour of carbides in different zones for 900 rpm condition.

The SEM photographs presented in Figures 4.3.13 and 4.3.14 illustrates the microstructures developed in various zones after PWNT for 500 and 900 rpm conditions. PWNT restored the microstructures of SZ, TMAZ and HAZ to the state existing in parent metal prior to FSW. After PWNT treatment the SZ has shown a uniform distribution of precipitates in the intragranular regions and eliminated the heterogeneous microstructure developed in the as-welded state in near-TMAZ, far-TMAZ and HAZ.

The re-austenitization (normalizing) treatment caused the dissolution of coarse carbides which are considered to be responsible for HAZ softening and the transformation of α-ferrite to austenite in far-TMAZ. The post weld normalizing treatment eliminated the microstructural inhomogeneity across the SZ, near-TMAZ, far-TMAZ and HAZ and led to the formation of martensite. The subsequent tempering treatment led to re-precipitation of $M_{23}C_6$ and MX at appropriate locations in optimum size and distribution in case of both 500 and 900 rpm conditions

4.3.4. Microhardness

The impact of developed microstructures, at two rotational speeds in various zones, is reflected in Vickers hardness profile obtained on transverse cross-section of welds in the mid-thickness region (Figure 4.3.15). In the as-welded state, SZs exhibited very high hardness irrespective of the rotational speed (Figure 4.3.15 (a, b)). A gradual reduction in hardness occurred in TMAZ, and finally attained dip in hardness in the very narrow HAZ, prior to reaching the base metal value which is 225 HV. The SZs displayed higher hardness with several peaks and valleys (Figure 4.3.15 (a, b)).The hardness in TMAZ varied from 475 HV to 300 HV. After PWHTs, hardness in the SZ

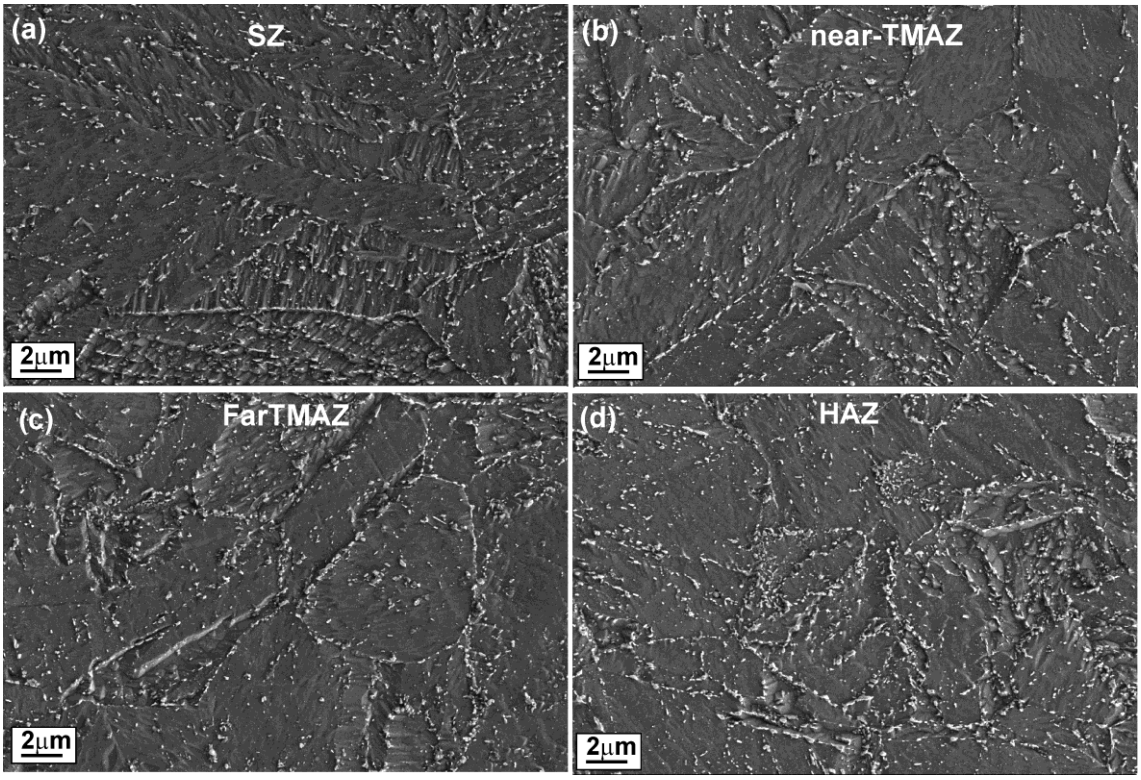

Figure 4.3.13 Scanning electron micrographs illustrating intra- and intergranular precipitation of carbides in various zones for 500 rpm condition after PWNT treatment

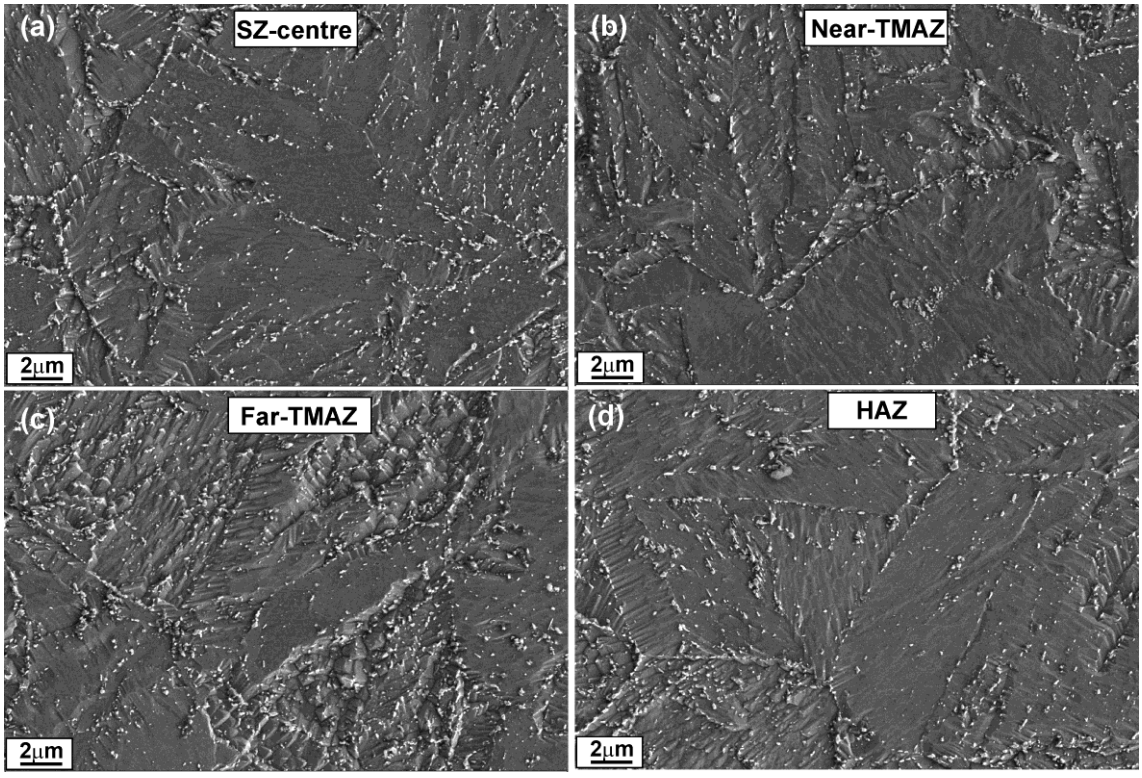

Figure 4.3.14 Scanning electron micrographs after PWNT treatment illustrating intra- and intergranular precipitation of carbides in various zones for 900 rpm condition.

was drastically decreased (Figure 4.3.15 (a, b)). PWDT caused a pronounced dip in hardness in HAZ.The PWNT treatment eliminated the microstructural inhomogeneity across the joint and displayed uniformity in hardness across the weld joint

A comparative evaluation of section thickness (6 and 12 mm) on microhardness profile at 500 rpm is shown in Figure 4.3.16. On increasing the thicknesses of the plate, FSW produced higher heat input (11.49kJ/mm) which promoted slow cooling rates across the weld joint and subsequently led to microstructural variation across the joint. Zheng et al. [24] reported that slower cooling rates promoted the formation of α-ferrite and coarsening of laths in CLAM steel. The occurrence of coarse grains and increased lath width in SZ, and the presence of α-ferrite in far-TMAZ appear to be responsible for inhomogeneous nature and lower hardness in 12 mm thick welded joints.

4.3.5. Impact toughness

Impact toughness values of 12 mm thick weld joints and BM were determined by employing 55×10×10 mm Charpy V-notch full-size samples. In the as-welded state, both 500 and 900 rpm conditions exhibited poor toughness; the low toughness seems to result from the combined effects of coarse grain size and martensite formed in the SZ. The PWDT significantly improved the impact toughness of weld joints and exhibited toughness close to that obtained for BM The fracture surface of impact tested samples, as shown in Figure 4.3.17 indicated cleavage mode of fracture at 500 and 900 rpm in the as-welded state. The fracture surfaces of the impact tested samples in PWDT condition exhibited ductile mode of fracture irrespective of the rotational speed. The improvement in toughness of both the weld joints can be attributed to the overall presence of tempered martensite structure after PWDT treatment

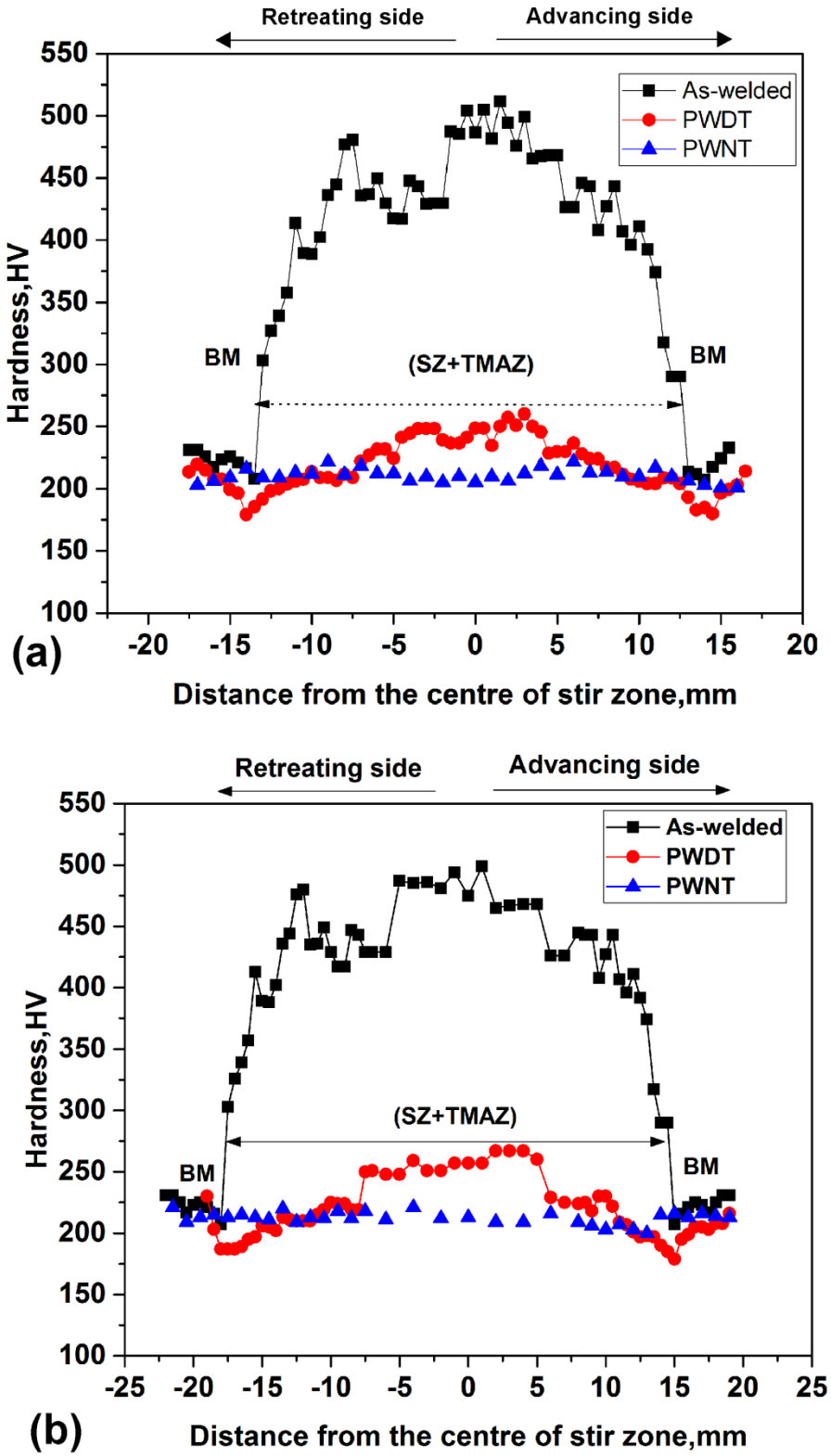

Figure 4.3.15 Hardness profiles of the friction stir welds across the stir zone in various conditions (a) 500 rpm and (b) 900 rpm condition.

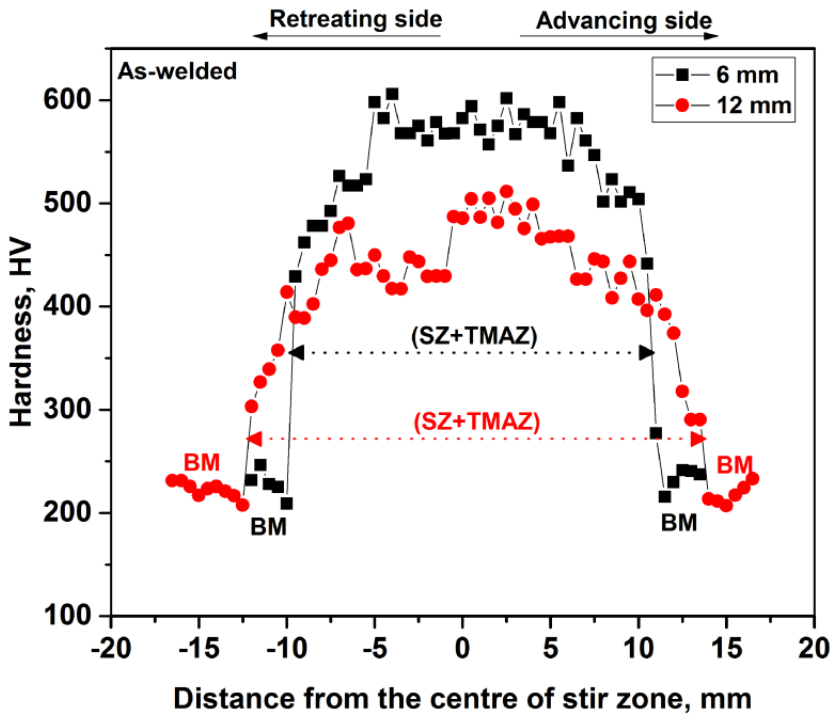

Figure 4.3.16 Vickers microhardness profile in as-welded state at 500 rpm condition for 6 and 12 mm thicknesses welds.

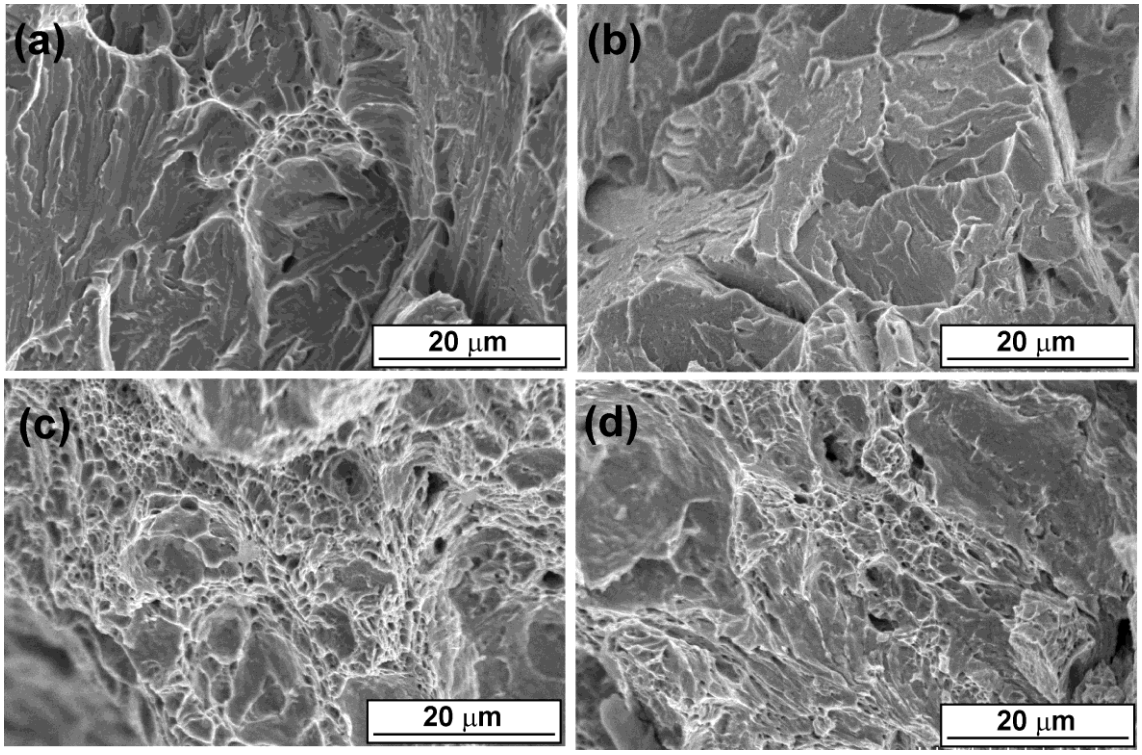

Figure 4.3.17 Fractographs of impact tested samples for 500 and 900 rpm conditions revealing cleavage fracture in as-welded state (a, b) and ductile fracture for PWDT condition (c, d) respectively.

Table 4.3.1 Details of full-size Charpy V-notch impact toughness values in as-welded, and PWDT conditions

Material condition	Impact energy, J	Impact energy, J (PWDT)
Base metal	244	263
500 rpm	31	243
900 rpm	19	227

4.4. Role of evolving microstructure on the mechanical properties in the as-welded and post weld heat-treated states

4.4.1. Introduction

EBW a low heat input and high speed fusion welding process is one of the advanced methods of joining being considered for the fabrication of structural components of TBMs as it produces a smaller HAZ, thereby the deleterious effects associated with the HAZ could be minimised. However, it is a very difficult task to eliminate the occurrence of δ- ferrite that nucleates during the solidification of liquid metal generated by conventional and advanced fusion welding processes. The amount of δ-ferrite retained in the weld metal depends upon the chemical composition of the BM and cooling rates achieved during the solidification of the weld metal [3, 25]. The occurrence of δ-ferrite in fusion zone has been credited with rise of ductile to brittle transition temperature (DBTT), lower impact toughness and poor creep properties [26, 27].In general the tendency to retain the δ-ferrite depends on the time spent by the weld metal in the δ-ferrite +austenite and austenite phase field during cooling. Longer the time spent in this temperature range more will be the transformation of δ-ferrite to austenite and less would be the volume fraction of the residual δ- ferrite in the weld metal [3].Recent investigations indicated that the δ-ferrite in the weld metal could be eliminated by restricting the W level to approximately 1wt. % [28]. The decision to use INRAFM steel (9Cr-1.4W-0.06Ta) calls for finding out appropriate methods to eliminate the δ-ferrite in the weld metal. Some of the PWHTs appear to have potential for the reduction /elimination of δ-ferrite in the weld zone. The results of EBW of INRAFM steel in as-welded and post weld heat treated conditions on evolving microstructure and hardness in various zones and the dependence of tensile

properties and impact strength on post weld heat treatments are presented and discussed in the subsequent sections.

4.4.2. Microstructure of the weld joint in as-welded state

The optical microstructure of EBW joint from 12 mm thick plate in as-welded condition is shown in Figure 4.4.1(a). The EB weld joint is made up of BM, weld metal (WM) and HAZ. There is no TMAZ as observed in FSW joints .The width of HAZ is about 600 microns. The occurrence of small HAZ serves as a pointer for low heat input associated with EBW process. The transverse cross-section showed full penetration welds with no indication of defects, which was confirmed by radiography analysis. The microstructural evolution in weld metal and HAZ was captured at four different locations as pointed in Figure 4.4.1(a) of the weld joint. Microstructure varied substantially across the weld joint and depended to a greater extent on the peak temperature attained during EBW at the marked locations in Figure 4.4.1 (b-e). In the weld zone, the maximum temperature experienced corresponds to the molten metal which enables the dissolution of all prior existing precipitates. The microstructure in the weld zone displayed martensite with a small amount of δ-ferrite in the matrix (Figure 4.4.1 (b)). Under the equilibrium conditions the molten metal solidifies as δ-ferrite and then transforms to austenite; the transformation of δ-ferrite to austenite commences around 1573 K and gets completed at 1473K [3]. However, the equilibrium transformation may not be complete at the prevailing fast cooling rates in EBW process. Therefore, a small amount of δ-ferrite would be retained in the weld metal as depicted in Figure 4.4.1(b). The volume fraction of δ-ferrite in the weld zone was found to be 1.99%. It has been estimated by Image J analysis software by measuring from 20 optical micrographs taken from each one of the three samples extracted from the same weld bead. Micro hardness measurements at 50g load revealed 198 HV and 450 HV for

δ-ferrite and martensite phases respectively (Figure 4.4.2). This observation is a clear indication of low resistance to deformation of δ-ferrite and hence to be avoided. Delta-ferrite is an undesirable phase since it is known to impair the impact toughness of the welds.

Microstructure in the HAZ was found to be very complex and reflected the temperatures seen across the HAZ due to thermal gradient experienced during EBW process. The representative microstructures taken from three different regions of HAZ are presented in Figure 4.4.1(c-e). During welding the HAZ region close to the fusion boundary experience temperatures well above Ac_3 (the temperature corresponding to the completion of transformation of α-ferrite to austenite upon heating). At these temperatures dissolution of the intra- and inter-granular $M_{23}C_6$ particles which act as obstacles to the growth of austenite grains occur. As a result, the microstructure in the region (c) displayed coarse grain austenite which subsequently transformed into high carbon martensite on cooling.

The temperature within HAZ decreases with increasing distance away from the fusion boundary and the peak temperature experienced in region (d) might be just above Ac_3. Therefore, in the zone-(d) grain growth is restricted by the incomplete dissolution of carbides during welding and the resulting microstructure at room temperature would be low carbon martensite in fine grains as shown in Figure 4.4.1 (d).

The microstructure at point (e) shows α-ferrite and martensite. The peak temperature experienced in region (e) appears to be in between A_{c3} and A_{c1}.Therefore the microstructure seen in Figure 4.4.1 (e) corresponds to the intercritical region (α-ferrite +austenite) and subsequent cooling transforms austenite to martensite. Away from the intercritical region, a very narrow zone towards base metal experience temperatures

below A_{c1} and therefore undergoes over tempering of carbides accompanied by reduction in hardness in comparison to the unaffected base metal. However this region is found to be insignificant in this study owing to narrow HAZ developed as a result of the low heat input employed in EBW.

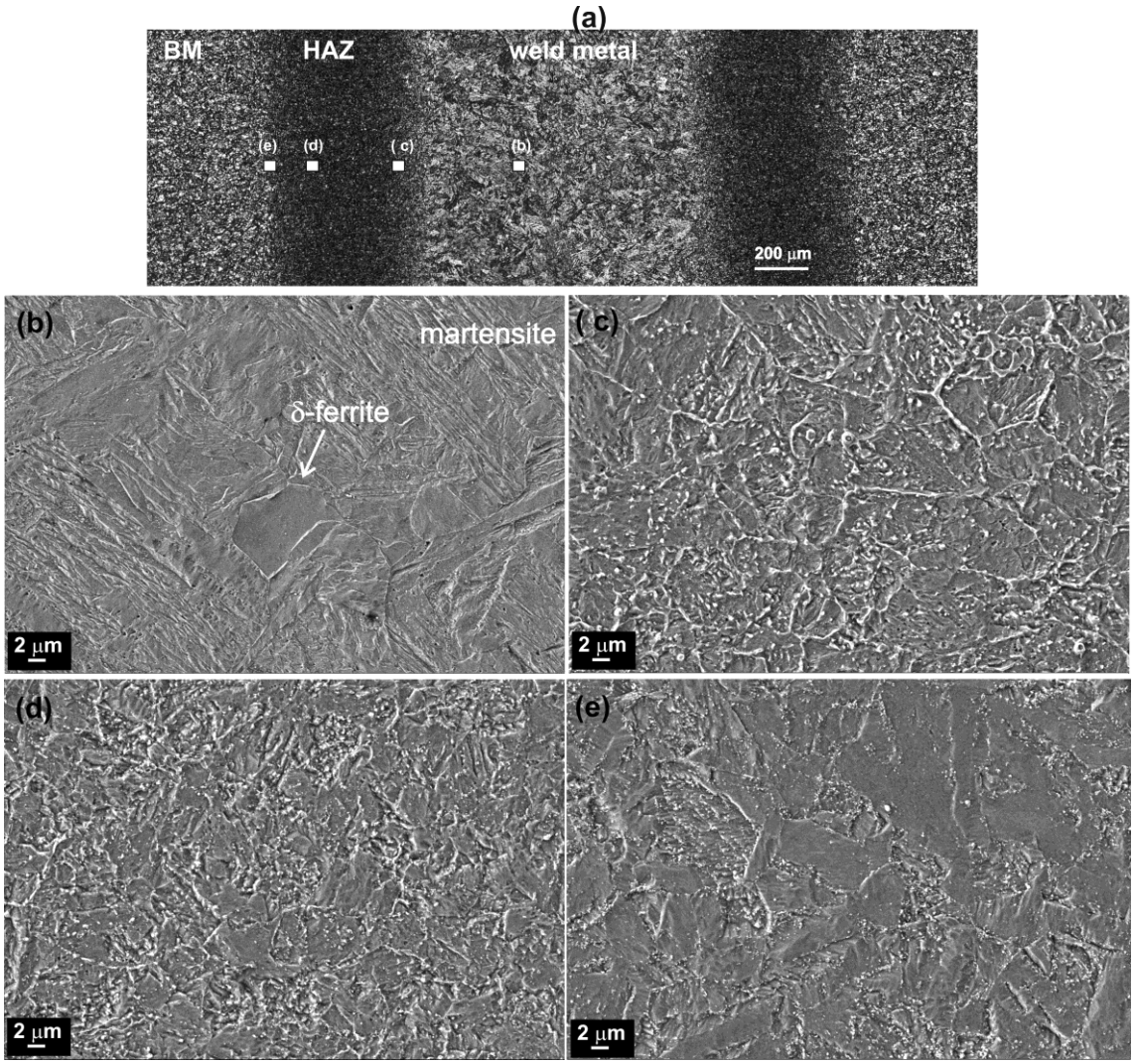

Figure 4.4.1 (a) Optical microstructure of the cross-sectional view of the weld joint illustrating various zones across the joint. Corresponding FE-SEM images taken at various locations marked in the optical micrograph. (b)Weld zone (c) Coarse grain HAZ (d) Fine grain HAZ (e) Intercritical region.

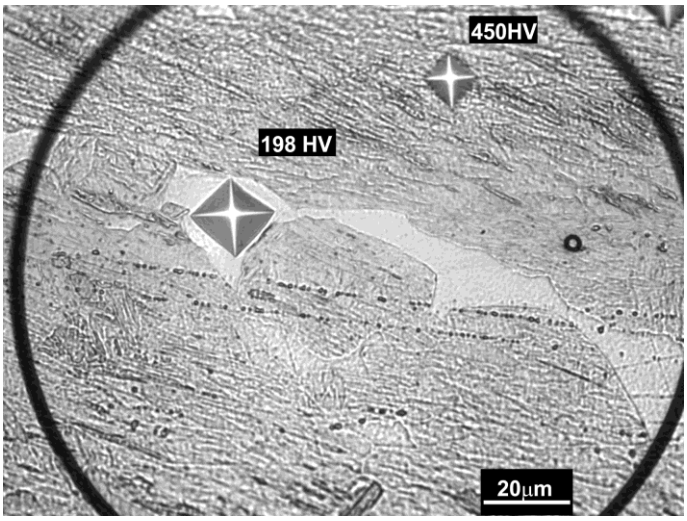

Figure 4.4.2 Optical microstructure of weld zone revealing the Vickers indentation marks taken at 50 g load in δ-ferrite and martensite phases and their corresponding hardness values.

4.4.3. Microstructure of weld joints in post weld heat-treated conditions

Figures 4.4.3 and 4.4.4 illustrates the optical and FE-SEM images of weld region respectively in as-welded, PWDT and PWNT conditions. Figure 4.4.5 depicts various features of microstructure obtained by EBSD and corresponding image quality figures of BM and weld region in the as-welded and PWNT states. The important observations made after PWDT include: (i) the δ-ferrite observed in as-welded state (Figure 4.4.3(a) and 4.4.4(a)) could not be eliminated (Figure 4.4.4(b)), (ii) precipitation of $M_{23}C_6$ occurred on δ-ferrite phase boundaries, (iii) microstructure still contained large number of martensite laths (Figure 4.4.4(b)) and (iv) carbide distribution in intra granular regions is more heterogeneous. The PWNT caused the transformation of as-welded martensite structure to α-ferrite and carbides and the disappearance of δ-ferrite (Figure 4.4.3(c) and 4.4.4(c)) in the weld region. The carbide precipitation was more or less homogeneous after PWNT and overall microstructure resembled to that displayed by starting material.

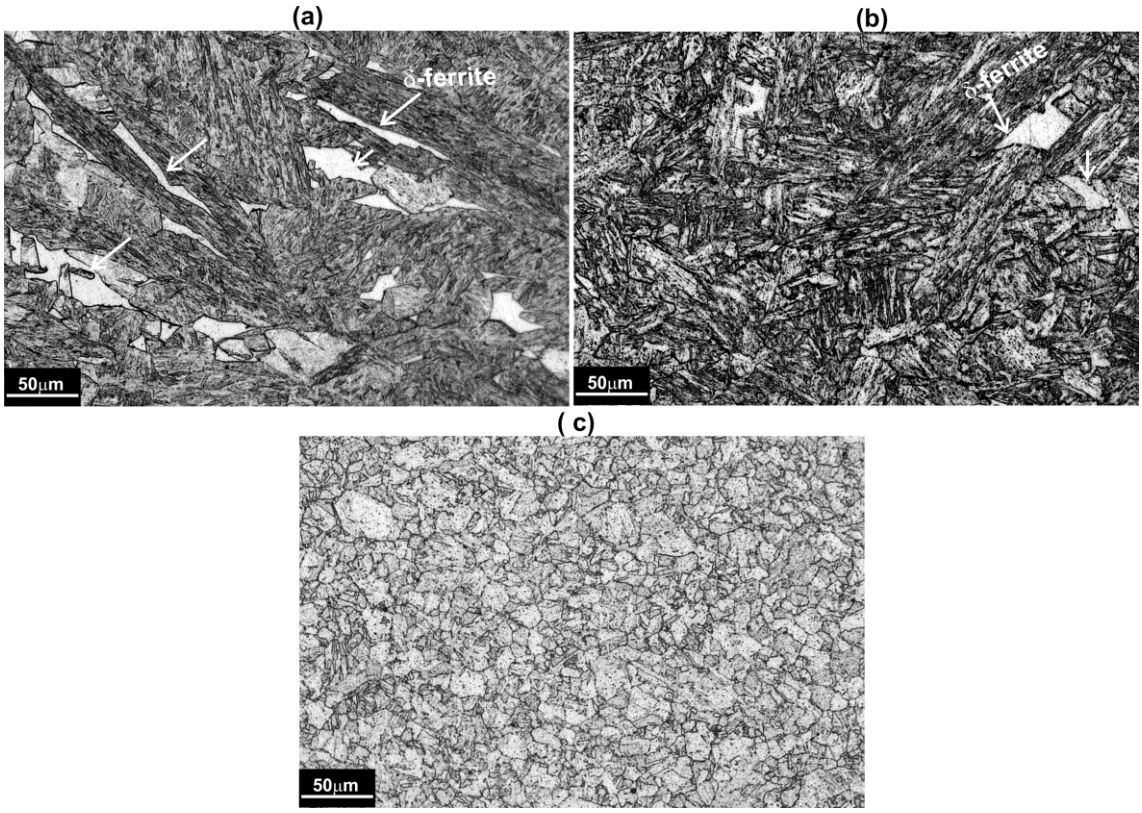

Figure 4.4.3 Optical images of weld zones in (a) as-welded condition showing δ-ferrite in martensite (b) PWDT condition revealing tempered martensite and presence of δ-ferrite and (c) PWNT condition revealing fully tempered martensite, fine PAGBs and no evidence of δ-ferrite.

The grain boundaries are clearly discerned in the EBSD crystal orientation image maps in Figure 4.4.5. There was no evidence for preferred orientation. Figure 4.4.5 shows the presence of both the low angle boundaries (defined by 2 deg ≤ θ min ≤ 15 deg) and high angle boundaries (defined by misorientation angle θ min ≥ 15 deg) in the weld zone prior to and after PWHTs. The orientation of grains was random in the weld metal irrespective of the heat treatment condition. EBSD crystal orientation maps and image quality figures of weld metal confirmed the presence of martensite and δ-ferrite in as-welded condition (Figure 4.4.5 (b, e)) while PWNT caused fine grain structure in the weld metal (Figure 4.4.5(c and f)).

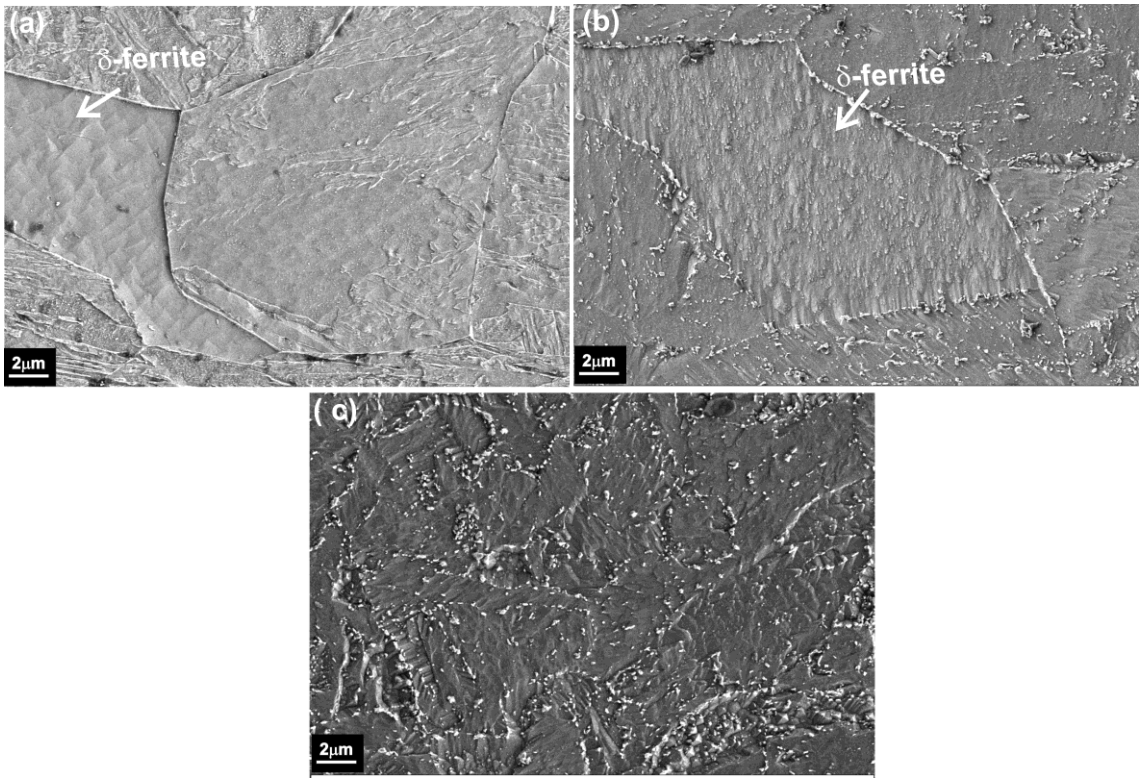

Figure 4.4.4 Field emission scanning electron micrographs of weld zones in (a) as-welded condition showing martensite in coarse grains and δ-ferrite (b) PWDT condition revealing tempered martensite and the presence of $M_{23}C_6$ layer in the interface between δ-ferrite grains and martensite matrix (c) PWNT condition revealing fully tempered martensite.

The fraction of low as well as high angle boundaries was higher after PWNT (Figure 4.4.5(f)) compared with those recorded in BM and as-welded conditions (Figure 4.4.5(a, d) and 4.4.5(b,e)) suggesting the occurrence of recrystallization. After PWNT the coarse martensite structure disappeared and resulted in fine grains of tempered martensite. Martensitic transformation in the weld zone during EBW generates very high dislocation density and more strain in the lattice structure [29]. During re-austenitization the amount of stored energy required to initiate recrystallization appears to be sufficient promoting fine grain size in the weld zone. Microstructure observation shows no evidence for δ-ferrite in the weld zone after PWNT. The high temperature associated with the re-austenitization treatment caused

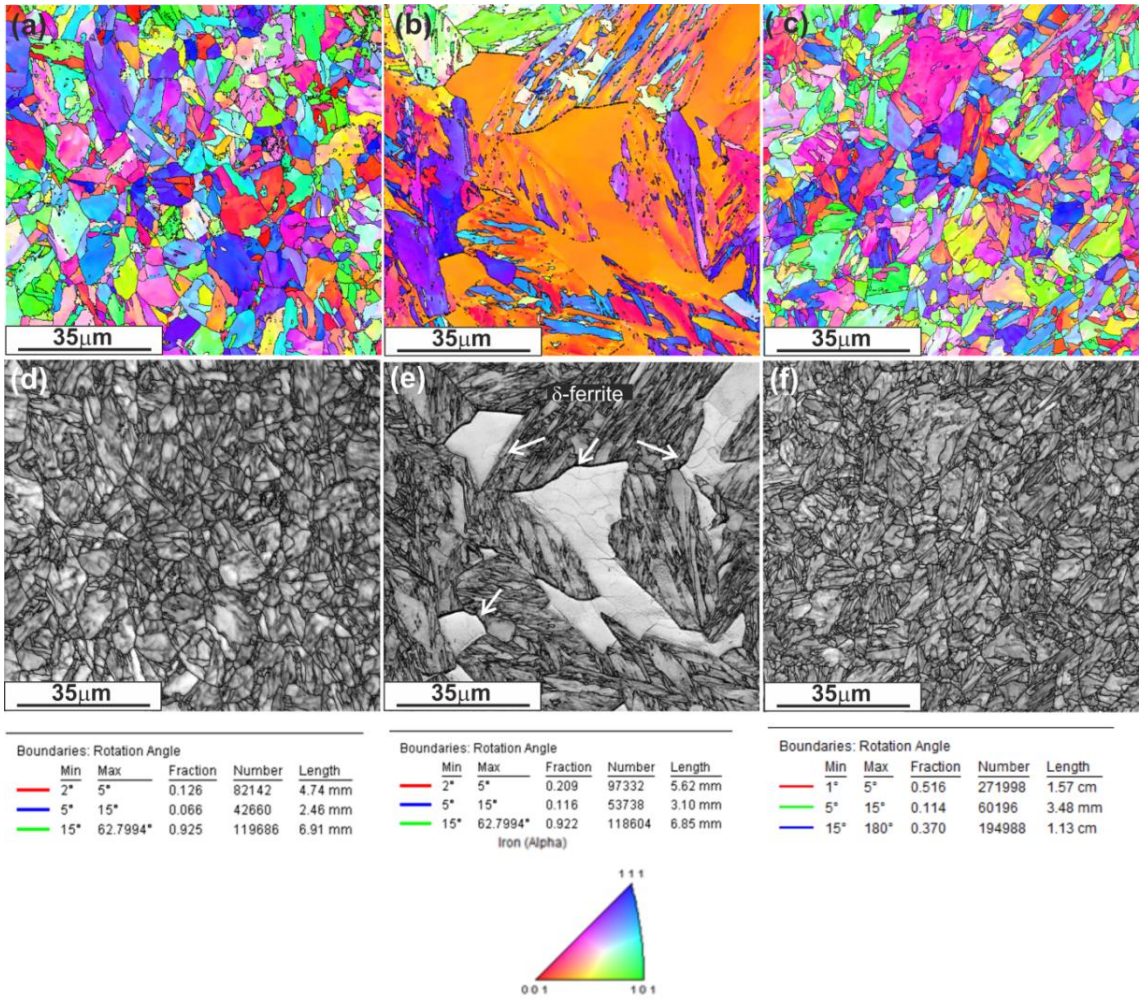

Figure 4.4.5 EBSD crystal orientation map and image quality figures of base metal (a, d). Weld in as-welded condition showing δ-ferrite in martensite matrix (b, e) and weld after PWNT condition (c, f).

the dissolution of coarse carbides and the transformation of δ-ferrite to austenite through solid state diffusion of ferrite forming elements. The subsequent tempering treatment eliminated the microstructural inhomogeneity across the weld joint by virtue of the transformation to tempered martensite.

4.4.4. Microhardness in as-welded and PWHT conditions

Vickers microhardness profiles of weld joints in the transverse cross-section at mid-thickness region for as-welded, PWDT and PWNT states are shown in Figure 4.4.6. In the as-welded state, the weld zone and HAZ exhibited very high hardness in

the range of 400-475 HV. Higher hardness in the weld metal and HAZ could be associated with the formation of martensite. Coarse grain HAZ region close to fusion boundary depicted high hardness of 475 HV due to the occurrence of high carbon martensite. The intercritical zone exhibited 220 HV which is lower than that of the base metal (235 HV).

There has been substantial decrease in hardness in the weld zone after PWDT (Figure 4.4.6 (a)). The decrease in hardness could be attributed to synergistic effects associated with the annihilation of dislocations associated with transformation to martensite, loss of solid solution strengthening elements from the matrix due to nucleation and growth of $M_{23}C_6$ and MX precipitates and increase in the width of martensite laths experiencing the conversion to tempered martensite structure. In PWDT condition, the hardness across the weld joint was not uniform (Figure 4.4.6 (a)).

The PWNT condition promoted more or less uniform hardness across the weld joint (Figure 4.4.6 (b)). This observation has been found to have correlation with more or less homogeneous tempered martensite structure developed in all the zones of weld joint. The hardness was about 210 HV, which is being considered as an acceptable value for high creep resistance of ferritic-martensitic steels

4.4.5. Impact toughness

In the development of RAFM steels, the high impact toughness was considered as a qualitative and prime indicator for ensuring the materials resistance to raise the ductile-to-brittle transition temperature (DBTT) upon irradiation. In this study, room temperature impact toughness (expressed as impact energy) of BM, as-welded joint and

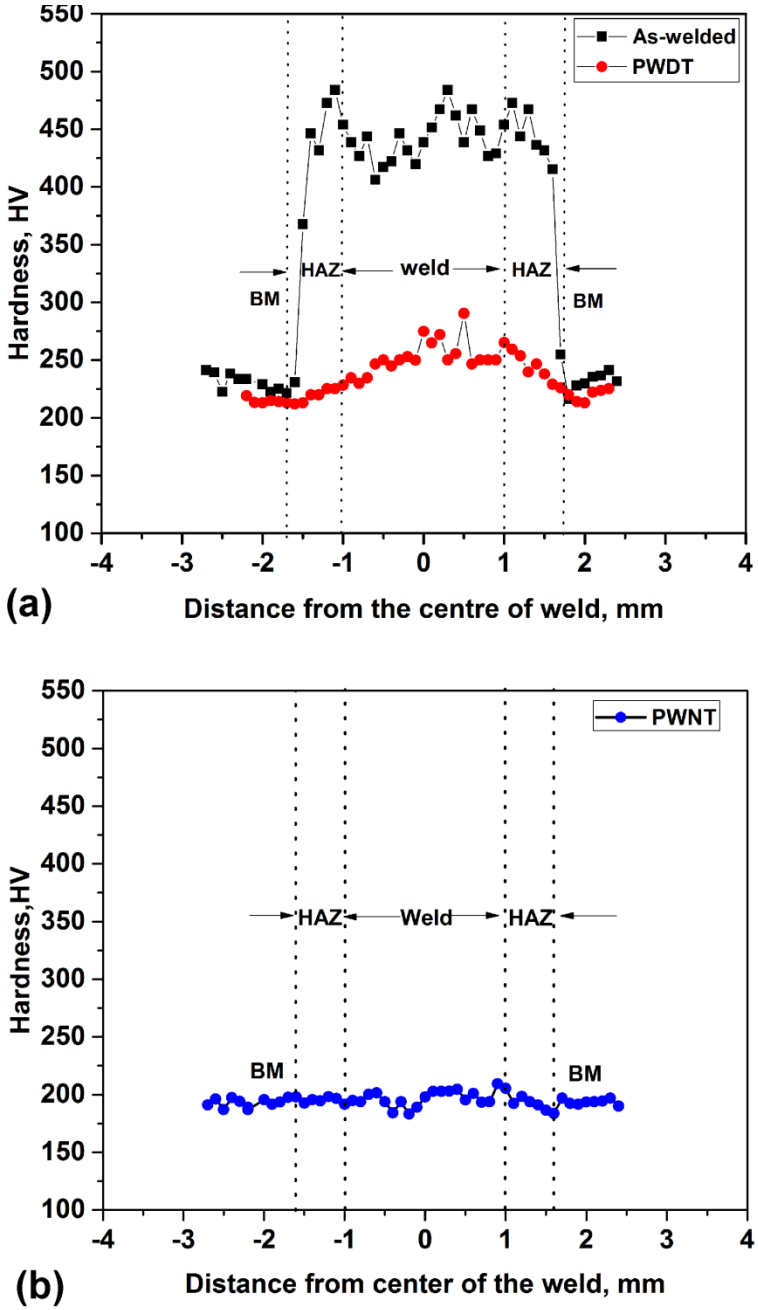

Figure 4.4.6 Microhardness profiles across the weld joint in (a) as-welded and PWDT conditions (b) PWNT condition.

post weld heat treated joints has been evaluated employing the full-size Charpy specimens. The Charpy V-notch in weld joints was located at weld centre line (Figure 4.4.7 (a)). The influence of materials condition on impact energy is shown in Figure 4.4.8. The as-welded joint exhibited very poor impact toughness compared to BM. PWNT treatment improved the impact toughness of the welded joint to a level higher than that of as-received parent metal. Investigations on fracture surface of impact tested samples indicated predominantly ductile fracture in case of BM, PWDT and PWNT conditions whereas quasi-cleavage mode of fracture dominated in as-welded state (Figure 4.4.9). Further, the impact tested samples were examined to locate the fracture path. It was revealed that the samples in which the crack path was confined to weld zone (Figure 4.4.7 (b)) possessed low impact toughness, whereas the samples in which the crack path was deviated from weld metal zone exhibited high values of impact toughness. The fractured sample in which the crack path was confined to the weld region is shown in Figure 4.4.7 (b) and the corresponding fractograph clearly reveals quasi-cleavage type fracture (Figure 4.4.7 (c)). The poor impact toughness of the as-welded joint may be attributed to the deleterious effects resulting from microstructural features such as coarse grain size, high carbon martensite, and to the presence of δ-ferrite in the weld zone. The δ-ferrite is preserved after PWDT and surrounded by coarse $M_{23}C_6$ carbides that weakened the cohesion between the δ-ferrite and prior austenite grain boundaries therefore restricted the recovery in impact toughness. Similar observation was made by Moon et.al in 9Cr2WVTa steel welds in which the impact toughness after tempering treatment is still lower than the base metal due to the existence of δ-ferrite [30]. Figure 4.4.10 shows fractographs of impact tested samples revealing ductile fracture for PWDT and PWNT conditions. The improved toughness after PWNT is found to have agreement with fine grain size, homogeneous

microstructure of tempered martensite and to the absence of δ-ferrite. Fine grain size helps to minimize stresses arising out of dislocation pile-ups and improves the resistance to impact toughness.

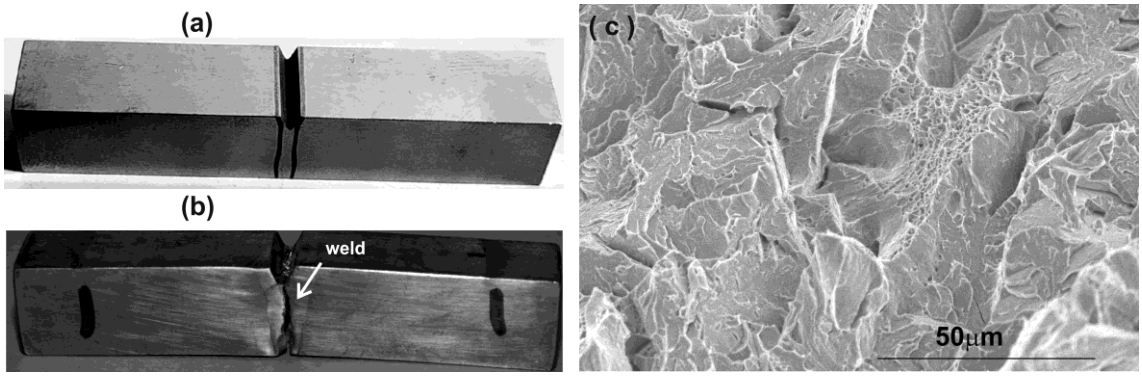

Figure 4.4.7 (a) Photograph of Charpy V-notch impact sample showing the location of notch (b) Impact tested fracture sample of as-welded joint showing the crack path and (c) fractograph of as-welded sample in figure (b) revealing quasi-cleavage fracture.

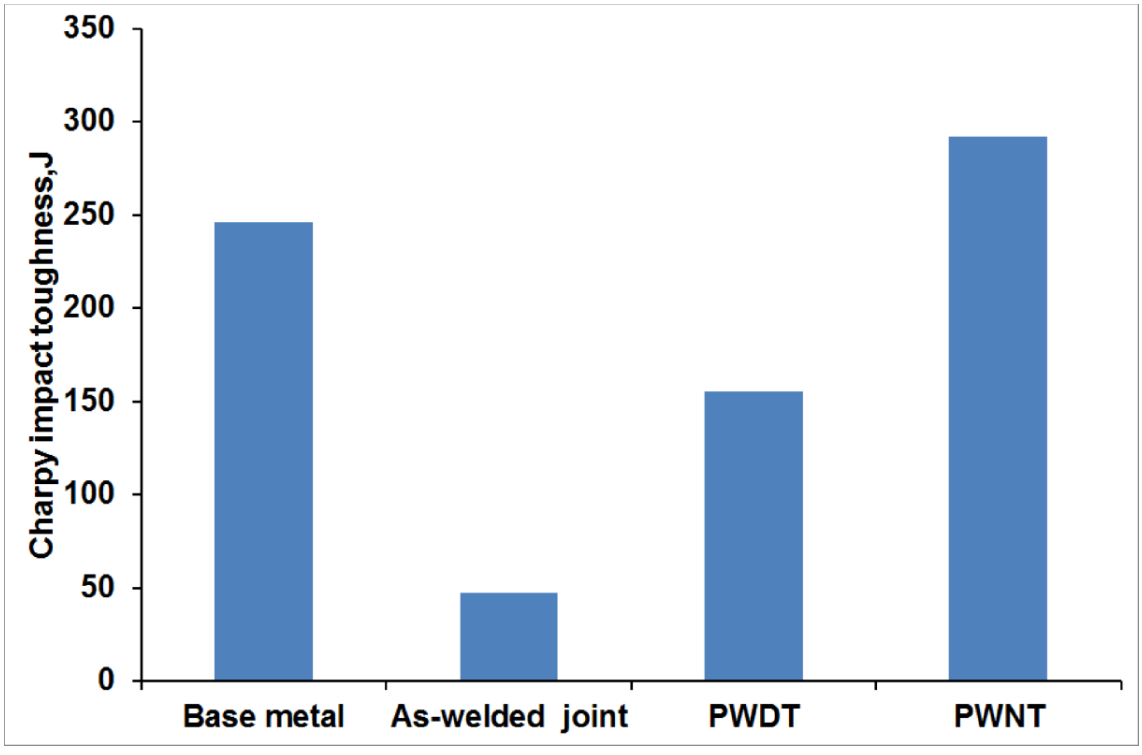

Figure 4.4.8 Charpy V-notch impact toughness of base metal and welded joints in various conditions at room temperature.

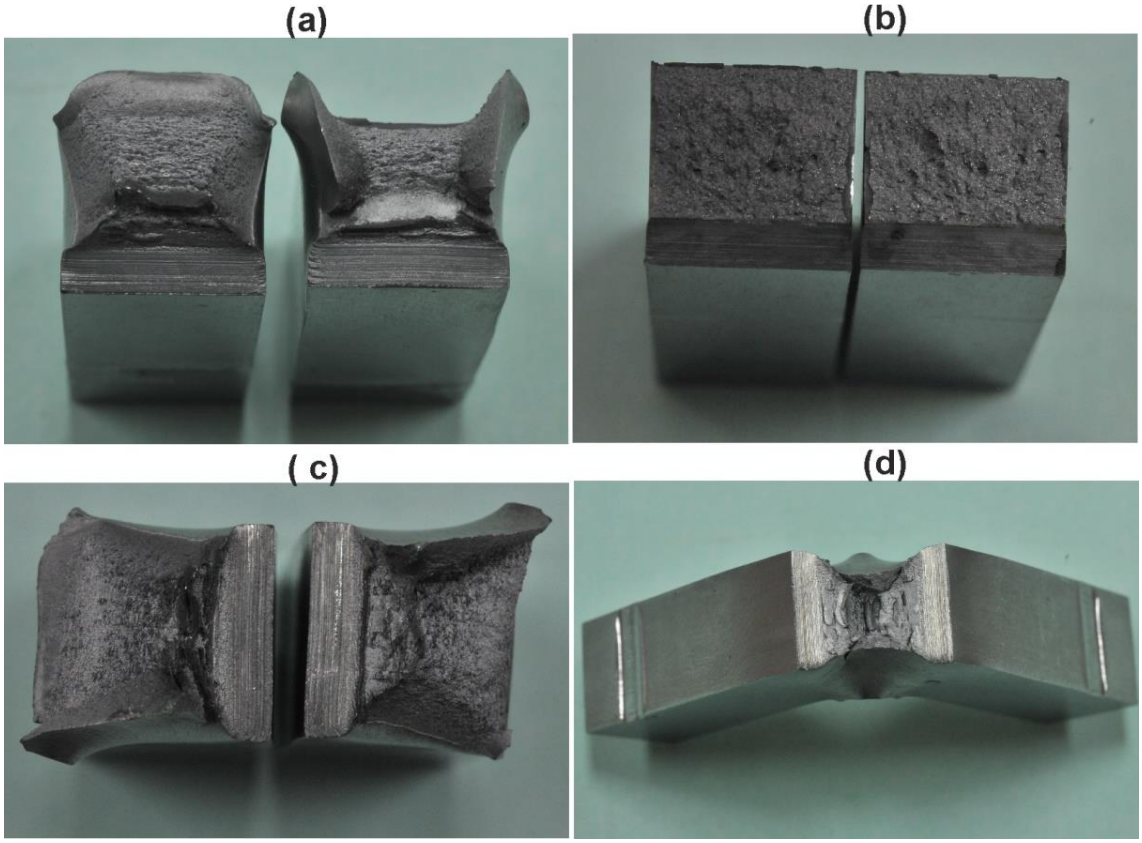

Figure 4.4.9 Appearance of Charpy V-notch impact fractured samples illustrating ductile fracture for base metal, PWDT and PWNT conditions (a, c and d) respectively. As welded condition (b) displays cleavage fracture

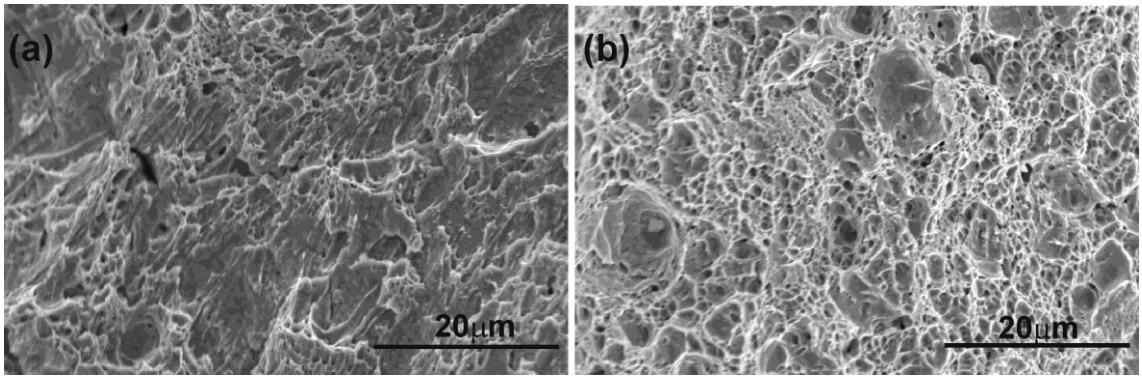

Figure 4.4.10 Fractographs of impact tested samples revealing ductile fracture for PWDT and PWNT conditions (a, b) respectively.

4.4.6. Tensile properties

The engineering tensile stress-strain curves obtained during room temperature tensile tests for various conditions are presented in Figure 4.4.11 and the tensile property data derived from these curves are given in Table 4.4.1.

The 0.2% offset Yield strength and UTS exhibited by various conditions are in the order: As-welded > BM > PWNT > PWDT. The joint after PWDT displayed much higher elongation whereas PWNT improved the elongation of weld-joint very marginally compared with as-welded condition. In all the conditions, tensile fracture took place in ductile mode and failure location was in the BM as shown in Figure 4.4.12. The higher strength of as-welded joint could be attributed to the pre-dominant influence of un-tempered martensite in the weld zone. The lower strength and substantial increase in elongation in PWDT state resulted from the combined effects of coarsening of prior existing carbides within HAZ and in the vicinity of HAZ in base metal, and tempering of martensite in the weld zone and HAZ.

Although there was a very narrow soft zone as revealed by low hardness in the intercritical region of HAZ, the tensile failure still prevailed in BM which was away from the HAZ region. This suggests that the intercritical region is very narrow to influence the overall tensile strength of the welded joint. These observations are inconformity with those reported by Das et al [28] in 9Cr-1W RAFM steel weldment prepared by EBW process. PWNT produced adequate elongation without significant reduction in strength compared to that of BM. During post-weld normalizing the δ-ferrite was eliminated and on subsequent tempering the microstructure in the weld metal displayed more homogeneous distribution of tempered martensite which is similar to that prevailing in the base metal.

Table 4.4.1 Room temperature tensile properties of base metal and electron beam welded joints in post weld heat treated conditions.

Material condition	Yield stress, MPa	UTS,MPa	% Elongation
Base metal	535	650	19
As welded joint	563	674	18
PWDT	474	629	31
PWNT	495	644	21

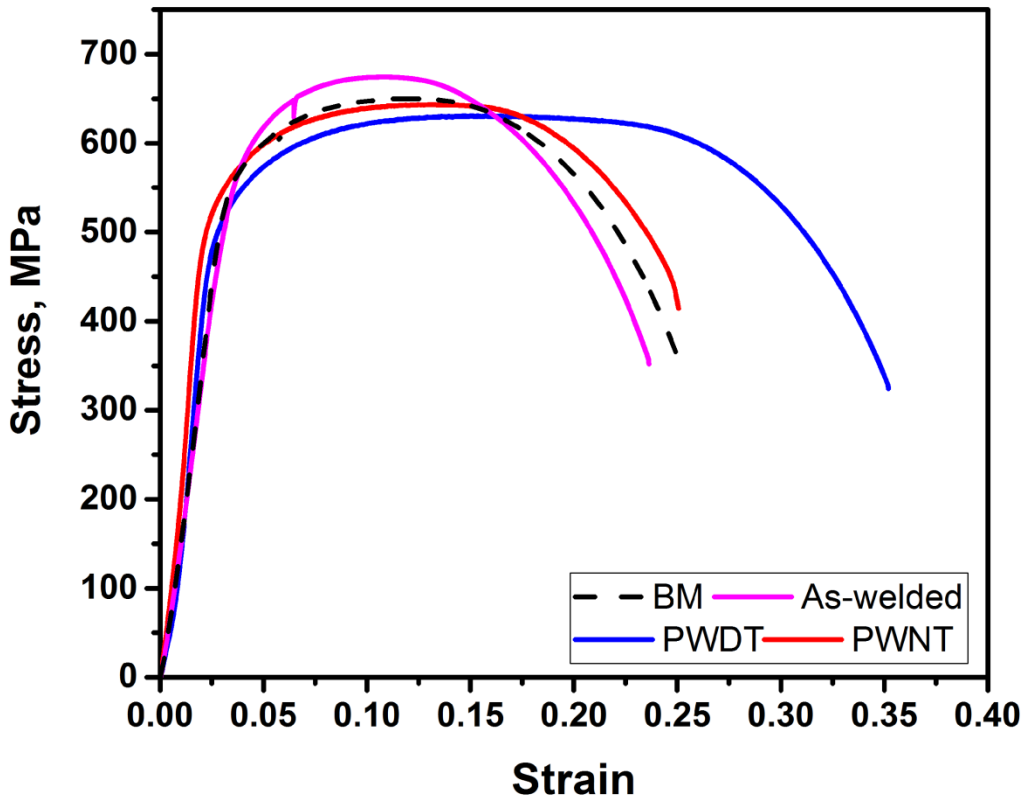

Figure 4.4.11 Stress-Strain plots of base metal, as-welded joint, post-weld direct tempered weld joint and post-weld normalised and tempered weld joints.

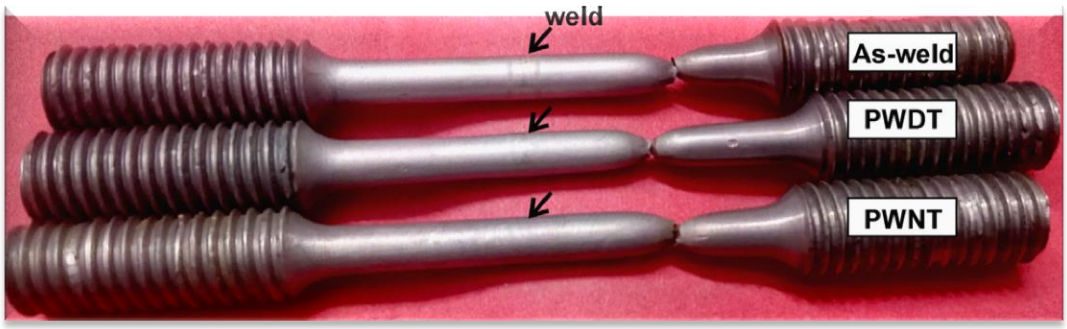

Figure 4.4.12 Tensile tested samples depicting the location of fracture in various conditions.

References

1. K.Laha, K.S.Chandravathi, P.Parameswaran, K.Bhanu Sankara Rao, Type IV cracking susceptibility in weld joints of different grades of Cr-Mo Ferritic Steel, Metallurgical and Materials Transactions A, 40 (2009) 386-397.

2. J.A.Francis, W.Mazur, H.D.K.Bhadeshia, Type IV cracking in ferritic power plant steels, Material Science and Technology, 22 (2006)1387-1395.

3. S.Sam, C.R.Das, V.Ramasubbu, S.K.Albert, A.K.Bhaduri, Delta-ferrite in the weld metal of reduced activation ferritic-martensitic steel, Journal of Nuclear Materials, 455 (2014) 343-348.

4. Y.Poitevin, L.V.Boccaccini, M.Zmitko, I.Ricapito, J.-F.Salavy, E.Diegele, F. Gabriel, E.Magnani, H.Neuberger, R.Lässer and L.Guerrini, Tritium breeder blankets design and technologies in Europe: Development status of ITER Test Blanket Modules, test & qualification strategy and roadmap towards DEMO, Fusion Engineering and Design, 85 (2010) 2340-2347.

5. S.Noh, H Tanigawa,H Fujii, A.Kimura, J.Shim, and T.K.Kim, Microstructural evolutions of friction stir welded F82H steel for fusion applications, Transactions Korean Nuclear Society Autumn Meeting Gyeongju, Korea, October 25-26: 2012

6. Y.D.Chung, H.Fujii, Y.Suna, H.Tanigawa, Interface microstructure evolution of dissimilar friction stir butt welded F82Hsteel and SUS304, Material Science and Engineering A, 528 (2011) 5812–5821.

7. Z.Yu, Z.Feng, D.Hoelzer, L.Tan, and M.A.Sokolov, Friction Stir Welding of ODS and RAFM steels, Metallurgical and Materials Transaction E, 2 (2015)164-172.

8. Y.S.Sato, H.Kokawa, Y.Yano, Y.Sekio, Mechanical properties of friction stir welded 11Cr-ferritic/martensitic steel, Journal of Nuclear Materials (2012), Article in press.

9. Ravikirana, Study of Transformation Characteristics and Microstructural Evolution in 9Cr Reduced Activation Ferritic/Martensitic Steel Using Electron Microscopy, Calorimetry and Computational Methods, Ph.D. Thesis, Homi Bhabha National Institute, August 2014.

10. N.A. McPherson, A.M. Galloway, S.R. Cater, S.J. Hambling, Friction stir welding of thin DH36 steel plate, Science and Technology of Welding and Joining, 18 (2013) 441-450

11. A. Toumpis, A. Galloway, S. Cater, N.A. McPherson, Development of a process envelope for friction stir welding of DH36 steel-A step change, Materials and Design, 62 (2014) 64-75

12. R.Mythili, Ravikirana, J.Vanaja, K Laha, S Saroja, T Jayakumar, M.D. Mathew, E.Rajendrakumar, Microstructural modification due to tungsten and tantalum in 9Cr reduced activation ferritic-martensitic steels on creep exposure, Procedia Engineering, 55 (2013) 295-299.

13. Ravikirana, R.Mythili, S.Raju, S.Saroja, T.Jayakumar, E.Rajendra Kumar, Decomposition modes of austenite in 9Cr–W–V–Ta reduced activation ferritic–martensitic steels, Material Science and Technology, 31 (2015) 448-459.

14. C.Liu, D.Zhang, Y.Liu, Q.Wang, Z.Yan, Investigation on the precipitation behaviour of M_3C phase in T91 ferritic steels, Nuclear Engineering and Design, 241 (2011) 2411–2415.

15. W.Tang, J.Chen, X.Yu, D.Frederick, and Z.Feng, Heat input and post weld heat treatment effects on reduced activation ferritic-martensitic steel friction stir welds, :R.S.Mishra, M.W.Mahoney, Y.Sato, Y.Hovanski (Eds), Friction stir welding and processing VIII, John Wiley & sons, Inc, New Jersey (2015)83-88.

16. J.Han, H.Li, Z.Zhu, F.Barbaro, L.Jiang, H.Xu, L.Ma, Microstructure and mechanical properties of friction stir welded 18Cr–2Mo ferritic stainless steel thick plate, Materials and Design, 63 (2014) 238–246.

17. V.L.Manugula, K.V.Rajulapati, G.M.Reddy, R.Mythili and K.Bhanu Sankara Rao: A Critical Assessment of the Microstructure and Mechanical Properties of Friction Stir Welded Reduced Activation Ferritic-Martensitic Steel, Materials and Design, 92 (2016) 200-212.

18. K.Laha, S.Saroja, A.Moitra, R.Sandhya, M.D.Mathew, T.Jayakumar and E.Rajendrakumar, Development of Indian specific RAFM steel through optimisation of tungsten and tantalum contents for better combination of impact, tensile, low cycle fatigue and creep properties, Journal of Nuclear Materials, 439 (2013) 41-50.

19. S.Raju, B.Jeyaganesh, A.K.Rai, R.Mythili, S.Saroja, E.Mohandas, M. Vijayalakshmi, K.Bhanu Sankara Rao, and B.Raj, Journal of Nuclear Materials, 389 (2009) 385-393

20. S.Saroja, A.Dasgupta, R.Divakar, S.Raju, E.Mohandas, M.VijayaLakshmi and K.Bhanu Sankara Rao, Development and characterization of advanced 9Cr ferritic/martensitic steels for fission and fusion reactors, Journal of Nuclear Materials,409 (2011) 131-139.

21. R. Ravikirana, R Mythili, S Raju, S Saroja, G. Paneerselvam, T Jayakumar and E. Rajendra kumar, Effect of alloy content on microstructure and microchemistry of phases during short term thermal exposure of 9Cr–W–Ta–0·1C reduced activation ferritic/martensitic (RAFM) steels, Bulliten of Material Science, 37 (2014) 1453–1460.

22. B. Raj, K. Bhanu Sankara Rao, A.K. Bhaduri, Progress in the development of reduced activation ferritic-martensitic steels and fabrication technologies in India, Fusion Engineering and Design, 85 (2010) 1460-1468.

23. Z.Lu, R.G. Faulkner, N.Riddle, F.D. Martino and K. Yang, Effect of heat treatment on microstructure and hardness of Eurofer 97,Eurofer ODS and T92 steels, Journal of Nuclear Materials, 386-388 (2009) 445-448.

24. S.Zheng, Q.Wu, Q.Huang, S.Liu, Y.Han, Influence of different cooling rates on the microstructure of the HAZ and welding CCT diagram of CLAM steel, Fusion Engineering and Design, 86 (2011) 2616-2619.

25. S.Chen, J.Huang, Q.Lu, X.Zhao, Microstructures and mechanical properties of laser welding joint of a CLAM steel with revised chemical compositions, Journal of Materials Engineering and Performance, 25 (2016) 1848-1855.

26. K.Anderko, L.Schafer, E.Materna-Morris, Effect of delta-ferrite on the impact properties of martensitic chromium steels, Journal of Nuclear Materials, 179-18 1(1991) 492-495.

27. L.Schafer , Influence of delta-ferrite and dendritic carbides on the impact and tensile properties of martensitic chromium steels, Journal of Nuclear Materials, 258-263 (1998) 1336-1339.

28. C.R.Das, S.K.Albert, S.Sam, P.Mastaniah, G.M.S.K.Chaitanya, A.K.Bhaduri, T.Jaya kumar, C.V.S.Murthy, E.Rajendrakumar, Mechanical properties of 9Cr-1W reduced activation ferritic martensitic steel weldment prepared by electron beam welding process, Fusion Engineering and Design, 89 (2014) 2672-2678.

29. G.Krauss, Martensite in steel: strength and structure, Material Science and Engineering A, 273–275 (1999) 40–57

30. J.Moon, C-H.Lee, T-H.Lee, and H.Chan Kim, Effect of heat input on microstructure evolution and mechanical properties in the weld heat-affected zone of 9Cr-2W-VTa reduced activation ferritic-martensitic steel for fusion reactor, Metallurgical and Materials Transactions A, 46 (2005) 156-163.

Chapter 5- Conclusions and future scope

5.1. Summary of the work

This thesis entitled **"Advanced Methods of Joining Indian Reduced Activation Ferritic-Martensitic Steel"** is aimed at establishing suitable welding parameters for the production of very clean RAFM steel weld joints by employing FSW and EBW processes and understanding the role of evolving microstructure on mechanical properties. Special attention has been paid to develop suitable post weld heat treatments and understanding their role in promoting the suitable microstructure for deriving the optimum mechanical properties in INRAFM (India specific) steel weld joints. The research work has been conducted with the focus on:

- Assessment of the effects of rotational speed on the evolving microstructure in various zones of FSW weld joints with special reference to the phase transition temperatures and ascertaining the influence of evolving microstructure on hardness and impact toughness of the weld joints
- Establishing suitable post weld heat treatments that could give rise to acceptable hardness and impact toughness in FSW weld joints
- Exploring the section thickness effects on microstructure and mechanical properties of FSW joints
- Studies on the evaluation of microstructure and its influence on mechanical properties of EBW joints and identifying suitable post weld heat treatments for EBW joints

The results pertaining to the "**Effects of tool rotational speed on microstructure and mechanical properties during FSW of INRAFM steel"** are summarised as follows:

The feasibility of producing full-penetration FSW joints on 6-mm-thick RAFM steel plates was demonstrated employing PcBN tools. The optimum rotational speed required without phase transformation during FSW has been established. The interface temperature between the bottom surface of the shoulder and the top surface of the work-piece was successfully monitored employing non-contact in-line thermography for the first time. This serves as an indicator for peak temperature attained during FSW. The interface temperatures for 200, 300 and 500, and 700 rpm were respectively below A_{c1}, between A_{c1} and A_{c3}, and above A_{c3}. The FSW joints were made up of BM, SZ, TMAZ and HAZ. The as-welded microstructure in these zones was dependent on rotational speed. In the as-welded state very high hardness was recorded in SZ irrespective of rotational speed. Grain boundary carbides dissolved and Fe_3C precipitated in the SZs at all rotational speeds. The microstructural changes in TMAZ in as-welded state indicated the occurrence of dynamic recovery and dynamic recrystallization and were driven by the combined influence of heat generated and deformation induced by the tool. Impact toughness is close to BM in the as-welded state for low rotational speed welds whereas high rotational speeds caused very low impact toughness. A good correlation between the measured interface temperatures and evolving microstructure in SZs could be established. PWHT was found necessary to restore grain boundary carbides and bring down the hardness in stir zone to the level of base metal.

The second theme of the study deals with "**Influence of tool rotational speed and post weld heat treatments on friction stir welding of RAFM steel".** Salient results of the study are as follows:

Subsequent to FSW, irrespective of rotational speed, re-austenitization and tempering treatment is necessary for obtaining the homogeneous distribution of strengthening precipitates in optimum size and distribution. The presence of Fe-rich

M_3C was not observed after PWHTs, suggesting the metastable nature of these precipitates. PWHTs reduced the stir zone hardness to an acceptable value. After PWDT the precipitate ripening was more intense in HAZ of 700 rpm. The PWDT significantly improved the impact toughness of 700 rpm weld joints and indeed the toughness values are very close to BM. The PWNT displayed homogeneous distribution of precipitates and hardness across the weld joint and hence the impact toughness was found to be higher than that achieved through PWDT.It is recommended to employ low rotational speeds in FSW where the interface temperatures are below A_{c1} and just above recrystallization temperature, followed by PWNT for obtaining optimum mechanical properties in FSW joints.

The third theme deals with **"Role of section thickness in FSW on microstructure and mechanical properties"** and the important results are summarised as follows:

The feasibility of producing full-penetration FSW joints on 12-mm-thick RAFM steel plates was demonstrated employing PcBN tools. Section-thickness strongly influenced the width of various zones and microstructures developed due to thermal gradients and associated slow cooling rates across the weld joint resulting from high heat input. The slow cooling rate led to the formation of α-ferrite and martensite in the TMAZ close to BM. PWHTs were found beneficial in decreasing the hardness of SZ and enabling the desirable precipitation of grain boundary carbides. The excessive softening of HAZ was prominent after PWDT. Post weld normalized and tempered treatment was found beneficial for eliminating the softening in HAZ. The PWDT significantly improved the impact toughness of weld joints and indeed the toughness values are very close to BM. This study suggests that tool geometry has to be properly designed for different thicknesses and FSW parameters for each thickness are to be separately established.

Fourth theme comprising the results of EBW of INRAFM steel and presents the systematic study on "**Role of evolving microstructure on the mechanical properties in the as-welded and post weld heat-treated states".** The salient results are presented as follows:

The electron beam weld zone microstructure consisted of martensite in coarse grains and small amount of δ-ferrite. The width of HAZ was much smaller owing to the low heat input of EBW process.The weld zone in as-welded condition exhibited high hardness compared to base metal. The impact toughness of as-welded joint was much poorer due to the occurrence of martensite and δ-ferrite in weld zone. Though the impact toughness was improved after PWDT, the value obtained was still much lower than that recorded for base metal. PWNT eliminated the δ-ferrite in the weld zone, refined the grain structure due to recovery and recrystallization processes and hence resulted in higher impact toughness than the base metal. The hardness profile was relatively uniform across the weld joint after PWNT and very much similar to that recorded in parent metal. The tensile properties of PWNT weld joints were comparable to that of the base metal. The PWNT is an effective way of improving the mechanical properties of EB weld joint.

5.2. Scope for future work

- Detailed investigations are to be conducted to optimise the tool traverse speed, in order to maximise the speed and to produce full penetration welds without any defects.
- Detailed FSW experiments on higher thickness (>12 mm) plates have to be conducted to optimise the tool rotational speed so that FSW could be achieved below A_{c1} transformation temperature and above recrystallization temperature of BM. Evaluation of tensile properties and DBTT on full-size Charpy samples in the PWNT condition is to be generated. This could not be done in the current investigation due to non-availability of sufficient samples, delayed by the tool procurement.
- TEM investigations have to be conducted in order to study the evolution of substructure in TMAZ and HAZ. This would be possible only in thick section welds, since there is likely possibility of thick sections (>12 mm) generating wider TMAZ and HAZ, that would enable to take samples from the individual zones.
- Gleeble simulations have to be conducted on thick plates to obtain prior information on microstructural changes occurring during thermal cycle. Correlations shall be established on thermal simulation conducted on base metal and actual joints produced through FSW.
- Evaluation of creep properties of FSW weld joints and EBW joints at operating temperatures of RAFM steel has to be performed.